



THERMOELECTRIC MULTILAYER GENERATOR OF NANO OXIDE  
THERMOELECTRIC MATERIALS

DISSERTATION

BY

WANATCHAPORN NAMHONGSA

A Dissertation Submitted in Partial Fulfillment of the Requirements for  
The Doctor of Philosophy Program in Physics  
at Sakon Nakhon Rajabhat University

September 2021

All Rights Reserved by Sakon Nakhon Rajabhat University

THERMOELECTRIC MULTILAYER GENERATOR OF NANO OXIDE  
THERMOELECTRIC MATERIALS

DISSERTATION  
BY  
WANATCHAPORN NAMHONGSA

A Dissertation Submitted in Partial Fulfillment of the Requirements for  
The Doctor of Philosophy Program in Physics  
at Sakon Nakhon Rajabhat University  
September 2021  
All Rights Reserved by Sakon Nakhon Rajabhat University



DISSERTATION APPROVAL  
SAKON NAKHON RAJABHAT UNIVERSITY  
DOCTOR OF PHILOSOPHY  
PROGRAM IN PHYSICS

Dissertation Title: Thermoelectric Multilayer Generator of Nano Oxide Thermoelectric Materials  
Author: Wanatchaporn Namhongsa

Dissertation Examination Committee

Anucha Watcharapason Chairperson T. Seetawan Committee  
(Assoc. Prof. Dr. Anucha Watcharapason) (Prof. Dr. Tosawat Seetawan) and Advisor

Wilawan Kumharn Committee  
(Assoc. Prof. Dr. Wilawan Kumharn)

Athorn Committee H. Wattanasarn Committee  
(Assist. Prof. Dr. Athorn Vora-ud) (Assist. Prof. Dr. Hassakorn Wattanasarn)

Approval by the Curriculum Committee

Athorn  
(Assist. Prof. Dr. Athorn Vora-ud)  
Chair of the Committee for Curriculum  
Administration Approval  
Sakon Nakhon Rajabhat University

Approval by Graduate School

S. Pienthunyakorn  
(Assoc. Prof. Dr. Sikan Pienthunyakorn)  
The Director of Graduate School  
Sakon Nakhon Rajabhat University

28 September 2021

Copyright of Sakon Nakhon Rajabhat University

## ACKNOWLEDGEMENTS

These last three years of being a PhD student in my group have been challenging, enriching, and have broadened my world perspective. Firstly, I would like to acknowledge the financial supported by “National Research Council of Thailand (NRCT) through the Royal Golden Jubilee (RGJ) Ph.D. Program (Grant No. PHD/0065/2560)”. My supervisors Prof. Dr. Tosawat Seetawan and co-advisor have made the completion of this dissertation possible. Whose gave best advice and be guidance of this thesis since start until successful. He gave appreciate suggestion, checked, and corrected the fault of this thesis. I have learned a lot from his strong background on material science and expertise on thermoelectric. I have been inspired by his tremendous love for work. His commitment to the highest scientific standards gave me more challenges and was a motivation for me to always try harder.

I would like to thank the thesis committee such as Assoc. Prof. Dr. Anucha Watcharapasorn, Assoc. Prof. Dr. Wilawan Kumharn, Assist. Prof. Dr. Athorn Vora-ud, and Assist. Prof. Dr. Hassakorn Wattanasarn for their kindly advise and helpful suggestions, including staff member, Ph.D. students of Center of Excellence on Alternative Energy (CEAE), Research and Development Institution and Program of Physics, Faculty of Science and Technology, Sakon Nakhon Rajabhat University. The thesis also could not be able to be completed without the help from my good friends.

Above all, I am deeply appreciative of the eternal love and care from my parents. They are the reason for me to be able to overcome all the hard times I have been through and to keep on going. Always I remember the feeling when all my tiredness and hopelessness disappeared only by hearing voices from mom, dad, brother. Each of you are everything I have.

Wanatchaporn Namhongsa



<b>TITLE</b>	Thermoelectric Multilayer Generator of Nano Oxide Thermoelectric Materials
<b>AUTHOR</b>	Wanatchaporn Namhongsa
<b>ADVISOR</b>	Prof. Dr. Tosawat Seetawan
<b>DEGREE</b>	Ph.D. (Physics)
<b>INSTITUTION</b>	Sakon Nakhon Rajabhat University
<b>YEAR</b>	2021

### ABSTRACT

The thermoelectric oxides n-type calcium manganese oxide ( $\text{CaMnO}_3$ ) and p-type calcium cobalt oxide ( $\text{Ca}_3\text{Co}_4\text{O}_9$ ) were synthesized from nano precursor powder using a solid-state reaction method. It consists of a grinding powder to reduce particle size by mill agate jar, incineration to remove impurities, and a hot-pressing method to compress the crystals. The crystal structure and morphology were studied by XRD and FE-SEM. The thermoelectric properties from an ambient temperature to 973 K of the n- $\text{CaMnO}_3$  and p- $\text{Ca}_3\text{Co}_4\text{O}_9$  samples that were measured consists of the Seebeck coefficient, electrical resistivity, power factor, and thermal conductivity.

The results showed that after milling, the n-type  $\text{CaMnO}_3$  material has a reduced particle size. The crystalline nano sizes could be sustained in a short time by hot pressing. The material was identified as an orthorhombic single-crystal structure. The Seebeck coefficient has shown a negative in this case. The values of electrical resistivity and relative density have lower than those of micro-synthesized references. It has a reduced Seebeck coefficient and a higher resistivity. As a result, the  $ZT$  value of n- $\text{CaMnO}_3$  has highest about 0.008.

The crystal structure of  $\text{Ca}_3\text{Co}_4\text{O}_9$  is consisting of alternate stacking sub-systems with a two-dimensional triangular lattice of rock-salt-structure [ $\text{Ca}_2\text{CoO}_3$ ] layers sandwiched between two hexagonal [ $\text{CoO}_2$ ] layers along c-axis. It has a

relative density of 94.87 %. It is hot-pressed for a short time to keep the nano-scale crystallinity, which results in increasing Seebeck coefficient. As well as electrical resistivity and thermal conductivity were decreased with increasing temperature (0.73 mW/K) leading to an increase of  $ZT$  (0.25). As a result, it is suitable for fabrication into p-type of thermoelectric materials.

Fabrication the horizontal of one-pair and two-pair thermoelectric generator using n-type  $\text{CaMnO}_3$  and p-type  $\text{Ca}_3\text{Co}_4\text{O}_9$  thermoelectric oxide materials coupled connected with silver electrodes. At the differential difference 473 K was measured the electric potential difference, output power ( $P_{\max}$ ), and current. To investigate the possibility of generating electricity for 3 horizontal shape thermoelectric devices, it was observed that resistances around 1 pair (0.33 k $\Omega$ ), 2 pairs with series circuit (27.5 k $\Omega$ ), and 2 pairs with parallel circuit (2.14 k $\Omega$ ), respectively. The electric potential difference was increased with increasing the temperature difference. The maximum potential difference of 1 pair is 82.14 mV, with current value of 0.14 mA and  $P_{\max}$  of 7.30  $\mu\text{W}$ . Therefore, 2 pairs connected with series circuit has maximum potential difference about 82.27 mV, with current value of 0.15 mA and  $P_{\max}$  of 6.12  $\mu\text{W}$ . Finally, the electric potential difference of 2 pairs connected with parallel circuit is 100.59 mV, current 0.16 mA, and  $P_{\max}$  7.46  $\mu\text{W}$  respectively indicating that this research a higher efficiency of horizontal thermoelectric generators constructed of oxide materials.

**Keywords:** Nano materials, Calcium cobalt oxide, Calcium manganese oxide, Thermoelectric properties, Thermoelectric generator

ชื่อเรื่อง	เครื่องกำเนิดไฟฟ้าเทอร์โมอิเล็กทริกแบบหลายชั้นของวัสดุนาโนออกไซด์เทอร์โมอิเล็กทริก
ผู้วิจัย	วนัชพร นามหงษา
กรรมการที่ปรึกษา	ศาสตราจารย์ ดร. ทศวรรษ ลีตะวัน
ปริญญา	ปร.ด. (ฟิสิกส์)
สถาบัน	มหาวิทยาลัยราชภัฏสกลนคร
ปีที่พิมพ์	2564

### บทคัดย่อ

การสังเคราะห์วัสดุออกไซด์เทอร์โมอิเล็กทริกชนิดเอ็น แคลเซียมแมงกานีสออกไซด์ ( $\text{CaMnO}_3$ ) และชนิดพี แคลเซียมโคบอลต์ออกไซด์ ( $\text{Ca}_3\text{Co}_4\text{O}_9$ ) จากสารตั้งต้นระดับนาโนด้วยวิธีปฏิกิริยาสถานะของแข็ง มีการบดเพื่อลดขนาดอนุภาคด้วยโอบดลูกอาร์เกต การเผาไล่สิ่งเจือปน และการอัดเผาผลึกด้วยวิธีการอัดร้อน ศึกษาโครงสร้างผลึกและลักษณะทางกายภาพโดยใช้ XRD และ FE-SEM วัดสมบัติทางเทอร์โมอิเล็กทริกของ  $n\text{-CaMnO}_3$  และ  $p\text{-Ca}_3\text{Co}_4\text{O}_9$  จากอุณหภูมิห้องถึง 973 K เช่นวัดค่าสัมประสิทธิ์ซีเบก ค่าสภาพต้านทานไฟฟ้า ค่าตัวประกอบกำลังไฟฟ้า และค่าสภาพนำความร้อน

ผลการวิจัยพบว่า วัสดุนาโนออกไซด์เทอร์โมอิเล็กทริกชนิดเอ็น  $\text{CaMnO}_3$  มีขนาดอนุภาคเล็กลงเมื่อผ่านการบด การอัดร้อนใช้ระยะเวลาสั้นเพื่อกดความเป็นผลึกในระดับนาโน พบว่าวัสดุนี้อาจมีโครงสร้างผลึกเดี่ยวแบบออร์โธโรมบิก ซึ่งค่าสัมประสิทธิ์ซีเบกมีค่าเป็นลบ มีค่าสภาพต้านทานไฟฟ้าและความหนาแน่นสัมพัทธ์ต่ำกว่าสารอ้างอิงที่มีการสังเคราะห์ในระดับไมโคร ทำให้สัมประสิทธิ์ซีเบกมีค่าลดลงและค่าสภาพต้านทานไฟฟ้าสูงขึ้น เนื่องจากความสัมพัทธ์ที่กล่าวมาทำให้ค่า  $ZT$  ของ  $n\text{-CaMnO}_3$  อยู่ที่ 0.008

ในส่วนของ วัสดุนาโนออกไซด์เทอร์โมอิเล็กทริกชนิดพี  $\text{Ca}_3\text{Co}_4\text{O}_9$  พบว่ามีการเรียงซ้อนตัวกันของชั้นโครงสร้างแบบโซเดียมคลอไรด์ (rock-salt structure) ประกอบระหว่างชั้นโครงสร้างเฮกซะกอลนอลสองชั้นตามแกน  $c$  มีความหนาแน่นสัมพัทธ์มากกว่า 94.87% การอัดร้อนใช้ระยะเวลาสั้นเพื่อกดความเป็นผลึกในระดับนาโนทำให้ค่าสัมประสิทธิ์ซีเบกสูงขึ้น และมีค่าสภาพต้านทานไฟฟ้าและสภาพนำความร้อนลดลงซึ่งมีค่า

0.73 W/mK ที่อุณหภูมิ 973 K ทำให้ค่า  $ZT$  เพิ่มขึ้นตามอุณหภูมิที่เพิ่มขึ้น ซึ่งมีค่า 0.25 จึงเหมาะที่จะนำไปประดิษฐ์เป็นวัสดุเทอร์โมอิเล็กทริกชนิดพี

การประดิษฐ์เครื่องกำเนิดไฟฟ้าเทอร์โมอิเล็กทริกแบบแวนนอน 1 คู่ และ 2 คู่ ด้วยวัสดุออกไซด์เทอร์โมอิเล็กทริกชนิดเอ็น  $\text{CaMnO}_3$  และชนิดพี  $\text{Ca}_3\text{Co}_4\text{O}_9$  เชื่อมต่อกับขั้วไฟฟ้าเงิน ที่ผลต่างอุณหภูมิ 473 เคลวิน วัดความต่างศักย์ไฟฟ้า (electric potential difference,  $V$ ) กำลังไฟฟ้าด้านออก (output power,  $P_{\text{max}}$ ) และกระแสไฟฟ้า (current,  $I$ ) เพื่อวิเคราะห์ความเป็นไปได้ในการผลิตไฟฟ้า พบว่า 1 คู่ 2 คู่ (แบบอนุกรม และขนาน) มีค่าความต้านทาน 0.33 k $\Omega$ , 27.5 k $\Omega$ , และ 2.14 k $\Omega$  ตามลำดับ มีค่าความต่างศักย์ไฟฟ้าเพิ่มขึ้นตามผลต่างอุณหภูมิที่เพิ่มขึ้น โดยมีค่าความต่างศักย์ไฟฟ้าสูงสุดของ 1 คู่ มีค่าความต่างศักย์ไฟฟ้าวงจรเปิด 82.14 mV มีค่ากระแสไฟฟ้า 0.14 mA มีค่ากำลังไฟฟ้าด้านออกสูงสุดที่ 7.30  $\mu\text{W}$  ในขณะที่ ต่อ 2 คู่ (แบบ อนุกรม) มีค่าความต่างศักย์ไฟฟ้าวงจรเปิด 82.27 mV กระแสไฟฟ้า 0.15 mA ค่ากำลังไฟฟ้าด้านออกสูงสุดที่ 6.12  $\mu\text{W}$  และ 2 คู่ (แบบขนาน) มีค่าความต่างศักย์ไฟฟ้าวงจร 100.59 mV กระแสไฟฟ้า 0.16 mA โดยมีค่ากำลังไฟฟ้าด้านออกสูงสุดที่ 7.46  $\mu\text{W}$  ซึ่งแสดงให้เห็นว่าการวิจัยครั้งนี้แสดงการเพิ่มประสิทธิภาพให้เครื่องกำเนิดไฟฟ้าเทอร์โมอิเล็กทริกจากวัสดุออกไซด์ให้มีประสิทธิภาพที่สูงขึ้น

**คำสำคัญ** วัสดุนาโน แคลเซียมโคบอลต์ออกไซด์ แคลเซียมแมงกานีสออกไซด์ สมบัติเทอร์โมอิเล็กทริก เครื่องกำเนิดไฟฟ้าเทอร์โมอิเล็กทริก

## TABLE OF CONTENTS

CHAPTER	PAGE
1 INTRODUCTION .....	1
Motivation .....	1
Research Objectives .....	5
Scope and Limitation of Thesis .....	6
Anticipated Outcomes of thesis .....	6
Financial Support .....	6
References .....	7
2 THEORY AND LITERATURE REVIEW .....	9
Thermoelectric Effects .....	9
Seebeck Effect .....	9
Peltier Effect .....	11
Thomson Effect .....	13
Functions of Thermoelectric Effects .....	15
Optimizing the figure of merit, ZT and Thermoelectric parameters .....	18
Thermoelectric Parameters .....	19
Seebeck coefficient .....	20
Electrical Resistivity .....	21
Thermal Conductivity .....	22
The electrical thermal conductivity .....	23
The lattice thermal conductivity .....	24
Enhancement of ZT with nanomaterials .....	24
Dimensions of nanomaterials .....	25
Phonon Scattering .....	27
The key differences between nanomaterials and bulk materials .....	27

## TABLE OF CONTENTS (Continued)

CHAPTER	PAGE
Compatibility and efficiency ratio of oxide thermoelectric materials .....	28
Current Research of Thermoelectric, Thermoelectric Oxide and Thermoelectric Oxide Nano Materials.....	29
P-type Oxides; Calcium cobaltite .....	30
N-Type; Manganese Oxide .....	36
Thermoelectric generators .....	37
Energy conversion efficiency .....	38
Multilayer or segmented bulk thermoelectric generators .....	40
Overview of oxide segmented TEGs and their relevant fabrication Techniques.....	41
References .....	47
<b>3 METHODOLOGY .....</b>	<b>55</b>
Synthesis And Preparation Thermoelectric Materials .....	56
Synthesis n-CaMnO <sub>3</sub> and p-Ca <sub>3</sub> Co <sub>4</sub> O <sub>9</sub> powder thermoelectric materials	56
Preparation n-CaMnO <sub>3</sub> thermoelectric material .....	59
Preparation of p-Ca <sub>3</sub> Co <sub>4</sub> O <sub>9</sub> bulk thermoelectric materials .....	62
Characterization Techniques .....	66
Sample Identification: X-ray Diffraction Analysis .....	66
Crystallite size .....	67
Microstructure Characterization: Field Emission Scanning Electron Microscopy.....	69
Extensibility: Energy Dispersive X-ray Spectrometer (EDS) .....	72
Thermoelectric Properties Measurements .....	72
Seebeck Coefficient / Electric Resistance Measurement System ZEM-3 series.....	72

## TABLE OF CONTENTS (Continued)

CHAPTER	PAGE
Thermal Conductivity of n-CaMnO <sub>3</sub> and p-Ca <sub>3</sub> Co <sub>4</sub> O <sub>9</sub> .....	75
Density Determination of Solids .....	76
Dimensionless Figure of Merit .....	77
Conversion Efficiency of Thermoelectric Cell and Module .....	77
Thermoelectric module fabrication and measurement .....	77
Thermoelectric module design .....	78
Segmented modules fabrication .....	79
Joining methods .....	80
Diffusion bonding .....	80
Brazing / soldering .....	81
Advantages of Brazing and Soldering .....	81
How to Select an appropriate joining method .....	83
Contact resistance of segmented thermoelectric modules .....	84
Segmented thermoelectric generator tester .....	84
References .....	87
 4 RESULTS AND DISCUSSION .....	 89
Thermoelectric Materials Synthesis .....	89
n-CaMnO <sub>3</sub> : Crystal Structure and Chemical Composition .....	89
Microstructure Analysis .....	93
n-CaMnO <sub>3</sub> : Thermoelectric properties .....	95
p-Ca <sub>3</sub> Co <sub>4</sub> O <sub>9</sub> : Crystal Structure and Chemical Composition .....	101
Synthesis Ca <sub>3</sub> Co <sub>4</sub> O <sub>9</sub> thermoelectric materials .....	101
Microstructure Analysis .....	106
p-Ca <sub>3</sub> Co <sub>4</sub> O <sub>9</sub> : Thermoelectric properties .....	110

## TABLE OF CONTENTS (Continued)

CHAPTER	PAGE
Thermoelectric multilayers generator fabrication of n-CaMnO <sub>3</sub> and p-Ca <sub>3</sub> Co <sub>4</sub> O <sub>9</sub> .....	117
Microstructure Analysis .....	119
Thermoelectric properties of multilayer thermoelectric modules .....	121
Power Generation Characteristics of The Modules .....	121
References .....	127
 5 CONCLUSIONS AND SUGGESTION .....	 131
Conclusions .....	131
Thermoelectric materials .....	131
Thermoelectric devices .....	133
Suggestion .....	134
Appendix.....	137
Appendix A Publications.....	139
Paper I .....	142
Paper II .....	151
Appendix B International Conferences	157
Appendix C The activities	161
Appendix D A brief history of research	165



## LIST OF TABLES

Table	Page
3.1 List of chemicals used for solid-state reaction methods, their formula, supplier, and purity.....	56
3.2 List of equipment used for synthesis of powder, preparation of bulk, characterization, and measurement of thermoelectric properties together with their model and area of application .....	57
3.3 Materials balance of n-CaMnO <sub>3</sub> for 10 g .....	59
3.4 Materials balance of and p-Ca <sub>3</sub> Co <sub>4</sub> O <sub>9</sub> for 10 g .....	62
3.5 ZEM-3 conditions of n-CaMnO <sub>3</sub> and p-Ca <sub>3</sub> Co <sub>4</sub> O <sub>9</sub> sample .....	75
4.1 Crystallographic parameters with average crystallite size, density, and relative density of CaMnO <sub>3</sub> nanoparticles .....	92
4.2 The EDS of CaMnO <sub>3</sub> bulk sample .....	94
4.3 The average crystallite size (D) determined by XRD of nano precursors powder, ball-milled, calcined samples, and grain size (d) from SEM for sintered Ca <sub>3</sub> Co <sub>4</sub> O <sub>9</sub> sample.....	105
4.4 The density, theoretical density, and the lattice parameter (a, b, and c) of Ca <sub>3</sub> Co <sub>4</sub> O <sub>9</sub> samples .....	109

## LIST OF FIGURES

Figure	Page
1.1 zT of $\text{Ca}_3\text{Co}_4\text{O}_9$ and $\text{CaMnO}_3$ oxide thermoelectric materials.....	3
2.1 Schematic illustration of Seebeck effect circuit between two dissimilar materials with junctions held at different temperatures.....	10
2.2 (a) The n-type semiconductor is biased externally creating an electrical current. The negative carriers (electrons) carry heat from bottom to top via the Peltier effect. (b) The positive carriers (holes) within a p-type semiconductor–biased in the same direction as (a) pump heat in the opposite direction, that is, from top to bottom .....	12
2.3 Schematic diagram of Thomson effect.....	13
2.4 Seebeck effect for the power generation, an applied temperature difference causes charge carriers in the material (electrons or holes) to diffuse from the hot side to the cold side, resulting in current flow through the circuit .....	16
2.5 Peltier effect for the active refrigeration, heat evolves at the upper junction and is absorbed at the lower junction when a current is made to flow through the circuit .....	17
2.6 Variation of the transport coefficients as a function of the carrier concentration .....	18
2.7 Classification of nanoscale dimensions .....	26
2.8 A plot of price in dollars per mole (a) and (b) efficiency ratio for various high-temperature TE materials .....	29
2.9 Statistics on review papers from 1995 to 2018 on ScienceDirect on requires “Thermoelectric”, “Thermoelectric oxide”, and “Thermoelectric oxide nano” .....	29
2.10 Shows the current of ZT of $\text{Ca}_3\text{Co}_4\text{O}_9$ from 2000–2021 .....	30
2.11 Shows the current of ZT of $\text{CaMnO}_3$ from 2006–2022 .....	36

## LIST OF FIGURES (Continued)

Figure	Page
2.12 (a) Schematic principle of a TEG. (b) Schema of a typical TEG in practice	38
2.13 Schematic principles of typical thermoelectric generator (a) $\pi$ -shape traditional (b) segmented structure and (c) multilayer structure	41
2.14 Images of the fabricated segmented HH/CCO legs	42
2.15 Schematic of the whole thermoelectric module construction process from sintering and characterized materials to modelling, built up and test modules	43
2.16 Schematic drawings of (a) steps of forming segmented YBCO–CCO ceramic, (b) XRD analysis of YBCO–side and CCO–side and (c) sample preparation for SEM/EDS analyses	44
2.17 Schematic drawing of a multilayer thermoelectric	45
2.18 Show Structure of the multilayer cofired ceramics	45
3.1 The schematic diagram of methodology	55
3.2 Planetary ball milling apparatus of Retsch, PM–400 at Sakon Nakhon Rajabhat University and working principle of planetary ball mill (a) overall layout of planetary disk (b) horizontal section of grinding jar	60
3.3 The temperature profile for hot pressing of $\text{CaMnO}_3$	61
3.4 The temperature profile for hot pressing of $\text{Ca}_3\text{Co}_4\text{O}_9$	63
3.5 The hot press furnace OTF–1200x–VHP–4 model at Sakon Nakhon Rajabhat University and schematic view of hot press machine and working chamber	65
3.6 Diffraction (i.e. constructive interference of the scattered X-rays) will occur if the Bragg condition (eq. 3) is fulfilled and of the scattering vector $K$ is parallel to the normal of the $hkl$ -planes	67

## LIST OF FIGURES (Continued)

Figure	Page
3.7 X-ray diffractometer of Center of Excellence on Alternative Energy at Sakon Nakhon Rajabhat University .....	68
3.8 The FE-SEM observations were performed on a JEOL Ultra-high Resolution Scanning Electron Microscope JSM-7610FPlus at Ubon Ratchathani University and preparation the powder and bulk n-CaMnO <sub>3</sub> and p-Ca <sub>3</sub> Co <sub>4</sub> O <sub>9</sub> materials (drop casting and coating) .....	70
3.9 The schematic diagram semi-in Lens objective lens of the FE-SEM equipment .....	70
3.10 The schematic diagram high power optics of the FE-SEM equipment .....	71
3.11 The Seebeck Coefficient / Electric Resistance Measurement System .....	72
3.12 Schematic diagram of the step detail for Seebeck coefficient and electrical resistivity measurement .....	73
3.13 The schematic diagram of Seebeck coefficient and electrical resistivity measurement .....	74
3.14 Schematic of the whole thermoelectric segmented module construction process from sintering and characterized materials to modelling for measurements, built-up and test modules .....	78
3.15 Model design of segmented thermoelectric device configuration .....	78
3.16 Schematic joining steps in diffusion bonding and brazing/soldering methods and comparison between them .....	83
3.17 Sources of contact resistance in a TEG .....	84
3.18 Schematic principle of the thermoelectric generator tester .....	85
3.19 Photo of the TEG thermoelectric output test system .....	86
4.1 XRD pattern of CaMnO <sub>3</sub> samples with ball-milled, calcined and sintered ....	91
4.2 SEM image of CaMnO <sub>3</sub> powder after (a) ball-milling (b) calcined and (c) sintered .....	93

## LIST OF FIGURES (Continued)

Figure	Page
4.3 Elemental mapping of $\text{CaMnO}_3$ surface bulk sample .....	95
4.4 Dependence of $S$ on the temperature of the nanocrystalline $\text{CaMnO}_3$ sample .....	97
4.5 Dependence of $\rho$ on the temperature of the nanocrystalline $\text{CaMnO}_3$ sample .....	98
4.6 Dependence of thermoelectric power factor $\sigma S^2$ on the temperature of the nanocrystalline $\text{CaMnO}_3$ sample .....	99
4.7 Dependence of the $K$ on the temperature of on the temperature hot-pressed method .....	99
4.8 Dimensionless figure of merit (ZT) of the $\text{CaMnO}_3$ sample .....	101
4.9 XRD patterns of the (a) precursors; $\text{CaCO}_3$ nanoparticles, (b) $\text{Co}_3\text{O}_4$ nanoparticles, (c) after ball-milled, (d) $\text{Ca}_3\text{Co}_4\text{O}_9$ powders prepared by calcination and (e) $\text{Ca}_3\text{Co}_4\text{O}_9$ powders prepared fast sintering by hot-press method. The vertical lines at the bottom axis represent various planes of $\text{Co}_2\text{O}_3$ , $\text{CaCO}_3$ , and $\text{Ca}_3\text{Co}_4\text{O}_9$ mentioned in ICDD No. 05-0586, 42-1476 and 21-0139, respectively .....	103
4.10 XRD patterns expanded image peaks in range $2\theta = 29 - 32^\circ$ , the broad peaks of the mixed nano precursor powders after ball milled .....	104
4.11 SEM micrographs of the precursors, (a) $\text{CaCO}_3$ nanoparticles, (b) $\text{Co}_2\text{O}_3$ nanoparticles, and (c) ball-milled the mixed nano precursors powder after ball milling showing aggregates of nanoparticles (d) calcined powder .....	107
4.12 SEM micrographs of the $\text{Ca}_3\text{Co}_4\text{O}_9$ fast-sintering sample .....	108
4.13 (a) FE-SEM cross-sectional view of the fracture surface of the pellets, (b) images of the elemental compositional deviation (the colors indicate green (Co), orange (Ca), and red (O)), (c) EDX spectra of bulk $\text{Ca}_3\text{Co}_4\text{O}_9$ .....	109

## LIST OF FIGURES (Continued)

Figure	Page
4.14 Dependence of the $S$ on the temperature of the $\text{Ca}_3\text{Co}_4\text{O}_9$ sample was synthesized by fast sintering with hot-pressed method .....	111
4.15 Dependence of the $\rho$ on the temperature of the $\text{Ca}_3\text{Co}_4\text{O}_9$ sample was synthesized by fast sintering with hot-pressed method .....	112
4.16 Temperature dependence of the power factor of the $\text{Ca}_3\text{Co}_4\text{O}_9$ sample .....	113
4.17 Dependence of the $K$ on the temperature of on the temperature of the $\text{Ca}_3\text{Co}_4\text{O}_9$ sample was synthesized by fast sintering with hot-pressed method .....	115
4.18 Dimensionless figure of merit (ZT) of the $\text{Ca}_3\text{Co}_4\text{O}_9$ sample .....	116
4.19 Schematic of the whole thermoelectric segmented module construction process from sintering and characterized materials to modelling for measurements, built-up and test modules .....	117
4.20 Thermoelectric multilayers devices of (a) 1 pair designed and real fabrication, (b) 2 pairs series circuit and real fabrication, and (c) 2 pairs parallel circuit and real fabrication .....	118
4.21 (a) A proven picture of segmented CCO/CMO legs were successfully joined by silver brazing method and (b) chemical composition of CCO/Ag/CMO ceramic .....	120
4.22 Temperature dependence of the Seebeck coefficient and power factor of n- $\text{CaMnO}_3$ and p- $\text{Ca}_3\text{Co}_4\text{O}_9$ 1 pair module fabrication .....	121
4.23 The V-I and P-I curves of 1 pair thermoelectric multilayer module as a function of temperature difference at $T_h = 497$ K .....	124
4.24 The V-I and P-I curves of 2 pair thermoelectric multilayer as a function of temperature difference at $T_h = 523$ K .....	125
4.25 The V-I and P-I curves of 2 pair thermoelectric module as a function of temperature difference at $T_h = 513$ K .....	126

# CHAPTER 1

## INTRODUCTION

Introduction of this research composed of motivation, research objectives, scope and limitation and anticipated outcomes of the thesis.

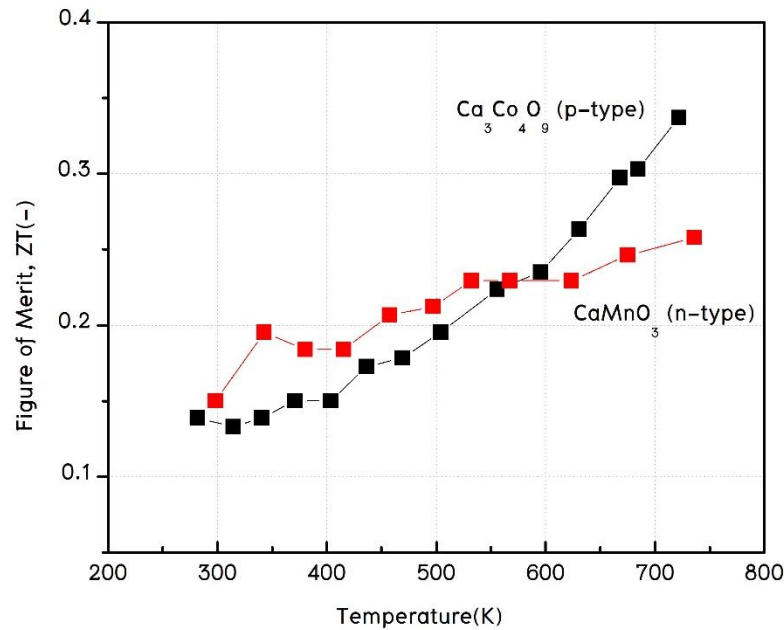
### **Motivation**

The thermoelectric is the most popular installs to convert waste heat streams from industrial into power generation processes. Thermoelectrics can have payback times as short as one year in the best applications (Energy.com, 2013). Thermoelectric is considered as one of the most promising and emerging clean energy technologies due to heat pump group can conversion technology is receiving increasing attention due to the worldwide energy and environment problems, and great progress has been made in the development of high-performance thermoelectric materials (He, 2017, pp.1000e102). Thermoelectric conversion is applied to areas as diverse as high-efficiency and high-precision temperature regulation, utilization of waste heat from automobiles and factories, and the use of body and ambient heat for the internet of things power generation is expected to play a crucial role in meeting the environmental and energy challenges of today and tomorrow as well as in creating safe living environments and in forging new industries. However, compared to that of conventional mechanical devices, the efficiency of the performance of thermoelectric is still low. These are reasons for the growing interest in further research and development of thermoelectric technology.

Since 1990s, oxide thermoelectric materials have been considered as promising thermoelectric (TE) materials due to their non-toxicity, low-cost, and

chemical stability at high temperatures in oxidizing atmospheres and are often composed of abundant elements, which are non-toxic in their oxidized form. Studied results show great potential for applications in thermoelectric power generator (TEG) at high temperature and thus have drawn attention over the years. However, oxides TEGs are still not used broadly due to their low performance. This thesis targets the research and development of exploring the use of these materials in high temperatures range using high conversion efficiency TEG based modules. This study demonstrates an effective way to improve the efficiency of oxide TEG by segmentation of oxide materials with other high-performance non-oxide materials, thereby, extending the temperature range. Among thermoelectric oxide materials, p-type of layered-cobaltite  $\text{Ca}_3\text{Co}_4\text{O}_9$  and n-type of perovskite  $\text{CaMnO}_3$  have been intensively investigated and considered as promising candidates for high temperature applications. The p-type and n-type of oxides materials combine promising ZT values with low material cost and allow an environmentally friendly and safe application in the air. Figure. 1.1. shows the timeline of representative p-type and n-type TE oxides and their maximum figure of merit values. The state-of-the-art p-type oxide TE materials are the layered cobaltite, such as  $\text{Ca}_3\text{Co}_4\text{O}_{9-\delta}$ , which has been reported to show ZT values of 0.45 at 1000 K (Nong, et al., 2010, pp. 53–56) and 0.65 at 1247 K (Nong, et al., 2011, pp. 2484–2490). For n-type oxide TE materials, the commonly used materials include calcium manganate ( $\text{CaMnO}_3$ ) (Flahaut, et al., 2006, pp. 084911).  $\text{CaMnO}_3$  can be used up to high-temperature (above 1000 K) applications, although their ZT are still relatively low at around 0.3 (Bocher, et al., 2008, pp. 8077–8085).





**Figure 1.1** ZT of  $\text{Ca}_3\text{Co}_4\text{O}_9$  (Nong, *et al.*, 2010, pp. 53–56 Nong, *et al.*, 2011, pp. 2484–2490) and  $\text{CaMnO}_3$  oxide thermoelectric materials (Flahaut, 2006, pp. 084911 Bocher, *et al.*, 2008, pp. 8077–8085).

For all these oxides, the major issue is the too large thermal conductivity, and the research on how to reduce thermal conductivity has been the most active in this field in the last 20 years. Several approaches have been followed, such as the reduction of the grain size and increase of grain boundaries scattering. Furthermore, the researcher demonstrated the enhancement of thermoelectric performance oxide thermoelectric materials via a decrease of grain size by nanoscale texturing and engineered interfaces. This strategy modified the crystal structure of oxide materials and induced phonon scattering by point defects, leading to lower thermal conductivity. Nanoscale texturing along c-axis provided advantage of higher electrical conductivity and reduce thermal conductivity in hot-pressing or spark plasma sintering samples, enhancing the thermoelectric properties response (enhanced ZT) (Song, *et al.*, 2018, pp. 10798–10810).

The conversion efficiency of a TE material is related to the dimensionless figure of merit,  $ZT$  and  $T$  are temperature dependent. However, now there are no single materials that can maintain high thermoelectric performance in its whole service temperature range. Although many combinations of p–n couples have been employed in the oxide modules, its performance i.e., voltage and current output are still relatively low compared with modules constructed from metallic alloys. Even the experimental value of the conversion efficiency has not been reported yet on those oxide modules. For example, Matsubara I., et al. reported that the p– $\text{Ca}_{2.7}\text{Bi}_{0.3}\text{Co}_4\text{O}_9$ /n– $\text{Ca}_{0.92}\text{La}_{0.08}\text{MnO}_3$  couples had the output power of 63.5 mW at  $\Delta T = 390$  K (Matsubara, *et al.*, 2001, pp. 3627–3629). While, Urata S., et al., showed the highest output power of p– $\text{Ca}_{2.7}\text{Bi}_{0.3}\text{Co}_4\text{O}_9$ / n–  $\text{CaMn}_{0.98}\text{Mo}_{0.02}\text{O}_3$  about 170 mW at  $\Delta T = 565$  K (Urata. *et al.*, 2006, pp. 535–540). Then, Funahashi, *et al.*, reported the maximum output power of p– $\text{Ca}_{2.7}\text{Bi}_{0.3}\text{Co}_4\text{O}_9$ / n–  $\text{CaMn}_{0.98}\text{Mo}_{0.02}\text{O}_3$  about 340 mW at  $\Delta T = 975$  K (Funahashi, *et al.*, 2007, pp. 297–307). These results show that many combinations of p–n oxide couples have been doped with alloy elements for increasing the performance of oxide materials. However, the highest estimated number is still lower than 2% (Hung, *et al.*, 2015, pp. 1143–1151). One of the main reasons for this low result is the low performance of oxide materials in the low temperature range ( $< 750$  K). To overcome the limitation mentioned above, new strategies on improved material of  $ZT$  and a new concept in module design and fabrication are needed. To increase the overall performance of TE devices, combining different TE materials whose optimum working temperatures are successively distributed is a promising approach.

To realize this, segmentation is the one approach that has been suggested for TE modules. In a multilayer leg, each p– and n–leg is constructed from at least two different p– and n–materials, respectively, that is the materials in a leg are joined together electrically and thermally in series. In this structure, the p– and n–legs of each TEG can be made either from a single material or by segmentation fabricated by

a single p- and n-type thermoelectric materials in the perpendicular direction. (Pham, *et al.*, 2015, pp. 124). A high-temperature material can be used for the hottest stage ( $>750$  K) and then a material with high electrical and thermal conductivity. The result from thermoelectric researchers demonstrates an effective way to improve the efficiency of oxide TEG by segmentation of oxide materials with other high-performance non-oxide materials, thereby, extending the temperature range.

Up to now, no detailed reports are available on the p-n horizontal multilayer oxide module under the same leg. We report new innovative high temperature TEG of layered-cobaltite  $\text{Ca}_3\text{Co}_4\text{O}_9$  and of perovskite  $\text{CaMnO}_3$ . In terms of a I-V testing circuit, measurements are routine since the magnitudes of the voltage (V) and current (A) can be measured by standard digital multimeters. The generated voltage and current are scanned on different points to get the I-V curves or operate the TEG under a dynamic load. The multilayer TEG improve maximum output power was achieved for this type at a  $\Delta T = 473$  K.

## Research Objectives

1. To synthesis nanocrystalline size of calcium cobalt oxides ( $\text{Ca}_3\text{Co}_4\text{O}_9$ ) and calcium manganese oxides ( $\text{CaMnO}_3$ ) bulk materials by planetary ball mill and hot-pressing method.
2. To study the effect of nano-sized precursors on the microstructure and thermoelectric properties of  $\text{Ca}_3\text{Co}_4\text{O}_9$  and  $\text{CaMnO}_3$ .
3. To fabricate and investigate multilayer thermoelectric generator from p- $\text{Ca}_3\text{Co}_4\text{O}_9$  and n- $\text{CaMnO}_3$  thermoelectric materials.

## Scope and Limitation of the Thesis

1. Precursor powder of calcium carbonate ( $\text{CaCO}_3$ ), cobalt oxide ( $\text{Co}_2\text{O}_3$ ), and Manganese oxide ( $\text{MnO}_2$ ) are nano powders which used to preparation by solid state reaction method within planetary ball mill and hot-pressing process for bulk materials.
2. The microstructure characterization composed of phase identification, morphology and chemical compositions using XRD, FE-SEM and EDS
3. Thermoelectric properties viz., Seebeck coefficient, electrical conductivity, power factor, thermal conductivity, and dimensionless figure of merit.
4. Thermoelectric generator was fabricated multilayer of p- $\text{Ca}_3\text{Co}_4\text{O}_9$  and n- $\text{CaMnO}_3$  thermoelectric materials using silver sheet electrode by brazing joining method.
5. The electrical power composed of electrical voltage, electrical current and electrical power output measuring 298 K to  $\Delta T = 473$  K.

## Anticipated Outcomes of the Thesis

1. Bulk thermoelectric materials of p- $\text{Ca}_3\text{Co}_4\text{O}_9$  and n- $\text{CaMnO}_3$ .
2. The effect of nano-sized precursors could be enhanced the thermoelectric properties
3. New multilayer of oxide thermoelectric generator prototype.
4. International paper publications.

## Financial support

Financial supported by “National Research Council of Thailand (NRCT) through the Royal Golden Jubilee (RGJ) Ph.D. Program (Grant No. PHD/0065/2560)”.

## References

- Bocher, L., Aguirre, M. H., Logvinovich, D., Shkabko, A., Robert, R., Trottmann, M., & Weidenkaff, A. (2008).  $\text{CaMn}_{1-x}\text{Nb}_x\text{O}_3$  ( $x \leq 0.08$ ) perovskite-type phases as promising new high-temperature n-type thermoelectric materials. *Inorganic chemistry*, 47(18), 8077–8085.
- Energy.com, C. (2013). WASTE HEAT RECOVERY. Retrieved from [http://coolenergy.com/waste-heat-recovery/].
- Flahaut, D., Mihara, T., Funahashi, R., Nabeshima, N., Lee, K., Ohta, H., & Koumoto, K. (2006). Thermoelectrical properties of A-site substituted  $\text{Ca}_{1-x}\text{Re}_x\text{MnO}_3$  system. *Journal of Applied Physics*, 100(8), 084911.
- Funahashi R, Urata S. Fabrication and Application of an Oxide Thermoelectric System. *Int J Appl Ceram Technol* 2007;4:297–307. doi:DOI: 10.1111/j.1744-7402.2007.02144.x.
- He, Z. (2017). Nanostructured Thermoelectric Materials with Improved Performance for Energy Conversion. *J Mater Sci Nanomater*, 1(e102).
- Hung, L. T., Van Nong, N., Han, L., Bjørk, R., Ngan, P. H., Holgate, T. C., ... & Pryds, N. (2015). Multilayer thermoelectric oxide-based module for high-temperature waste heat harvesting. *Energy Technology*, 3(11), 1143–1151.
- Matsubara I, Funahashi R, Takeuchi T, Sodeoka S, Shimizu T, Ueno K. Fabrication of an all-oxide thermoelectric power generator. *Appl Phys Lett* 2001;78:3627. doi:10.1063/1.1376155.
- Nong, N. V., Liu, C. J., & Ohtaki, M. (2010). Improvement on the high temperature thermoelectric performance of Ga-doped misfit-layered  $\text{Ca}_3\text{Co}_{4-x}\text{Ga}_x\text{O}_{9+\delta}$  ( $x = 0, 0.05, 0.1, \text{ and } 0.2$ ). *Journal of Alloys and Compounds*, 491(1–2), 53–56.
- Nong, N.V., Pryds, N., Linderth, S., Ohtaki, M., 2011. Enhancement of the thermoelectric performance of p-Type layered Oxide  $\text{Ca}_3\text{Co}_4\text{O}_{9+\delta}$  through heavy doping and metallic nano inclusions. *Adv. Mater.* 23 (1), 2484–2490. <https://doi.org/10.1002/adma.201004782>.

Pham, H. N. (2015). Design and Optimization of Effective Multilayer Thermoelectric Generator for Waste Heat Recovery.

Song, M. E., Lee, H., Kang, M. G., Li, W., Maurya, D., Poudel, B., ... & Priya, S. (2018). Nanoscale texturing and interfaces in compositionally modified  $\text{Ca}_3\text{Co}_4\text{O}_9$  with enhanced thermoelectric performance. *ACS omega*, 3(9), 10798–10810.

Urata S, Funahashi R, Mihara T. Power generation of p-type  $\text{Ca}_3\text{Co}_4\text{O}_9$ /n-type  $\text{CaMnO}_3$  module. 2006 25<sup>th</sup> Int. Conf. Thermoelectric., IEEE; 2006, p. 501–4. doi:10.1109/ICT.2006.331343

## CHAPTER 2

### THEORY AND LITERATURE REVIEWS

This chapter reviews the history and background of the thermoelectric effect, thermoelectric performance, functions of thermoelectric effects, Optimizing the figure of merit,  $ZT$  and thermoelectric parameters presented the three thermoelectric effects which are Seebeck effect, Peltier effect, and Thomson effect. Section of key differences between nanomaterials and bulk materials and compatibility and efficiency ratio of oxide thermoelectric materials. Section of current research of thermoelectric of n-CaMnO<sub>3</sub> and p-Ca<sub>3</sub>Co<sub>4</sub>O<sub>9</sub> materials. Last section of thermoelectric generators presents the energy conversion efficiency of multilayer bulk thermoelectric modules and overview of the oxide multilayer generator and their relevant fabrication techniques.

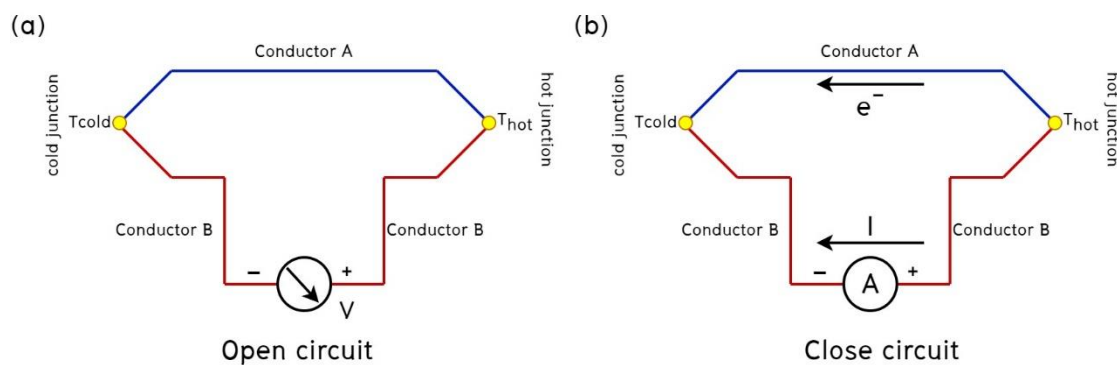
#### Thermoelectric Effects

Thermoelectric has a long history of providing simple, reliable power generation solution. The thermoelectric generator is made of semiconductor too which are direct conversion of temperature differences to electric voltage and vice versa. This chapter reviews briefly of the state-of-art the thermoelectric phenomena including the Seebeck effect, Peltier effect, and Thomson effect. Moreover, the Figure of Merit and Dimensionless, Figure of Merit relating to thermoelectric materials are used to further describe the properties of these materials.

#### Seebeck Effect

In 1821, Thomas Johann Seebeck, a German–Estonian physicist, found that a voltage existed between two ends of a metal bar when a temperature difference

$\Delta T$  existed in the bar (see Figure 2.1(a)). This effect is the conversion of temperature differences directly into electricity, called the Seebeck effect. Seebeck also discovered that a compass needle would be deflected when a closed loop was formed of two metals with a temperature difference between the junctions (see Figure 2.1(b)). This is because the metals respond differently to the temperature difference, which creates a current loop. When a steady temperature gradient is maintained along the bar of the thermoelectric material, the free charge carriers at the hot end will have high kinetic energy and tend to diffuse to the cold end. The accumulation of the charges at the cold end results in a back electromotive force (EMF) which opposes a further flow of charge. The EMF is called the Seebeck emf or Seebeck voltage, which is the open circuit voltage when no current flows (Seetawan, *et al.*, 2006, pp. 314–317; Somkhunthot, *et al.*, 2007, pp. 20–26).



**Figure 2.1** Schematic illustration of Seebeck effect circuit between two dissimilar materials with junctions held at different temperatures (Rowe, 2005).

From Figure 2.1, if the temperature difference  $\Delta T = T_H - T_C$  between the two ends of a material is small, and the thermoelectric voltage  $\Delta V$  is seen at the terminals. Then the Seebeck coefficient, or thermoelectric power, or thermopower of a material is defined as (Rowe, 2005):



$$S = \frac{\Delta V}{\Delta T} \quad (4)$$

If the junctions of the metals A and B were maintained at two different temperatures  $T_H$  and  $T_C$ , where  $T_H > T_C$ , the potential difference  $\Delta V$  developed can be derived from:

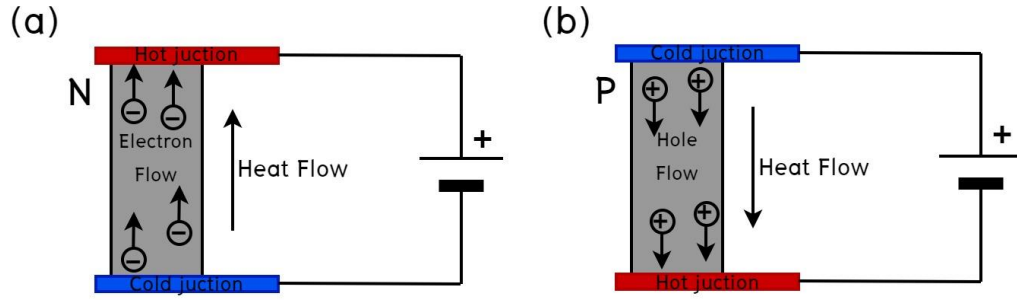
$$\Delta V = \int_{T_C}^{T_H} [S_B(T) - S_A(T)] dT \quad (5)$$

where  $S_A$  and  $S_B$  are the absolute Seebeck coefficients of the metals A and B, respectively. The Seebeck coefficients are non-linear, and depend on the conductors' absolute temperature, material, and molecular structure. It has a unit of V/K. If the Seebeck coefficients are effectively constant for the measured temperature range, Equation (5) can be approximated as:

$$\Delta V = (S_B - S_A) \cdot (T_H - T_C) \quad (6)$$

### Peltier Effect

The Peltier effect was observed in 1834 by Jean Charles Athanase Peltier, 13 years after Seebeck initial discovery. This effect is the reverse of the Seebeck effect; an electrical current would produce a temperature gradient at the junctions of two dissimilar metals or semiconductors (n-type and p-type).



**Figure 2.2.** (a) The n-type semiconductor is biased externally creating an electrical current. The negative carriers (electrons) carry heat from bottom to top via the Peltier effect. (b) The positive carriers (holes) within a p-type semiconductor-biased in the same direction as (a) pump heat in the opposite direction, that is, from top to bottom.

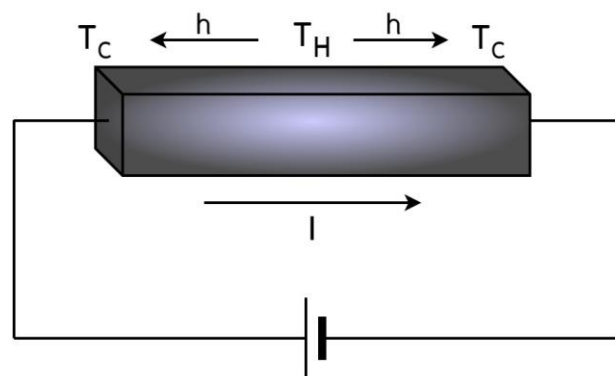
Consider the Peltier effect circuit in Figure 2.2; when a voltage is applied, a current  $I$  will flow through the circuit. In the case of n-type semiconductor, high energy electrons moved from negative end to positive end as shown in Figure 2.2(a). As a result, the thermal current and the electric current are in opposite directions. Consequently, the junction connected to positive terminal of the power supply will be heated up, while that connected to the negative terminal will be cooled down. The situation is opposite in the p-type as shown in Figure 2.2(b), the applied voltage causes holes to move from positive end to negative end. The thermal current and electric current are therefore in the same direction. In either case, the thermal current density  $Q$  is proportional to the electrical current density  $J$  :

$$Q = \Pi_{ab} \cdot J \quad (7)$$

where  $\Pi$  is the Peltier coefficients which represent how much heat current is carried per unit charge through a given material.

## Thomson Effect

When the electrical current density passes through a homogeneous conductor along which a temperature gradient is also maintained. In this case, when charge carriers flow in the direction of the temperature gradient  $\nabla T$ , both thermal and electrical currents are simultaneously present in the system and one may expect different behaviors to occur due to the coupling of these currents, depending upon whether  $h$  and  $j$  currents propagate in the same or the opposite sense. This phenomenon is well known as the Thomson effects which are dependent on the direction of both the electrical current density and temperature gradient as shown in Figure 2.3 (Rowe, 2005). This thermal effect results in the release or absorption of a certain amount of heat depending on the relative sense of the  $h$  and  $j$  currents, as well as on the material nature of the conductor.



**Figure 2.3** Schematic diagram of Thomson effect.

William Thomson (Lord Kelvin) was a Scottish mathematical physicist and engineer who described the heating or cooling of an electric current carrying conductor, the ends of which are maintained at different temperatures. In his original experimental setup, Thomson allowed an electrical current of intensity  $I$  to pass through an iron rod, which was bent into a U-shape. Two resistance coils,  $R_1$  and

$R_2$ , were wound about the two sides and connected to an external electrical circuit known as a Wheatstone bridge. This extremely sensitive circuit was initially balanced to determine any possible variation of the resistivity of these coils. The bottom of the U-shaped conductor was then heated with a burner. This establishes two temperature gradients, a positive one extending from A to C and a negative one extending from C to B. Consequently, the thermal and electrical currents run parallel (anti-parallel) in the CB (AC) arms, respectively. By inspecting the behavior of the Wheatstone bridge, Thomson observed that it became unbalanced, indicating that the resistance  $R_1$  has increased its value because of heat being liberated from the conductor. On the contrary, at the position of resistance  $R_2$  a certain amount of heat was absorbed by the conductor, so that some energy was supplied to the conductor at the expense of the thermal energy of the resistance. Therefore, carriers traversing the thermal gradient gain or release energy depending on their direction relative to  $\nabla T$ . He found that an extra amount of heat is evolved at a rate approximately proportional to the product of the current, and a temperature gradient, in addition to the well-known joule heat. This can be given by the relation:

$$q = \rho J^2 - \mu J \frac{dT}{dx} \quad (8)$$

where  $q$  is heat production per unit volume,  $\rho$  is the resistivity of the material,  $J$  is the electric current density,  $\mu$  is the Thomson coefficient in volt per Kelvin, and  $dT/dx$  is the temperature gradient along the wire. The first term  $\rho J^2$  is simply the Joule heating which is not reversible. While the second term  $\mu J(dT/dx)$  is the Thomson heat which changes sign when changes direction of  $J$ .

In 1854, Thomson found two relationships which called the Thomson or Kelvin relationships. The first Thomson relation is related to the  $\Pi$ ,  $S$ , and  $T$ :

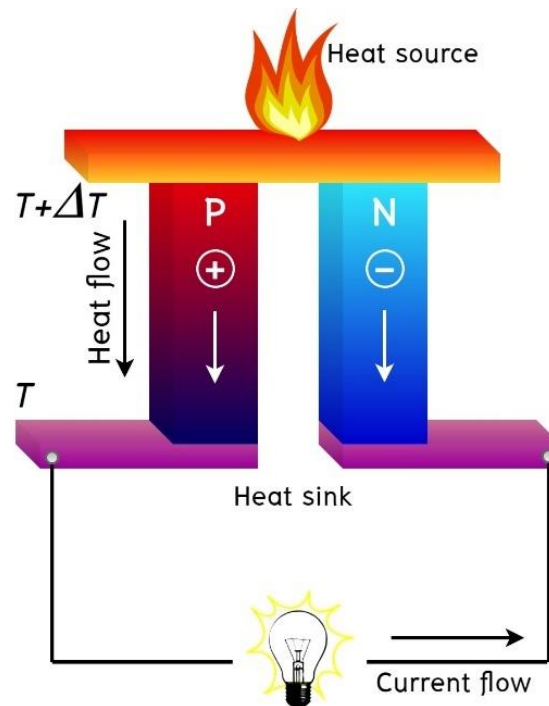
$$\Pi = S \cdot T \quad (9)$$

The second Thomson relation is related to the  $\mu$ ,  $S$  and  $T$ :

$$\mu = T \frac{dS}{dT} \text{ or } S = \int \frac{\mu}{T} dT \quad (10)$$

## Functions of Thermoelectric Effects

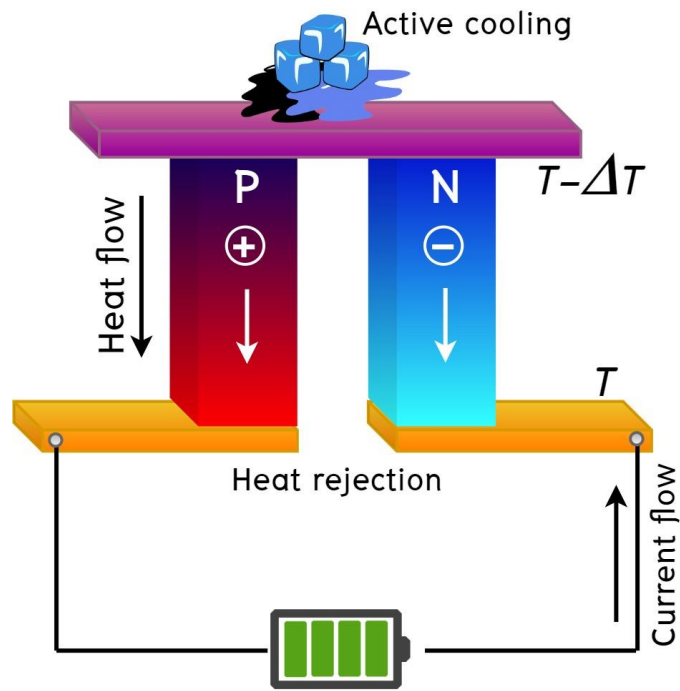
The most popular and classic TE application is a thermocouple. The power generation from heat of TE cell based on the Seebeck phenomenon. Thermoelectric cell is fabricated from two type of thermoelectric materials (p-type and n-type). Most of the semiconductor materials as the electrode connected serially called p-n junction. In other word when heating at the p-n junction of thermoelectric cell. The heat that flows through it varies by the type of thermoelectric material, which results in temperature differences and potential voltages between the two electrodes. It is caused by the flow of electrons and holes. And at the same time, it absorbs heat from the other side of the thermoelectric material and release it at the other end of the thermoelectric material. The hole flow of thermoelectric material is in the opposite direction to the flow of electrons, that is, when we heat the p-n junction. The flow of electrons and holes from the hot side to the cold side or the thermal absorption of the positive charge of the p-type material and then dissipate of the n-type material as shown in Figure 2.4.



**Figure 2.4** Seebeck effect for the power generation, an applied temperature difference causes charge carriers in the material (electrons or holes) to diffuse from the hot side to the cold side, resulting in current flow through the circuit.

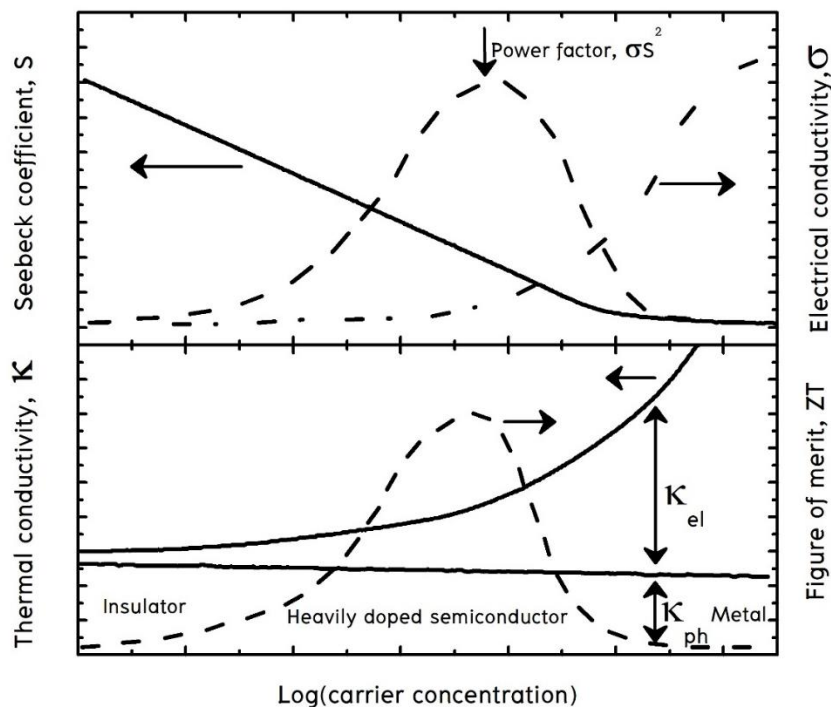
The Peltier coefficients represent how much heat is carried per unit charge. Since charge current must be continuous across a junction, the associated heat flow will develop a discontinuity if  $\Pi_A$  and  $\Pi_B$  are different. The Peltier effect can be considered as the back-action counterpart to the Seebeck effect (analogous to the back-emf in magnetic induction): if a simple thermoelectric circuit is closed, then the Seebeck effect will drive a current, which in turn (by the Peltier effect) will always transfer heat from the hot to the cold junction (Skripnik & Khimicheva, 1997, pp. 673–677). The close relationship between Peltier and Seebeck effects can be seen in the direct connection between their coefficients:  $\Pi = TS$ . A typical Peltier heat pump involves multiple junctions in series, through which a current is driven. Some of the junctions lose heat due to the Peltier effect, while others gain heat. Thermoelectric

heat pumps exploit this phenomenon, as do thermoelectric cooling devices found in refrigerators as shown in Figure 2.5.



**Figure 2.5** Peltier effect for the active refrigeration, heat evolves at the upper junction and is absorbed at the lower junction when a current is made to flow through the circuit.

## Optimizing the figure of merit, $ZT$ and Thermoelectric parameters



**Figure 2.6** Variation of the transport coefficients as a function of the carrier concentration.

Figure 2.6 shows the previously stated optimized  $ZT$ , which is one of the parameters used in the classification of materials is electrical conductivity. Metals have high electrical conductivity, while insulators have very low conductivity which under normal conditions is taken as zero. Semiconductors occupy an intermediate position between the two. Electrical conductivity reflects the charge carrier concentration. All three parameters which occur in the figure of merit are functions of carrier concentration (Spies, *et al.*, 2015). Electrical conductivity increases with an increase in carrier concentration, while the Seebeck coefficient decreases, and the electrical power factor maximizes at a carrier concentration of around  $10^{25} \text{ cm}^{-3}$ . The electronic contribution to the thermal conductivity  $\kappa_e$ , which in thermoelectric materials is generally around 1/3 of the total thermal conductivity, also increases with carrier



concentration. Evidently the Figure of Merit is optimized at carrier concentrations which corresponds to semiconductor materials. Consequently, semiconductors are the materials most researched for thermoelectric applications.

## Thermoelectric parameter

The thermoelectric materials harvesting energy by converting waste heat into electricity through different temperatures between the thermoelectric devices; this method is an attractive method to reduce greenhouse gas emission (Enescu, 2019). Thermoelectric devices can convert heat into electricity or transport heat producing cooling using the Seebeck and Peltier effects. The efficiency of process typically determines the utility and cost of such devices and even the power density (Snyder, *et al.*, 2017, pp. 2280–2283). This performance of thermoelectric materials can be predicted via consideration the dimensionless figure of merit ( $ZT$ ).

$$ZT = \frac{S^2 T}{\rho \kappa} \quad (11)$$

where  $S$  is the Seebeck coefficient (V/K),  $T$  is the absolute temperature,  $\rho$  is the electrical resistivity ( $\Omega \text{ m}$ ) and  $\kappa$  is the thermal conductivity (W/mK). The figure of merit  $ZT(T)$  is, in general, a temperature dependent material property derived from temperature dependent material properties  $S(T)$ ,  $\rho(T)$ , and  $\kappa(T)$ . An efficient thermoelectric generator, however, must operate across a finite temperature difference  $\Delta T = T_h - T_c$  so that these material properties will change from the hot to the cold end. The relationships of  $S$ ,  $\rho$  and  $\kappa$  are the most important factors leading to high or low  $ZT$  values of thermoelectric materials with a drastic dependence on carrier concentration, the electrical and thermal conductivity increase, while the Seebeck coefficient decreases with increasing carrier concentration

## Seebeck coefficient

One way to define the Seebeck coefficient is the voltage built up when a small temperature gradient is applied to a material, and when the material has come to a steady state where the current density is zero everywhere. If the temperature difference  $\Delta T$  between the two ends of a material is small, then the Seebeck coefficient of a material is defined as:

$$S = -\frac{\Delta V}{\Delta T} \quad (12)$$

where  $\Delta V$  is the thermoelectric voltage seen at the terminals.

Note that the voltage shift expressed by the Seebeck effect cannot be measured directly, since the measured voltage (by attaching a voltmeter) contains an additional voltage contribution, due to the temperature gradient and Seebeck effect in the measurement leads. The voltmeter voltage is always dependent on *relative* Seebeck coefficients among the various materials involved. Equation. 13. By utilizing thermodynamics of irreversible processes, Seebeck coefficient can be expressed as (Hilaal Alama, 2012, pp. 190–212):

$$S = \frac{8\pi^2 k_B^2}{3eh^2} m^* T \left( \frac{\pi}{3n} \right)^{\frac{3}{2}} \quad (13)$$

where  $k_B$  is the Boltzmann constant,  $e$  is electron charge,  $h$  is Planck's constant,  $m^*$  is the effective carrier mass,  $T$  is the absolute temperature and  $n$  is charge carrier concentration. Assuming that  $S$  is measured at constant temperature, the only variable in this equation will be carrier concentration  $n$  that can be varied through doping. By looking at the equation we can see that  $S$  will decrease when  $n$  increases. Reason for this is the fact that Seebeck effect is caused by the induced voltage in the material. The higher the carrier concentration to begin with the lower

the induced voltage as it takes less new electron–hole pairs to induce current flow through the material.

## Electrical Resistivity

In general, for intrinsic semiconductor the resistivity decreases with increasing temperature. The electrons are collision to the conduction energy band by thermal energy, where they flow freely, and in doing so leave behind holes in the valence band, which also flow freely (Lowrie, & Fichtner, 2020).

The electric resistance of a typical intrinsic (undoped) semiconductor decreases exponentially with temperature:

$$\rho = \rho_0 e^{-aT} \quad (14)$$

An even better approximation of the temperature dependence of the resistivity of a semiconductor is given by the Steinhart–Hart equation (Seymour 1972, pp. 53–54 34):

$$\frac{1}{T} = A + B \ln \rho + C (\ln \rho)^3 \quad (15)$$

where  $A, B$  and  $C$  are the so-called **Steinhart–Hart coefficients**.

Extrinsic (doped) semiconductors have a far more complicated temperature profile. As temperature increases starting from absolute zero, they first decrease steeply in resistance as the carriers leave the donors or acceptors. After most of the donors or acceptors have lost their carriers, the resistance starts to increase again slightly due to the reducing mobility of carriers (much as in a metal). At higher temperatures, they behave like intrinsic semiconductors as the carriers from the donors/acceptors become insignificant compared to the thermally generated carriers (Smith, 1972, pp. 78).

In non-crystalline semiconductors, conduction can occur by charges quantum tunnelling from one localized site to another (öer, & Pohl, 2017, pp. 1053–1087; : (Kabir, *et al.*, 2014, 7522–7528). This is known as variable range hopping and has the characteristic form of

$$\rho = A \exp \left( T^{-\frac{1}{n}} \right), \quad (16)$$

where  $n = 2, 3, 4$ , depending on the dimensionality of the system.

A normally of semiconductor exhibits thermally activated electrical resistivity ( $\rho$ ) that decreases with increasing temperature. Metals have very low electrical resistivity, typically above  $5 \times 10^{-4} \Omega \text{ cm}$  that increases as the temperature increases. However, non-degenerate semiconductors exhibit a resistivity that decrease with temperature, but the magnitude is much higher than for a metal, and typically in the range of  $10^{-4}$  to  $10^5 \Omega \text{ cm}$  depending on the band gap. Insulators have resistivity greater than  $10^7 \Omega \text{ cm}$ .

## Thermal Conductivity

The **thermal conductivity** of a material is a measure of its ability to conduct heat. It is commonly denoted by  $k, \lambda$ , or  $\kappa$

Heat transfer occurs at a lower rate in materials of low thermal conductivity than in materials of high thermal conductivity. For instance, metals typically have high thermal conductivity and are very efficient at conducting heat, while the opposite is true for insulating materials. Correspondingly, materials of high thermal conductivity are widely used in heat sink applications, and materials of low thermal conductivity are used as thermal insulation. The reciprocal of thermal conductivity is called thermal resistivity. The thermal conductivity of a materials is mainly the sum of two components: the lattice (phonon) component,  $\kappa_{ph}$ , and the electronic component,  $\kappa_e$ .

As a result, the total thermal conductivity,  $\kappa_{tot}$  is defined as a sum of the electronic and lattice component.

$$\kappa = \kappa_e + \kappa_{ph} \quad (17)$$

Therefore, in semiconducting materials a finite maximum of the thermoelectric power factor is achieved. As a result, the most effective way to enhance the thermoelectric figure of merit of bulk materials is to decrease the lattice contribution to the thermal conductivity  $\kappa_l$ . However, thermal conductivity reduction, without decreasing the power factor, was not possible for a long time (in all efforts up to the 1990s), and the  $ZT$  values were limited to unity. This translates to low conversion efficiencies and limited applications for thermoelectricity.

**The electrical thermal conductivity** can be expressed as

$$\kappa_e = \frac{LT}{\rho} \quad (18)$$

This contribution, due to electrons or holes that carry heat in the system, is insignificant at very low doping levels but becomes more important as the number of charge carrier increases. The electronic participation of the thermal conductivity is given by the Wiedemann–Franz law as a function of the electrical resistivity  $\rho$ , the absolute temperature,  $T$ , and the Lorentz number,  $L = 2.4453 \times 10^{-8} \text{ W}\Omega/\text{K}^2$ . Another illustrative equation is the Wiedemann–Franz relationship s (Bhaskar, A., Liu, C.–J., Yuan, J. J., & Chang, C.–L., 2013, pp. 236–239):

$$\kappa_e = \left( \frac{k_B}{e} \right)^2 \frac{LT}{\rho} \quad (19)$$

where  $e$  is charge of an electron and  $k_B$  is the Boltzmann's constant.

### The lattice thermal conductivity

Lattice vibrations are independent of the carrier concentration the lattice thermal conductivity increases rapidly and becomes less significant in materials with high carrier concentration because the electronic thermal conductivity is the dominating process (Sootsman, Chung, & Kanatzidis, 2009, pp. 8616–8639).

$$\kappa_{ph} = \frac{1}{3} C_V v l_{ph} \quad (20)$$

where  $C_V$  is the heat capacity at constant volume,  $V$  is the concentration and velocity of phonons and  $l_{ph}$  is the phonon mean free path, which is defined as the average distance a phonon travels before colliding with another particle. The evolution of  $\kappa_{ph}$  with the temperature depends on the dominating interactions occurring in the lattice. At low temperatures those limitations are caused by the grain size and the defect concentration while at high temperatures, collisions between phonons are the dominant factor limiting heat conduction.

### Enhancement of $ZT$ with nanomaterials

Nanostructuring of materials is a key topic in many of today's research fields. Popular techniques to produce nanometric structures can be classified as top-down strategies or bottom-up growth mechanisms. Self-assembled and self-organized structures are important owing to the elementary fabrication processes. A special interest exists in the changing properties of the material due to the nanoscopic size compared with bulk materials. Because of these emerging new properties, nanostructured materials and especially semiconductors are of paramount importance.

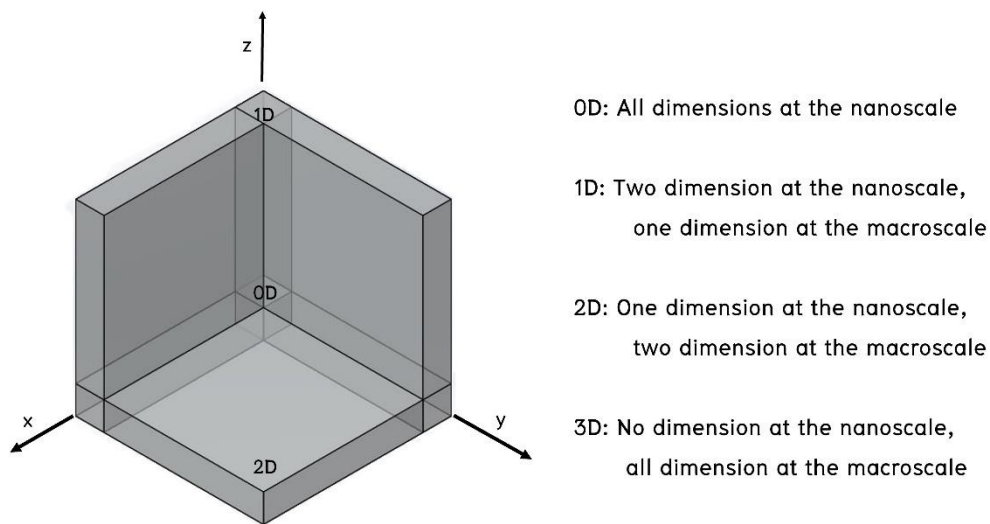
The idea of nano-engineering the materials to enhance their thermoelectric properties began when scientists predicted that introduction of defects at the nano level could interrupt the flow of phonon by selective-site scattering i.e. quantum dots

and wire, which resulted in a decrease in thermal conductivity and lead to a higher figure of merit (Harman *et al.*, 2002, pp. 2229–2232). Furthermore, not only dispersed defects but also a layer of thin-film or a specific array of nanowires could be coated onto the thermoelectric material which could potentially alter its electronic state e.g. Fermi energy level etc., and lead to more favorable electrical characteristics (Böttner, Chen, & Venkatasubramanian, 2006, pp. 211–217). Research literature suggests that nanomaterials have increased the figure of merit several folds (Dresselhaus *et al.*, 2007, 1043–1053; Shakouri & Zebbarjadi, 2009, pp. 225–299). The concept of nano-materials has been widely used in thin film thermoelectric materials and in some quantum dots (Böttner *et al.*, 2006; Harman *et al.*, 2002, pp. 2229–2232) (Minnich *et al.*, 2009, pp. 466–479; Shakouri & Zebbarjadi, 2009, pp. 225–299).

### **Dimensions of nanomaterials**

This nanomaterial classification is based on the number of dimensions of a material, which are outside the nanoscale (<100 nm) range.

The dimensionality of the materials, these are 4 nanostructures in the thermoelectric with improved the figure of merit as shown in figure 2.7; 0D nanodots, 1D nanowires, 2D quantum wells and superlattices and 3D nanomaterials and nanocomposites (Vineis *et al.*, 2010, pp. 3970–3980; Saleemi, 2014). For this thesis, 3D bulk thermoelectric materials have easier fabrication processes.



**Figure 2.7** Classification of nanoscale dimensions.

Accordingly, in zero-dimensional (0D) nanomaterials all the dimensions are measured within the nanoscale (no dimensions are larger than 100 nm). Most commonly, 0D nanomaterials are nanoparticles. In one-dimensional nanomaterials (1D), one dimension is outside the nanoscale. This class includes nanotubes, nanorods, and nanowires. In two-dimensional nanomaterials (2D), two dimensions are outside the nanoscale. This class exhibits plate-like shapes and includes graphene, nanofilms, nanolayers, and nanocoating. Three-dimensional nanomaterials (3D) are materials that are not confined to the nanoscale in any dimension. This class can contain bulk powders, dispersions of nanoparticles, bundles of nanowires, and nanotubes as well as multi-nanolayers.

Several years ago, the researchers have proposed the process to enhance the  $ZT$  value with the main approaches are focusing on either enhancement of the electrical conductivity, on lowering of the bulk thermal conductivity by decreasing the grain sizes when the grain diameter is less than 500 nm to the dimensionality of materials to 1D nanostructures would lead to large  $ZT$  increase. Nanostructured



materials can reduce phonon mean free path very effectively, however nanograins are also capable of reducing the electrical conductivity (Granitzer & Rumpf, 2014).

## Phonon Scattering

Phonon scattering is a phenomenon where the phonon mean free path through a material has been reduced; several factors can contribute to this effect. In the development of thermoelectric materials, there is a trade-off between the electrical and thermal conductivity (Chen, 2001, pp. 23). Phonon scattering has therefore become four key methods to reduce thermal conductivity without reducing the electrical conductivity and increasing phonon scattering in crystalline materials. Doping a material with elements to introduce lattice misfit and strain that increases phonon scattering without significant degradation of electrical conductivity. It also alters the band structure and electron mobility which might be favorable to thermoelectric properties (Ioffe, 1957). A second method to achieve phonon scattering is via 'rattling' crystal structures, where the crystal structure is engineered such that a dopant atom is surrounded by a 'cage' of atoms. The dopant-and cage atoms will have different vibrational frequencies at a given temperature leading to scattering of phonons (Trigo, Bruchhausen, Fainstein, Jusserand, & Thierry-Mieg, 2002, pp. 227402).

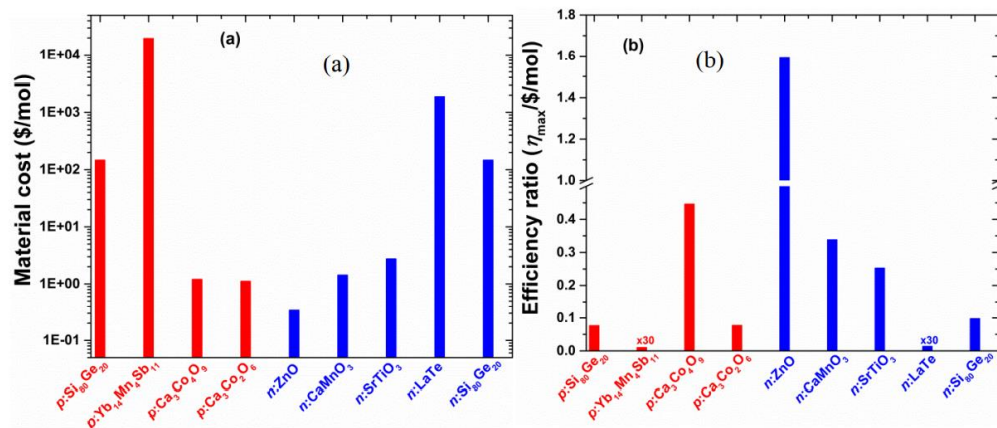
## The key differences between nanomaterials and bulk materials

Two principal factors cause the properties of nanomaterials to differ significantly from other materials: increased relative surface area, and quantum effects. These factors can change or enhance properties such as reactivity, strength, and electrical characteristics. As a particle decreases in size, a greater proportion of atoms are found at the surface compared to those inside. For example, a particle of size 30 nm has 5% of its atoms on its surface, at 10 nm 20% of its atoms, and at 3

nm 50% of its atoms. Thus, nanoparticles have a much greater surface area per unit mass compared with larger particles. As growth and catalytic chemical reactions occur at surfaces, this means that a given mass of material in nanoparticulate form will be much more reactive than the same mass of material made up of larger particles.

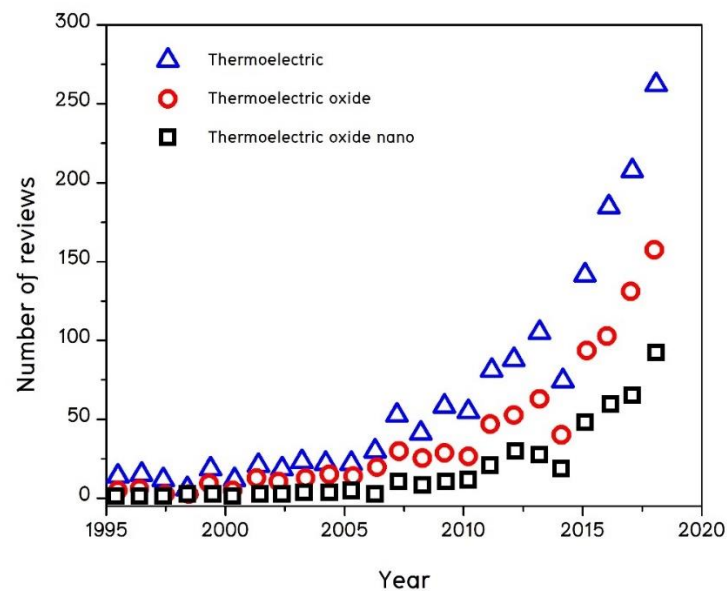
### **Compatibility and efficiency ratio of oxide thermoelectric materials**

For commercialization industries are interested in low-cost materials where the values are less than copper. Therefore, the researcher wants to developed other materials for industries but not low quality for example polymer, silicide, oxide materials. Figure 2.8(a) shows the materials cost per mol of oxide thermoelectric materials for p-type and n-type. Low-cost oxide materials of are  $\text{Ca}_3\text{Co}_4\text{O}_9$  or  $\text{Ca}_3\text{Co}_2\text{O}_6$  for p-type and  $\text{ZnO}$  and  $\text{CaMnO}_3$  for n-type. To ensure that high conversion efficiency of segmented or multilayer module the compatibility factor of thermoelectric materials must be first considered. The oxide materials such as  $\text{Ca}_3\text{Co}_4\text{O}_9$ ,  $\text{CaMnO}_3$  are environmentally friendly operating for high temperature usage. Although the peak ZT values of oxide materials are relatively low as compared with the intermetallic compounds, their chemical composition contains abundant elements and low-cost of raw material processing by focus on the efficiency ratio. As seen from Figure. 2.8(b) their efficiency ratios are higher by a factor of two for p-type and one for n-type materials as clearly. This results points out that  $\text{Ca}_3\text{Co}_4\text{O}_9$  and  $\text{CaMnO}_3$  nanocomposite are good candidates for low-cost for the fabrication high performance segmented legs or multilayers for the demonstration of energy conversion (Hung, *et al.*, 2015, pp. 1143–1151).



**Figure 2.8** A plot of price in dollars per mole (a) and (b) efficiency ratio for various high-temperature TE materials.

## Current Research of Thermoelectric, Thermoelectric Oxide and Thermoelectric Oxide Nano Materials



**Figure 2.9** Statistics on review papers from 1995 to 2018 on ScienceDirect on requires “Thermoelectric”, “Thermoelectric oxide”, and “Thermoelectric oxide nano” (Zavjalov, *et al.*, 2019, pp. 2895).

Particularly, Figure 2.9 shows the statistics of review papers from 1995 to 2018 on “Thermoelectric”, “Thermoelectric oxide” and “Thermoelectric oxide nano” queries. The annual amount of research has increased more than 20-fold (from 12 in 1995 to 260 in 2018). The highest publication activity in this field is happening now: From 2014, the number of published reviews grew by 40 every year, which corresponds to additional 1000 research papers. They are focused mainly on the thermoelectric properties of oxides and thermoelectric devices based on them (over 50% of papers have studied oxide systems since 2014).

### P-type Oxides; Calcium cobaltite

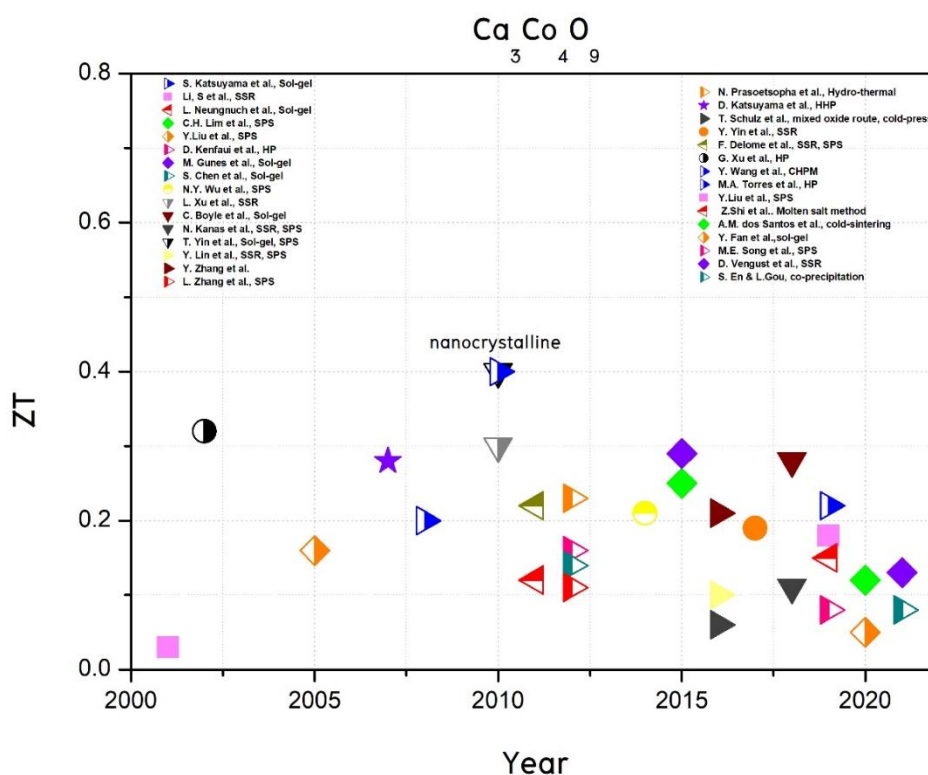


Figure 2.10 shows the current of  $ZT$  of  $\text{Ca}_3\text{Co}_4\text{O}_9$  from 2000–2021.

The p-type oxide thermoelectric materials are those based on metal-cobaltite compounds that form layered structures also referred as misfit oxide (Grebille *et al.*, 2007, pp. 373–383). The calcium cobaltite has been identified being  $\text{Ca}_3\text{Co}_4\text{O}_9$  (Koumoto, Terasaki, & Funahashi, 2006, pp. 1–23; Fergus, 2012, pp. 525–540). The Cobaltite Misfit-layered (ML) structures can be described with formula,  $[\text{M}_m\text{A}_2\text{O}_{m+2}]_q[\text{CoO}_2]$  ( $\text{M}=\text{Co}, \text{Bi}, \text{Pb}, \text{Ti}, \text{etc.}$ );  $\text{A}=\text{Ca}, \text{Sr}, \text{Ba}, \text{etc.}$ ;  $m=0, 1, 2$ ;  $q>0.5$ ) as purposed by Yamauchi *et al.* (Yamauchi, Sakai, Nagai, Matsui, & Karppinen, 2006, pp. 155–158). Two type of layer blocks: hexagonal (h) layer  $[\text{CoO}_2]$  and rock-salt (RS) layer  $[\text{M}_m\text{A}_2\text{O}_{m+2}]$  are stacked on each other forming a layer superstructure. The number of the cations is defined by  $m$ , and the misfit parameter ' $q = b_H/b_{RS}$ ' ( $b$  is defined as lattice parameter ' $b$ ' of respective layers along the perpendicular direction of stacking layer in the superstructure) is a ratio of mismatch between two layers. Typical values of the lattice parameters are  $a = 54.8376(7) \text{ \AA}$ ,  $c = 510.833(1) \text{ \AA}$ ,  $\beta = 98.06(1)^\circ$ ,  $b_2 = 4.5565(6) \text{ \AA}$ , and  $b_1 = 2.8189(4) \text{ \AA}$  (Büttner, 2017). At  $q = 0.5$  (or 1.0), a distinct commensurate structure shows at this specific misfit ratio. The hexagonal  $[\text{CoO}_2]$  layer, which shares edges of  $\text{CoO}_6$  polyhedral, is considered the basic common layer found in all multilayers.

The  $\text{Ca}_3\text{Co}_4\text{O}_9$  bulk was synthesized by hot pressed method at 1173 K for 1 h and annealed by furnace at 1173 K for 12 h. The electrical resistivity of sample is  $24.2 \text{ m}\Omega \text{ cm}$  at 373 K, Seebeck coefficient  $205 \text{ }\mu\text{V/K}$ , and power factor  $0.17 \text{ mW m}^{-1}\text{K}^{-2}$  at 873 K, respectively (Angnanon, 2020, pp. 469–472). F. Delorme *et al.* have shown the effect of micrometer, nanometer and mixing sized of precursors powder, which were prepared by solid state reaction and spark plasma sintering. The  $\text{Ca}_3\text{Co}_4\text{O}_9$  sample was synthesized from nanosized  $\text{CaO}$  — micro-sized  $\text{Co}_3\text{O}_4$  precursors leads to slightly higher electrical conductivity and higher power factor, meanwhile the thermal conductivity values are lower around  $1.65 \text{ W m}^{-1} \text{ K}^{-1}$  at 1000 K more than micro-sized  $\text{CaO}$  — micro-sized  $\text{Co}_3\text{O}_4$  sized precursors sample. The best  $ZT$  value was reached 0.18 at 973 K for the sample synthesized from nano sized  $\text{CaO}$  and micrometer sized  $\text{Co}_3\text{O}_4$  [Delorme, *et al.*, 2012, pp. 1169–1175]. The

$\text{Ca}_3\text{Co}_4\text{O}_9$  was prepared by powder synthesis with the solid-state reaction and conventional sintering. The  $\text{Ca}_3\text{Co}_4\text{O}_9$  microstructure has a strong texture of the  $\text{Ca}_3\text{Co}_4\text{O}_9$  platelets within lamination. The electrical conductivity of conventional sintering is 56 S/cm at 373 K. The thermal conductivity of  $\text{Ca}_3\text{Co}_4\text{O}_9$  sample is 1.3 W/(mK) at 373K.  $ZT$  of the  $\text{Ca}_3\text{Co}_4\text{O}_9$  sample increases with temperature and reaches about 0.11 at 873 K (Schulz, *et al.*, 2018, pp. 1600–1607). Gunes *et al.* analyzed the effect of grain size and porosity on thermal conductivity of  $\text{Ca}_3\text{Co}_4\text{O}_9$  ceramics with various grain sizes; nano-sized samples exhibit higher  $ZT$  values they report a thermal conductivity 0.32 W/(mK) at 300 K, decreasing with particle sizes. The  $ZT$  value reached 0.29 at 1273 K. The increase in  $ZT$  at high temperature is due to several factors. First, the thermal conductivity is already low and remains constant. Second, the Seebeck coefficient increases with temperature; however, the electrical transport behavior change, and resistivity decrease near 420 K, which substantially contributes to the enhancement of  $ZT$  at high temperature. The synthesized nano-sized samples exhibited higher electrical resistivity due to the quantity of pores, which increased the carrier scattering at boundaries, and the lower thermal conductivity due to phonon boundary scattering at the increased number of interfaces.  $ZT$  was enhanced due to the substantial decrease in the thermal conductivity despite the great increase in resistivity. The total thermal conductivity reduction was experimentally observed to be larger for smaller grain sizes and higher porosities. Because the size and morphology of materials strongly affect  $ZT$  values (Gunes, & Ozenbas, 2015, pp. 360–367). Miyazaki *et al.* reported the structure of  $[\text{Ca}_2\text{CoO}_3]_{0.62}\text{CoO}_2$  (Miyazaki *et al.*, 2002, pp. 491–497) by using solid-state reaction to prepare  $[\text{Ca}_2\text{CoO}_3]_{0.62}\text{CoO}_2$ . Similar to findings of Masset *et al.* (Masset *et al.*, 2000, pp. 166), it was reported that the compound consisted of two subsystems:  $\text{CdI}_2$ -type  $\text{CoO}_2$  (Co lattice also sharing an edge of the  $\text{CoO}_6$  octahedra) and distorted layers of rock salt type  $\text{Ca}_2\text{CoO}_3$ . The two subsystems were alternately stacked in the  $c$ -direction with an incommensurate misfit relationship in the  $b$ -axis. The  $[\text{Ca}_2\text{CoO}_3]_{0.62}\text{CoO}_2$  structure without modulation (fundamental or average structure)

was indexed and refined. Li et al. (Li *et al.*, 2000) were first to report the thermoelectric properties for  $\text{Ca}_3\text{Co}_4\text{O}_9$  and the effect of Bi substitution for Ca. The ceramics with the composition  $\text{Ca}_{3-x}\text{Bi}_x\text{Co}_4\text{O}_9$  ( $x= 0.0\text{--}0.75$ ) were prepared from  $\text{CaCO}_3$ ,  $\text{Bi}_2\text{O}_3$  and  $\text{Co}_2\text{O}_3$  powders by solid-state reaction. It was reported that the ‘a’ and ‘b’ lattice parameters increased while ‘c’ decreased with the increase in Bi content. The largest cell volume was found in  $x=0.3$  because the  $\text{Bi}^{3+}$  atom is larger than  $\text{Ca}^{2+}$ , However, for  $x>0.3$  the cell volume decreased; it was suggested that this could be due to structural change or oxygen content which led to a decrease in cell volume. For undoped  $\text{Ca}_3\text{Co}_4\text{O}_9$ , Seebeck coefficient of  $80\ \mu\text{VK}^{-1}$ , the resistivity of  $12\ \text{m}\Omega\cdot\text{cm}$  and thermal conductivity of  $1.8\ \text{Wm}^{-1}\text{K}^{-1}$  at room temperature were reported. However, substitution of Bi to Ca sites greatly improved the thermoelectric properties; compositions with  $x=0.5$  showed a  $ZT$  value of 0.2 at  $700\ ^\circ\text{C}$ . The reason for the improvement of the thermoelectric properties was stated that the substitution of Bi for Ca led to an increase in carrier mobility, therefore, resulted in a rise of both thermopower and electrical conductivity. In addition,  $\text{Bi}^{3+}$  is larger and heavier than  $\text{Ca}^{2+}$  leading to higher phonon scattering, thus reducing the thermal conductivity (Li *et al.*, 2000, pp. 2424–2427). The effect of texturing on the properties of calcium cobaltite was investigated by Hao et al. (Hao, He, Chen, Sun, & Hu, 2009, pp. 87–95). Two compositions,  $\text{Ca}_3\text{Co}_4\text{O}_9$  and  $\text{Ca}_{2.7}\text{Bi}_{0.3}\text{Co}_4\text{O}_9$ , were prepared by a solid-state reaction using  $\text{CaCO}_3$ ,  $\text{Bi}_2\text{O}_3$ , and  $\text{Co}_3\text{O}_4$  as starting powders. The measured densities were typically  $3.29\ \text{g/cm}^3$  (71% of the theoretical density) and  $4.34\ \text{g/cm}^3$  (93 % of the theoretical density) in  $\text{Ca}_3\text{Co}_4\text{O}_9$  and  $\text{Ca}_{2.7}\text{Bi}_{0.3}\text{Co}_4\text{O}_9$  respectively. The growth mechanism in  $\text{Ca}_{2.7}\text{Bi}_{0.3}\text{Co}_4\text{O}_9$  was not very clearly understood however, the authors highlighted two important factors. Firstly, the presence of bismuth improved the diffusion and growth kinetics; it was found during experiments that bismuth-doped samples required a lower sintering temperature to prevent melting,  $1273\ \text{K}$  for  $\text{Ca}_{2.7}\text{Bi}_{0.3}\text{Co}_4\text{O}_9$  instead of  $1373\ \text{K}$  for  $\text{Ca}_3\text{Co}_4\text{O}_9$ . Therefore, it was concluded that Bi decreased the melting point in calcium cobaltite and may form a liquid phase promoting stacking and sliding of plate-like grains during high temperature sintering.

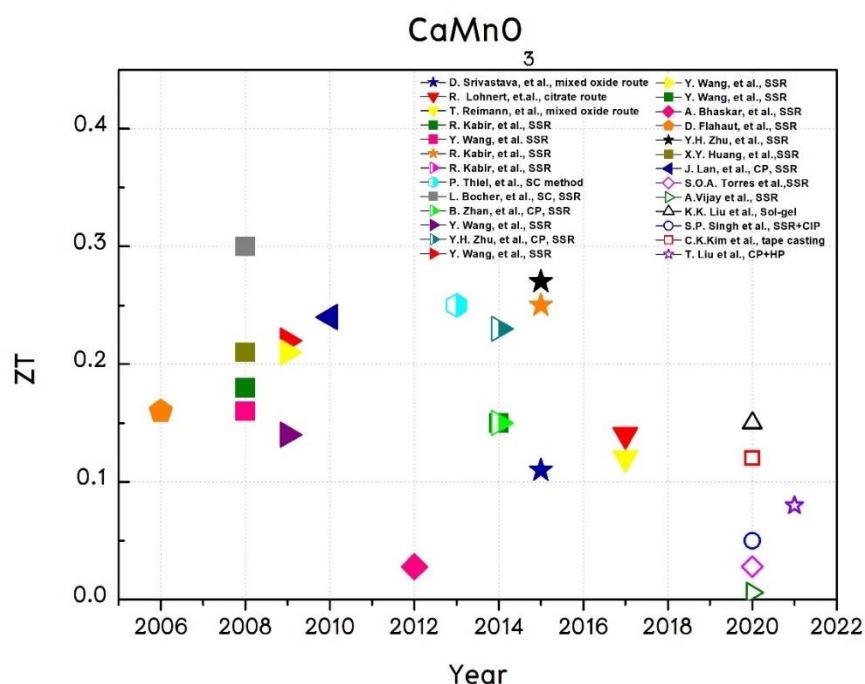
Comparison of the X-ray spectra of the two compositions showed higher intensity (00l) peaks for  $\text{Ca}_{2.7}\text{Bi}_{0.3}\text{Co}_4\text{O}_9$  sample, an indication of the presence of texturing. The degree of texturing in  $\text{Ca}_{2.7}\text{Bi}_{0.3}\text{Co}_4\text{O}_9$  was calculated based on Lotgering factor (Lotgering, 1959, pp. 113–123) and was found to be 86%. No texturing was observed for  $\text{Ca}_3\text{Co}_4\text{O}_9$ ; therefore, it was concluded that bismuth had a pronounced effect on the grain alignment of  $\text{Ca}_3\text{Co}_4\text{O}_9$ . SEM showed that in powder samples of both bismuth-doped and bismuth-free samples, the grains exhibited a plate-like shape, several microns in size with no significant difference in the size and morphology of the grains between two samples. However, in bulk samples, the bismuth-doped samples had a larger grain size and seemed to align homogeneously perpendicular to the direction of pressing compared to smaller and randomly orientated grains of the bismuth-free sample. The electrical conductivity and Seebeck coefficients were measured in both the a–b plane and along the c axis. It was found that the electrical conductivity was highly dependent on the lattice direction. Xu et al. reported the Bi, Na and (Bi–Na) substituted  $\text{Ca}_3\text{Co}_4\text{O}_9$  were studied thermoelectric properties (Xu, Funahashi, Shikano, Matsubara, & Zhou, 2002, pp. 3760–3762).  $\text{Ca}_3\text{Co}_4\text{O}_9$ ,  $\text{Ca}_{2.7}\text{Na}_{0.3}\text{Co}_4\text{O}_9$ ,  $\text{Ca}_{2.7}\text{Bi}_{0.3}\text{Co}_4\text{O}_9$ , and  $\text{Ca}_{2.4}\text{Bi}_{0.3}\text{Na}_{0.3}\text{Co}_4\text{O}_9$  were prepared using  $\text{CaCO}_3$ ,  $\text{Co}_3\text{O}_4$ ,  $\text{Bi}_2\text{O}_3$  and  $\text{Na}_2\text{CO}_3$  powders by the solid-state reaction then densified by hot pressing. The substitution of Na and Bi and double substitution enhanced the electrical conductivity values compared to pure  $\text{Ca}_3\text{Co}_4\text{O}_9$ . An increase in electrical conductivity values due to Na substitution was explained by an increase in carrier concentration (if other factors such as grain size and orientation were not considered). However, substitution of  $\text{Bi}^{3+}$  for  $\text{Ca}^{2+}$  would decrease hole concentration. The thermal conductivity of  $\text{Ca}_{2.7}\text{Bi}_{0.3}\text{Co}_4\text{O}_9$  was reported to be around  $2 \text{ Wm}^{-1}\text{K}^{-1}$  over the temperature range of 300–1000 K in comparison to  $1.8\text{--}1.7 \text{ Wm}^{-1}\text{K}^{-1}$  of  $\text{Ca}_{2.4}\text{Bi}_{0.3}\text{Na}_{0.3}\text{Co}_4\text{O}_9$ . The increase in the thermopower, electrical conductivity and reduction in the thermal conductivity led to a high  $ZT$  of 0.35 and 0.24 at 1000 K for compositions  $\text{Ca}_{2.4}\text{Bi}_{0.3}\text{Na}_{0.3}\text{Co}_4\text{O}_9$  and  $\text{Ca}_{2.7}\text{Bi}_{0.3}\text{Co}_4\text{O}_9$  respectively. Puri, N *et al.* reported highly pure and fully dense pellets prepared by solid-state ball mill and consolidated by hot-pressing method. They were



suggest fully dense and highly pure phase of samples with longer ball-milling time require less calcination time (Puri, *et al.*, 2018, pp. 6337–6342). Yin T. et al. (Yin, *et al.*, 2010, pp. 10061–10065) reported a novel technique to developed process nanocrystalline  $\text{Ca}_3\text{Co}_4\text{O}_9$  ceramics with a much enhanced thermoelectric properties synthesized first by sol-gel based electrospinning, and consolidated into bulk ceramics by spark plasma sintering. They found a much smaller grain size and improved texture are observed in the nanofiber-sintered ceramics, The thermoelectric properties of  $\text{Ca}_3\text{Co}_4\text{O}_9$  ceramics undoped has substantially reduced thermal conductivity, resulting in 55% enhancement in the thermoelectric figure of merit  $ZT$  that is estimated to be around 0.40 at 975 K.

To summarize, The  $\text{Ca}_3\text{Co}_4\text{O}_9$  consists with a misfit-layered structure with a rock salt-type  $\text{Ca}_2\text{CoO}_3$  subsystem and  $\text{CdI}_2$ -type hexagonal subsystem that makes inside the structure have a stacked. For this reason, the misfit-layered oxide can be described as  $[\text{Ca}_2\text{CoO}_3][\text{CoO}_2]_{(b1/b2)}$  with a  $b1$  to  $b2$  ratio of approximately 1.62, where  $b1$  to  $b2$  are two lattice parameter for the rock salt and  $\text{CoO}_2$  subsystems respectively The typical thermoelectric properties in the temperature range of 300–1000 K are: i. Seebeck coefficient is between  $80\text{--}180\ \mu\text{VK}^{-1}$ , ii. Electrical resistivity of  $5\text{--}50\ \text{m}\Omega\cdot\text{cm}$ ., iii. Thermal conductivity of  $0.75\text{--}2\ \text{Wm}^{-1}\ \text{K}^{-1}$ ., iv. Highest  $ZT$  of 0.3 has been reported as shown in Figure 2.10 shows the current of  $ZT$  of  $\text{Ca}_3\text{Co}_4\text{O}_9$  from 2000–2022.

N-Type; Calcium Manganese Oxide



**Figure 2.11** Shows the current of  $ZT$  of  $\text{CaMnO}_3$  from 2006–2022.

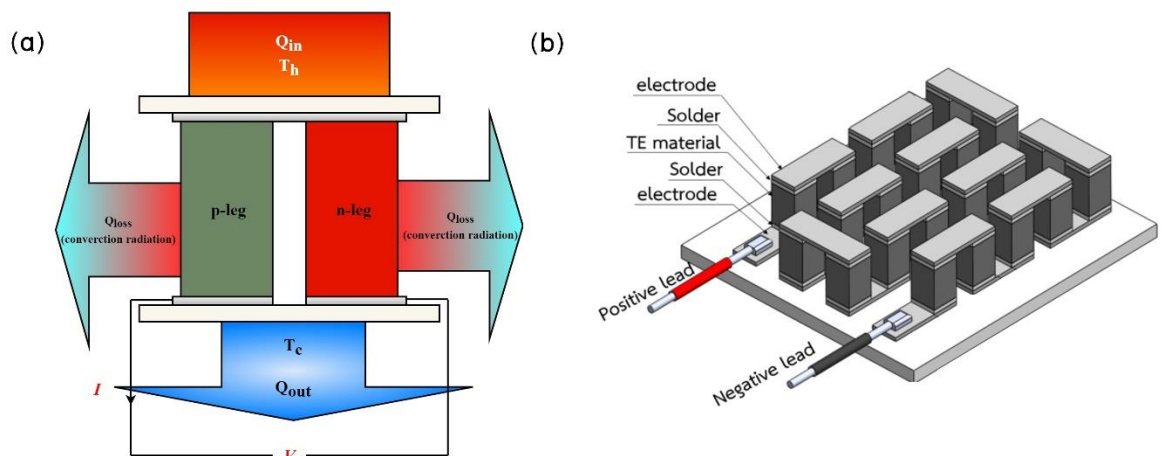
CaMnO<sub>3</sub> is another n-type material with a perovskite structure. Its space group has been identified as *Pnma* orthorhombic (Molinari, *et al.*, 2014, pp. 14109–14117). Two phase transition temperatures have been reported by Molinari *et al.* first, 1169 K from orthorhombic to tetragonal, and second, 1186 K from tetragonal to cubic. CaMnO<sub>3</sub> is a natural antiferromagnetic insulator at room temperature due to a lack of electrons in the valence band; due to this it has a comparatively low electrical conductivity of 10–100 Sm<sup>-1</sup> in temperature range of 300 to 1000 K. Thermal conductivity has also been found to be relatively high between 3.5–2.5 Wm<sup>-1</sup>K<sup>-1</sup> in the same temperature range. It has a large room temperature thermopower of about – 250 μVK<sup>-1</sup>. For CaMnO<sub>3</sub>, their thermoelectric properties are high Seebeck coefficient, at the high temperature figures of merit are high remain low due to their large resistivity but we can improved thermoelectric properties by dopant modification method (Wang, *et al.*, 2010, pp. 033708). Bocher *et al.* (Bocher, *et al.*, 2008, pp.

8077–8085) studied the effect of preparation route on microstructure and thermoelectric properties of Nb-doped  $\text{CaMnO}_3$ .  $\text{CaMn}_{1-x}\text{Nb}_x\text{O}_3$  ( $x \leq 0.08$ ) compositions were manufactured by solid-state route and a chemical method. Chemically prepared samples showed higher  $ZT$  values compared to samples prepared by the mixed-oxide route.  $ZT$  of 0.3 at 1000 K was achieved in chemically prepared  $\text{CaMn}_{0.98}\text{Nb}_{0.02}\text{O}_3$ . The main difference was found to be the thermal conductivity, where the solid-state sample had values of around  $2.8\text{--}1.5 \text{ Wm}^{-1} \text{ K}^{-1}$  over the temperature range of 300–1000 K in comparison to  $0.8 \text{ Wm}^{-1} \text{ K}^{-1}$  found in chemically prepared samples. Thiel et al. (Thiel, *et al.*, 2013, pp. 243707) also used a chemical route similar to Bocher et al. (Bocher, *et al.*, 2008, pp. 8077–8085) to manufacture and investigate  $\text{CaMn}_{1-x}\text{W}_x\text{O}_3$  ( $x \leq 0.05$ ). The thermal conductivity of W-doped samples was slightly lower compared to Nd-doped samples, but power factor was inferior.  $ZT$  was reported to be 0.15 at 1000 K and 0.25 at 1225 K. It was stated that increased  $ZT$  between 1200 and 1225 K was due to the creation of oxygen vacancies because of oxygen loss. Above 1225 K,  $ZT$  was found to be reducing; this was explained by a phase transition from orthorhombic to cubic. Koumoto, K et al. reported  $\text{CaMn}_{0.98}\text{Nb}_{0.02}\text{O}_3$  produced with a soft chemistry exhibit  $ZT$  values of 0.3 at 1073 K which are the one of highest values obtained for this material (Koumoto *et al.*, 2013, pp. 1–23). Figure 2.13 shows the current of  $ZT$  of  $\text{CaMnO}_3$  from 2006–2022.

## Thermoelectric generators

A thermoelectric generator (TEG), also called a Seebeck generator, is a solid-state device that converts heat flux (temperature differences) directly into electrical energy through a phenomenon called the Seebeck effect (a form of thermoelectric effect). Thermoelectric generators function like heat engines but are less bulky and have no moving parts (Adroja, *et al.*, 2015). However, TEGs are typically more expensive and less efficient. Thermoelectric power generators consist of three

major components: thermoelectric materials, thermoelectric modules and thermoelectric systems that interface connected electrically in series and thermally in parallel with the heat source (Jaziri, *et al.*, 2020, pp. 264–287) as shown in Fig. 2.12a. The thermoelectric materials consist of two type materials called p-type (with positive charge carriers) and n-type (with negative charge carriers). For end of p-type and n-type is contact with a heat source with temperature at hot-side and the other end is exposed to a heat sink at temperature cool-side. Under such a temperature gradient, the connected p- and n-type generate electrical voltage, current and power when connected to an external load. In practice, multiple pairs of p- and n-legs are connected to increase the total outputs (Figure 2.12b.)



**Figure 2.12** (a) Schematic principle of a TEG. (b) Schema of a typical TEG in practice.

## Energy conversion efficiency

The conversion efficiency of a thermoelectric device is determined by the Carnot efficiency and the figure of merit,  $ZT$ , of the thermoelectric material (TE). With increasing value of  $ZT$ , a higher maximum device energy conversion efficiency of the thermoelectric generator (TEG),  $\eta_{max}$ , was first derived based on a constant property model by Altenkirch in 1909, and its optimized formula has been commonly used since Ioffe reported the optimum condition for the maximum efficiency in 1957,

which can be expressed as: (Kim, *et al.*, 2015, pp. 8205–8210.)

$$\eta_{\max} = \frac{T_h - T_c}{T_h} \frac{\sqrt{1 + z\bar{T}_m} - 1}{\sqrt{1 + z\bar{T}_m + \frac{T_c}{T_h}}} \quad (21)$$

is expected.  $T_h$  is the hot side temperature and  $T_c$  is the cold side temperature,  $\frac{T_h - T_c}{T_h}$  is known as the Carnot efficiency, and  $\bar{T} = \frac{T_h + T_c}{2}$  is the mean temperature (Van Nong, *et al.*, 2015, pp. 20–27). The maximum efficiency of the thermoelectric generator is limited by Carnot factor,  $\Delta T / T_h$ , and the reduced efficiency that depends on  $ZT$ ,  $T_h$  and  $T_c$ . (Snyder, & Snyder, 2017, pp. 2280–2283).  $Z_{TEG}$  is the average figure of merit of the TEG:

$$Z_{TEG} = \frac{(\alpha_p - \alpha_n)}{KR} \quad (22)$$

where  $K, \alpha$ , and  $R$  : thermal conductance, thermopower and resistance of the TEG, respectively. Given that A is the total cross-sectional area of p- ( $A_p$ ) and n- ( $A_n$ ) legs the values of  $K, R$ , and  $\alpha$  are calculated as follows:

$$K = k_p \frac{A_p}{l_p} + k_n \frac{A_n}{l_n} \quad (23)$$

$$R = \rho_p \frac{l_p}{A_p} + \rho_n \frac{l_n}{A_n} \quad (24)$$

$$\alpha = |\alpha_p| + |\alpha_n| \quad (25)$$

The TE voltage  $V$ , the current  $I$  and the power  $P$  generated are:

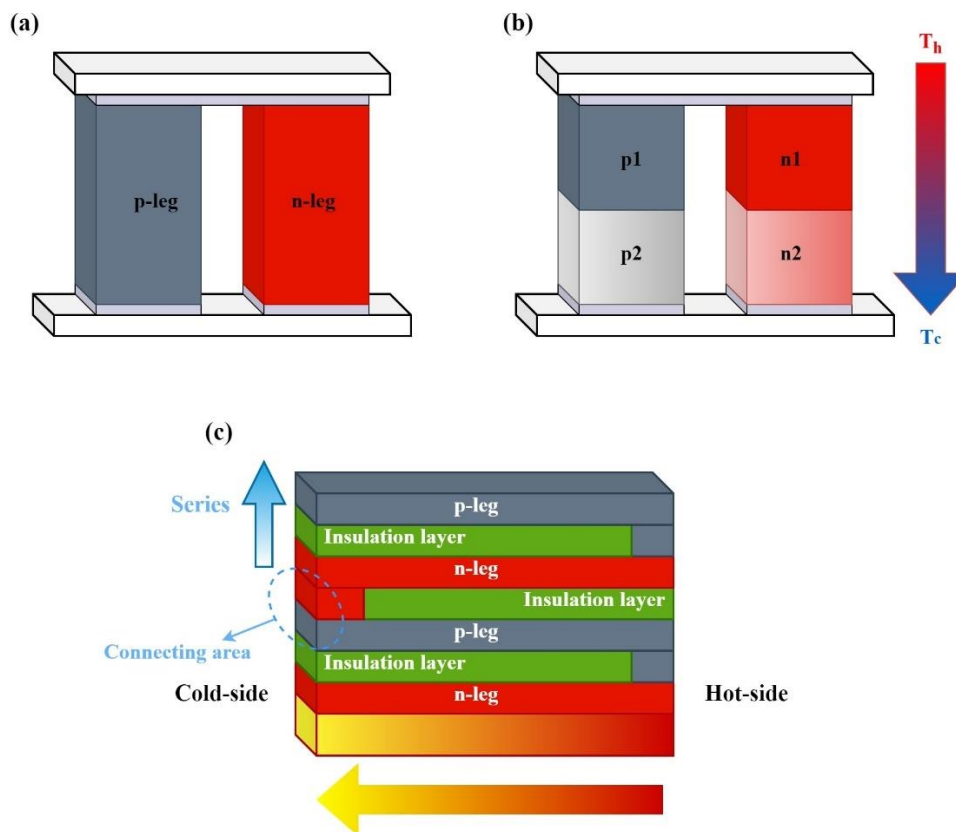
$$V = \alpha \Delta T \quad (26)$$

$$I = \frac{V}{R + R_{load}} \quad (27)$$

$$P = IV = \frac{(\alpha\Delta T)^2}{R + R_{load}} \quad (28)$$

### Multilayer or segmented bulk thermoelectric generators

The  $\pi$ -shape of traditional thermoelectric module commonly consists of n- and p-type of thermoelements with cylindrical shape. By the legs of thermoelements related to thermally in parallel from heat source and in series. The strength of the  $\pi$ -shape traditional thermoelectric modules is easily to conducts the heat unidirectionally and produces with the large of temperature difference in the direction of heat flux, which allows achieving best module performance. However, for the real situation for build up with applications of thermoelectric generators are limited because their relatively low output power. Thus, researcher was designed geometric structural modifications and other parameter optimization have been focused to optimize power output of thermoelectric generator. To realize the concept, two approaches have been developed with **segmented** or **multilayer**. A segmented leg requires that the compatibility between its constituent materials is matched to ensure the improvement of efficiency by segmentation. In the segmented structure, each n- and p-type is constructed from at least two different n- and p-thermoelements keep alternating. Materials in a leg are physically joined together with electrically and thermally in series. To build efficient segmented legs, the selection of the TE materials must be such that they are compatible with each other. The assumption of this model is that the system is thermally isolated i.e., no heat loss. Furthermore, influences of contact resistances are not included but can be integrated. The concept of these approaches is illustrated in Figure. 2.13 (a-c).

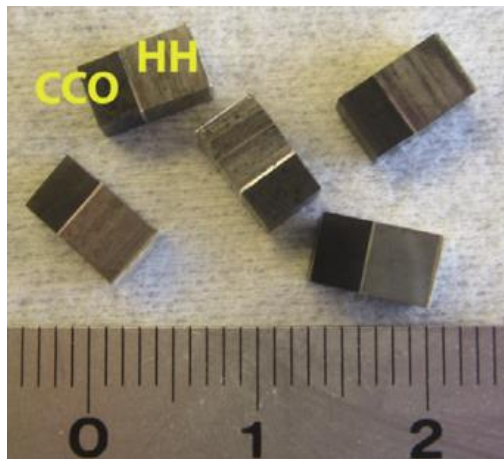


**Figure 2.13** Schematic principles of typical thermoelectric generator (a)  $\pi$ -shape traditional (b) segmented structure and (c) multilayer structure.

## Overview of oxide segmented TEGs and their relevant fabrication techniques

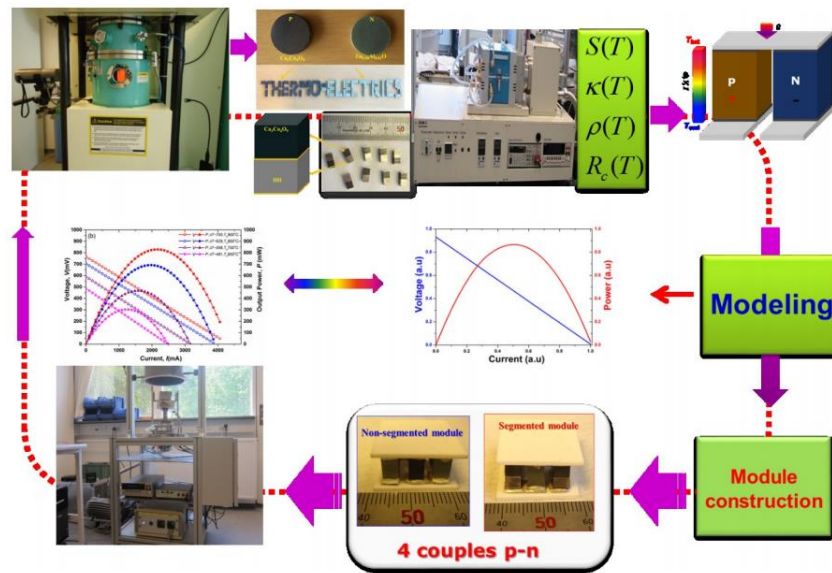
The result from thermoelectric researchers demonstrates an effective way to improve the efficiency of oxide TEG by segmentation of oxide materials with other high-performance non-oxide materials, thereby, extending the temperature range. For examples, Hung et al. reported about the segmented thermoelectric oxide-based module for high temperature. The segmented oxide-based module consists of half-Heusler  $\text{Ti}_{0.3}\text{Zr}_{0.35}\text{Hf}_{0.35}\text{CoSb}_{0.8}\text{Sn}_{0.2}$  and misfit-layered cobaltite  $\text{Ca}_3\text{Co}_4\text{O}_{9+\delta}$  as the p-leg and 2% Al-doped ZnO as the n-leg. For  $\text{Ca}_3\text{Co}_4\text{O}_{9+\delta}$  sample was synthesized by solid-state reaction followed by a spark plasma sintering process under a uniaxial

pressure of 50 MPa at 1123 K for 5 min under vacuum. While the half-Heusler  $\text{Ti}_{0.3}\text{Zr}_{0.35}\text{Hf}_{0.35}\text{CoSb}_{0.8}\text{Sn}_{0.2}$  was prepared by arc melting from the pure (99.999%) metals Ti, Zr, Hf, Co, Sb, and Sn and followed sintering by spark plasma sintering process at 1373 K for 20 min under a pressure of 50 MPa. For segmented thermoelectric fabrication, they use the Ag electrodes is put on top of two alumina substates by using the brazing/soldering joining method. The module was then placed in a graphite die and hot-pressed at 973 K under a pressure 20 MPa under Ar atmosphere as shown in Figure 2.14. The maximum output power of a 4-couple segmented module at  $\Delta T = 700$  K attains a value of approximately  $6.5 \text{ kW m}^{-2}$ , which is three times higher than that of the best reported non-segmented oxide module. Initial long-term stability tests of the module at the hot and the cold side temperatures of 1073 K and 444 K, respectively, showed a promising result with 4% degradation for 48 h operating in air (Hung *et al.*, 2015, pp. 1143–1151).



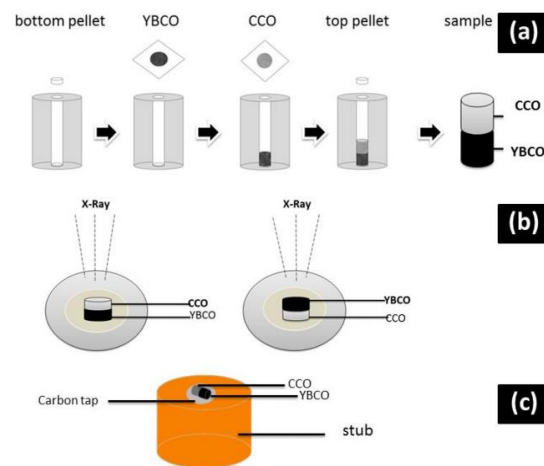
**Figure 2.14** Images of the fabricated segmented HH/CCO legs.





**Figure 2.15** Schematic of the whole thermoelectric module construction process from sintering and characterized materials to modelling, built up and test modules.

Wannasut *et al.* synthesized the  $\text{YBa}_2\text{Cu}_3\text{O}_{7-x}-\text{Ca}_3\text{Co}_4\text{O}_9$  segmented ceramic with high relative density of about 96% by hot pressing method at the high temperature. They were successful even though there may be a reaction and/or ionic diffusion at the interface, hot pressing seemed to be a suitable method to produce high-quality segmented thermoelectric ceramic for the YBCO-CCO system (Wannasut, Keawprak, Jaiban, & Watcharapasorn, 2018, pp. 012010).



**Figure 2.16** Schematic drawings of (a) steps of forming segmented YBCO–CCO ceramic, (b) XRD analysis of YBCO–side and CCO–side and (c) sample preparation for SEM/EDS analyses.

However, many combinations of p–n couples have been included in the oxide modules, the output power generation of oxide modules are still limited due to the low performance of oxide materials, in the mid–to low temperature range, and the large internal resistance. The highest conversion efficiency of oxide modules was estimated lower than 2%. One of the main reasons for this low result is the low performance in the low temperature range ( $< 750$  K). To overcome the limitation mentioned above, new strategies on improved material of  $ZT$  and a new concept in module design and fabrication are needed. Ideally, a combination of two types of materials in one device is expected to achieve higher efficiency by either segmenting. A segmented generator consists of two stage, where each stage is fabricated by a single p– and n–type thermoelectric materials in the horizontal direction. A high temperature material can be used for the hottest stage ( $>750$  K) and then a material with high electrical and thermal conductivity (Hung, *et al.*, 2015, pp. 1143–1151).

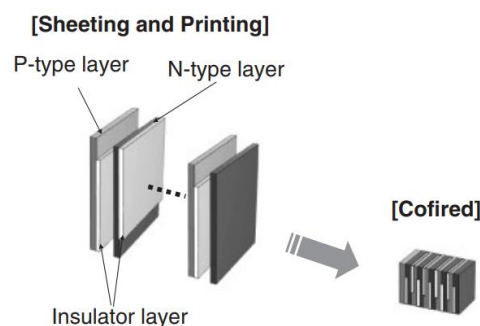
While, different to the traditional device, most of thin films will invents by multilayers are set layer by layer with the growth direction across the thin–film surface as Figure .2.14(c). Then multilayers three–layer NP junctions in series

available, with an insulating between every three-layer NP junctions. The purpose of segmented and multilayer structure enables a high integration of the thermoelements. It can enable the device to acquire with high output voltage by combining the NP thermoelectric modules in a small-scale range. Thus, it provides a possibility to simplify the manufacturing process. Töpfer, *et al.* were fabricated oxide multilayer thermoelectric generators (MLTEG) by using green tape p-type of  $\text{La}_2\text{CuO}_4$ , n-type of  $\text{Nd}_2\text{CuO}_4$  as shown in figure 2.17. The electrical contacts were using screen-printing of AgPd paste, cofired at 1273 K. The results show a TMLTEG based upon p-type lanthanum cuprite exhibits a power output of 7.8 mW at  $\Delta T = 200$  K in the low temperature range of 298–408 K.



**Figure 2.17** Schematic drawing of a multilayer thermoelectric (Töpfer, *et al.*, 2018, pp. 716–722).

Hayashi, S. F., *et al.* reported on developing novel thermoelectric multilayer cofired ceramics as shown in figure 2.20 and compared the results with simulation.



**Figure 2.18** Show Structure of the multilayer cofired ceramics (Hayashi, *et al.*, 2010, pp. 096505).

They were fabrication of the TE device elements,  $\text{La}_2\text{O}_3$ ,  $\text{SrCO}_3$ ,  $\text{CuO}$ ,  $\text{Nd}_2\text{O}_3$ , and  $\text{CeO}_2$  were used. The results show a maximum generated power of 0.0263 W was obtained at  $T \approx 360$  K, and the generated electric power was estimated to be 40 mW/cm<sup>2</sup>.

In 2018, Thomas, S et al. were reported synthesis a single-phase, multilayer samples of  $\text{Ca}_3\text{Co}_4\text{O}_9$  prepared by powder with the mixed-oxide route and different sintering routes: conventional sintering at 1193 K, alternative sintering at 1473 K and annealing at 1173 K, or hot pressing with 10 MPa at 1193 K. They were found that conventional sintering sample have exhibits a low density only. The electrical conductivity of multilayer laminates conventional sintered at 1193 K show  $35 \text{ Sm}^{-1}$  at 373 K, thermal conductivity is very low  $6 \text{ Wm}^{-1} \text{ K}^{-1}$  at 373 K but a sample has a low density 55% and large porosity (Schulz, *et al.*, 2018, pp. 1600–1607). Multilayer of  $\text{Ca}_3\text{Co}_4\text{O}_9$  thick thermoelectric materials were fabricated by hot-pressing method reported by Driss Kenfaui et al. The results show a bulk density of multilayer like a single-layer samples, but remarkable texture strength reinforcement. The resulting figure-of-merit  $ZT$  is then noticeably anisotropic (Kenfaui *et al.*, 2012, pp. 2405–2414). D. Kenfaui *et al.* reports the  $\text{Ca}_3\text{Co}_4\text{O}_9$  (349) thermoelectric ceramics were synthesis by using hot pressing (HP) process under various stress levels up to 30 MPa. The mechanical properties were shown to improve well with the applied stress,  $\sigma$ , and anisotropy of elastic modulus, and of the hardness occur. The resistivity anisotropy of the sample prepared at 30 MPa has increases drastically with  $\sigma$  and reaches 64 at 300 K.

## References

- Angrnanon, A. (2020). Effect of Hot-Defection on Thermoelectric Properties of  $\text{Ca}_3\text{Co}_4\text{O}_9$  Synthesized By Hot Pressing. *Journal of Materials Science and Applied Energy*, 9(1), 469–472.
- Adroja, M. N., Mehta, S. B., & Shah, M. P. (2015). Review of thermoelectricity to improve energy quality. *International Journal of Emerging Technologies and Innovative Research JETIR*, 2.
- Baranowski, L. L., Jeffrey Snyder, G., & Toberer, E. S. (2013). Effective thermal conductivity in thermoelectric materials. *Journal of applied physics*, 113(20), 204904.
- Bhansali, S. (2017). Thermoelectric properties of oxides and related materials.
- Bhaskar, A., Liu, C. J., Yuan, J. J., & Chang, C. L. (2013). Thermoelectric properties of n-type  $\text{Ca}_{1-x}\text{Bi}_x\text{Mn}_{1-y}\text{Si}_y\text{O}_3$ - $\delta$  ( $x=y=0.00, 0.02, 0.03, 0.04$ , and  $0.05$ ) system. *Journal of alloys and compounds*, 552, 236–239.
- Bocher, L., Aguirre, M., Logvinovich, D., Shkabko, A., Robert, R., Trottmann, M., & Weidenkaff, A. (2008).  $\text{CaMn}_{1-x}\text{Nb}_x\text{O}_3$  ( $x \leq 0.08$ ) Perovskite-Type Phases As Promising New High-Temperature n-Type Thermoelectric Materials. *Inorganic Chemistry*, 47(18), 8077–8085.
- Böttner, H., Chen, G., & Venkatasubramanian, R. (2006). Aspects of thin-film superlattice thermoelectric materials, devices, and applications. *MRS bulletin*, 31(3), 211–217.
- Büttner, G. (2017). Misfit-layered cobalt oxides for thermoelectric energy conversion.
- Chen, G. (2001). Phonon transport in low dimensional. *Semicond Semimetals*, 71, 203.
- Delorme, F., Ovono, D. O., Marudhachalam, P., Martin, C. F., & Fraboulet, O. (2012). Effect of precursors size on the thermoelectric properties of  $\text{Ca}_3\text{Co}_4\text{O}_9$  ceramics. *Materials Research Bulletin*, 47(5), 1169–1175.

- Dresselhaus, M. S., Chen, G., Tang, M. Y., Yang, R., Lee, H., Wang, D., . . . Gogna, P. (2007). New directions for low-dimensional thermoelectric materials. *Advanced Materials*, 19(8), 1043–1053.
- Enescu, D. (2019). Thermoelectric energy harvesting: basic principles and applications. *Green energy advances*, 1.
- Fergus, J. W. (2012). Oxide materials for high temperature thermoelectric energy conversion. *Journal of the European Ceramic Society*, 32(3), 525–540.
- Granitzer, P., & Rumpf, K. (Eds.). (2014). *Nanostructured semiconductors: from basic research to applications*. CRC Press.
- Grebille, D., Muguerra, H., Pérez, O., Guilmeau, E., Rousselière, H., & Funahashi, R. (2007). Superspace crystal symmetry of thermoelectric misfit cobalt oxides and predicted structural models. *Acta Crystallographica Section B*, 63(3), 373–383.
- Gunes, M., & Ozenbas, M. (2015). Effect of grain size and porosity on phonon scattering enhancement of  $\text{Ca}_3\text{Co}_4\text{O}_9$ . *Journal of Alloys and Compounds*, 626, 360–367.
- Harman, T., Taylor, P., Walsh, M., & LaForge, B. (2002). Quantum dot superlattice thermoelectric materials and devices. *science*, 297(5590), 2229–2232.
- Hao, H., He, Q., Chen, C., Sun, H., & Hu, X. (2009). TEXTURED STRUCTURE AND ANISOTROPIC THERMOELECTRIC PROPERTIES OF  $\text{Ca}_{2.7}\text{Bi}_{0.3}\text{Co}_4\text{O}_9$  OXIDE PREPARED BY CONVENTIONAL SOLID-STATE REACTION. *International Journal of Modern Physics B*, 23(01), 87–95.
- Hayashi, S. F., Nakamura, T., Kageyama, K., & Takagi, H. (2010). Monolithic thermoelectric devices prepared with multilayer cofired ceramics technology. *Japanese Journal of Applied Physics*, 49(9R), 096505.
- Hilaal Alama, S. (2012). A review on the enhancement of figure of merit from bulk to Nano thermoelectric materials. 2, 190–212.

- Hung, L. T., Van Nong, N., Han, L., Bjørk, R., Ngan, P. H., Holgate, T. C., ... & Pryds, N. (2015). Segmented thermoelectric oxide-based module for high-temperature waste heat harvesting. *Energy Technology*, 3(11), 1143–1151.
- Ioffe, A. (1957). *Semiconductor Thermoelements and Thermoelectric Cooling* (London: Infosearch): Ltd.
- Lotgering, F. K. (1959). Topotactical reactions with ferrimagnetic oxides having hexagonal crystal structures—I. *Journal of Inorganic and Nuclear Chemistry*, 9(2), 113–123.
- Jaziri, N., Boughamoura, A., Müller, J., Mezghani, B., Tounsi, F., & Ismail, M. (2020). A comprehensive review of Thermoelectric Generators: Technologies and common applications. *Energy Reports*, 6, 264–287.
- Kenfaui, D., Lenoir, B., Chateigner, D., Ouladdiaf, B., Gomina, M., & Noudem, J. G. (2012). Development of multilayer textured  $\text{Ca}_3\text{Co}_4\text{O}_9$  materials for thermoelectric generators: Influence of the anisotropy on the transport properties. *Journal of the European Ceramic Society*, 32(10), 2405–2414.
- Kenfaui, D., Chateigner, D., Gomina, M., & Noudem, J. G. (2011). Anisotropy of the Mechanical and Thermoelectric Properties of Hot-Pressed Single-Layer and Multilayer Thick  $\text{Ca}_3\text{Co}_4\text{O}_9$  Ceramics. *International Journal of Applied Ceramic Technology*, 8(1), 214–226.
- Kim, H. S., Liu, W., Chen, G., Chu, C. W., & Ren, Z. (2015). Relationship between thermoelectric figure of merit and energy conversion efficiency. *Proceedings of the National Academy of Sciences*, 112(27), 8205–8210.
- Koumoto, K., Funahashi, R., Guilmeau, E., Miyazaki, Y., Weidenkaff, A., Wang, Y., & Wan, C. (2013). Thermoelectric ceramics for energy harvesting. *Journal of the American Ceramic Society*, 96(1), 1–23.
- Koumoto, K., Funahashi, R., Guilmeau, E., Miyazaki, Y., Weidenkaff, A., Wang, Y., & Wan, C. (2013). Thermoelectric ceramics for energy harvesting. *Journal of the American Ceramic Society*, 96(1), 1–23.

- Li, S., Funahashi, R., Matsubara, I., Ueno, K., Sodeoka, S., & Yamada, H. (2000). Synthesis and Thermoelectric Properties of the New Oxide Materials  $\text{Ca}_{3-x}\text{Bi}_x\text{Co}_4\text{O}_{9+\delta}$  ( $0.0 < x < 0.75$ ). *Chemistry of Materials*, 12(8), 2424–2427.
- Lotgering, F. (1959). Topotactical reactions with ferrimagnetic oxides having hexagonal crystal structures—I. *Journal of Inorganic and Nuclear Chemistry*, 9(2), 113–123.
- Lowrie, W., & Fichtner, A. (2020). *Fundamentals of geophysics*. Cambridge university press.
- Masset, A. C., Michel, C., Maignan, A., Hervieu, M., Toulemonde, O., Studer, F., & Hejtmanek, J. (2000). Misfit-layered cobaltite with an anisotropic giant magnetoresistance:  $\text{Ca}_3\text{Co}_4\text{O}_9$ . *Physical Review B*, 62(1), 166.
- Minnich, A., Dresselhaus, M., Ren, Z., & Chen, G. (2009). Bulk nanostructured thermoelectric materials: current research and future prospects. *Energy & Environmental Science*, 2(5), 466–479.
- Miyazaki, Y., Onoda, M., Oku, T., Kikuchi, M., Ishii, Y., Ono, Y., . . . Kajitani, T. (2002). Modulated structure of the thermoelectric compound  $[\text{Ca}_{2-x}\text{CoO}_3]_{0.62}\text{CoO}_2$ . *Journal of the Physical Society of Japan*, 71(2), 491–497.
- Molinari, M., Tompsett, D. A., Parker, S. C., Azough, F., & Freer, R. (2014). Structural, electronic and thermoelectric behaviour of  $\text{CaMnO}_3$  and  $\text{CaMnO}_{3-\delta}$ . *Journal of Materials Chemistry A*, 2(34), 14109–14117.
- öer K.W., Pohl U.W. (2017) Carrier Transport Induced and Controlled by Defects. In: Semiconductor Physics. Springer, Cham. [https://doi.org/10.1007/978-3-319-06540-3\\_28-3](https://doi.org/10.1007/978-3-319-06540-3_28-3).
- Ohtaki, M. (2010). Oxide thermoelectric materials for heat-to-electricity direct energy conversion. *Novel Carbon Resour. Sci. Newsl*, 3.
- Puri, N., Tandon, R. P., & Mahapatro, A. K. (2018). Fully dense hot pressed calcium cobalt oxide ceramics. *Ceramics International*, 44(6), 6337–6342.
- Rowe, D. M. (2005). *Thermoelectrics handbook: macro to nano*: CRC press.



- Saleemi, M. (2014). *Nano-Engineered Thermoelectric Materials for Waste Heat Recovery*. KTH Royal Institute of Technology.
- Schulz, T., Reimann, T., Bochmann, A., Vogel, A., Capraro, B., Mieller, B., ... & Töpfer, J. (2018). Sintering behavior, microstructure and thermoelectric properties of calcium cobaltite thick films for transversal thermoelectric multilayer generators. *Journal of the European Ceramic Society*, 38(4), 1600–1607.
- Seetawan, T., Amornkitbamrung, V., Burinprakhon, T., Maensiri, S., Tongbai, P., Kurosaki, K., ... & Yamanaka, S. (2006). Effect of sintering temperature on the thermoelectric properties of  $\text{Na}_x\text{Co}_2\text{O}_4$ . *Journal of alloys and compounds*, 416(1–2), 291–295.
- Seymour J, Physical Electronics, Pitman, 1972, pp 53–54 34.
- Shakouri, A., & Zebarjadi, M. (2009). Nanoengineered materials for thermoelectric energy conversion *Thermal Nanosystems and Nanomaterials* (pp. 225–299): Springer.
- Smith, D. (1972). Physical Electronics. *Students' Quarterly Journal*, 42(169), 78.
- Snyder, G. J., & Snyder, A. H. (2017). Figure of merit ZT of a thermoelectric device defined from materials properties. *Energy & Environmental Science*, 10(11), 2280–2283.
- Somkhunthot, W., Burinprakhon, T., Seetawan, T., & Amornkitbamrung, V. (2007). Bipolar pulsed-DC power supply for magnetron sputtering and thin films synthesis. *Elektrika Journal of Electrical Engineering*, 9(2), 20–26.
- Sootsman, J. R., Chung, D. Y., & Kanatzidis, M. G. (2009). New and old concepts in thermoelectric materials. *Angewandte Chemie – International Edition*, 48(46), 8616–8639. <https://doi.org/10.1002/anie.200900598>
- Spies, P., Pollak, M., & Mateu, L. (Eds.). (2015). *Handbook of energy harvesting power supplies and applications*. CRC Press.

- Töpfer, J., Reimann, T., Schulz, T., Bochmann, A., Capraro, B., Barth, S., . . . Teichert, S. (2018). Oxide multilayer thermoelectric generators. *International Journal of Applied Ceramic Technology*, 15(3), 716–722.
- Thiel, P., Eilertsen, J., Populoh, S., Saucke, G., Döbeli, M., Shkabko, A., . . . Weidenkaff, A. (2013). Influence of tungsten substitution and oxygen deficiency on the thermoelectric properties of  $\text{CaMnO}_{3-\delta}$ . *Journal of applied physics*, 114(24), 243707.
- Trigo, M., Bruchhausen, A., Fainstein, A., Jusserand, B., & Thierry-Mieg, V. (2002). Confinement of acoustical vibrations in a semiconductor planar phonon cavity. *Physical review letters*, 89(22), 227402.
- Van Nong, N., Snyder, G. J., Viet, M. H., Balke, B., Han, L., Stamate, E., ... & Pryds, N. (2015). High performance p-type segmented leg of misfit-layered cobaltite and half-Heusler alloy. *Energy Conversion and Management*, 99, 20–27.
- Vineis, C. J., Shakouri, A., Majumdar, A., & Kanatzidis, M. G. (2010). Nanostructured thermoelectrics: big efficiency gains from small features. *Advanced Materials*, 22(36), 3970–3980.
- Wang, Y., Sui, Y., Wang, X., Su, W., & Liu, X. (2010). Enhanced high temperature thermoelectric characteristics of transition metals doped  $\text{Ca}_{3}\text{Co}_{4}\text{O}_{9+\delta}$  by cold high-pressure fabrication. *Journal of applied physics*, 107(3), 033708.
- Wannasut, P., Keawprak, N., Jaiban, P., & Watcharapasorn, A. (2018). Preparation and Physical Properties of Segmented Thermoelectric  $\text{YBa}_2\text{Cu}_3\text{O}_{7-x}-\text{Ca}_3\text{Co}_4\text{O}_9$  Ceramics. In *IOP Conference Series: Materials Science and Engineering* (Vol. 303, No. 1, p. 012010). IOP Publishing.
- Xu, G., Funahashi, R., Shikano, M., Matsubara, I., & Zhou, Y. (2002). Thermoelectric properties of the Bi- and Na-substituted  $\text{Ca}_{3}\text{Co}_{4}\text{O}_9$  system. *Applied Physics Letters*, 80(20), 3760–3762.

- Yamauchi, H., Sakai, K., Nagai, T., Matsui, Y., & Karppinen, M. (2006). Parent of Misfit-Layered Cobalt Oxides:  $[\text{Sr}_{2/3}\text{CoO}_2]$ . *Chemistry of Materials*, 18(1), 155–158.
- Yin, T., Liu, D., Ou, Y., Ma, F., Xie, S., Li, J.-F., & Li, J. (2010). Nanocrystalline thermoelectric  $\text{Ca}_{0.3}\text{Co}_{0.7}\text{O}_{1.9}$  ceramics by sol-gel based electrospinning and spark plasma sintering. *The Journal of Physical Chemistry C*, 114(21), 10061–10065.
- Yu. A. Skripnik, A. I. Khimicheva. Methods and devices for measuring the Peltier coefficient of an inhomogeneous electric circuit. *Measurement Techniques* July 1997, Volume 40, Issue 7, pp 673–677



## CHAPTER 3

### METHODOLOGY

In this dissertation, several experimental methods are applied for the preparation and characterization of thermoelectric materials and converters. The methods can be grouped in four categories: (i) the synthesis of powders and preparation of sintered p-type  $\text{Ca}_3\text{Co}_4\text{O}_9$ , n-type  $\text{CaMnO}_3$ , (ii) the characterization of the sample morphology, structure, and phase composition, and thermoelectric properties (iii) the fabrication and characterization the nano oxide multilayers/segmented thermoelectric generator, and (iv) the test performance of thermoelectric converters the nano oxide multilayer p-type  $\text{Ca}_3\text{Co}_4\text{O}_9$ , n-type  $\text{CaMnO}_3$ . Those methods, and their application in this work, are introduced in this chapter.

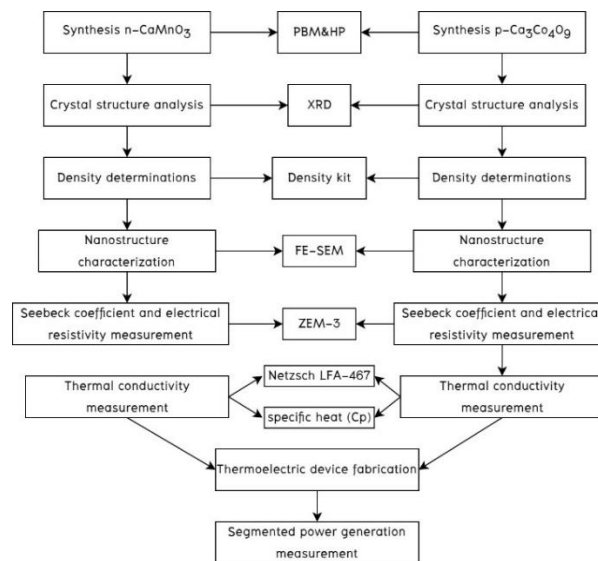


Figure 3.1 The schematic diagram of methodology.

## SYNTHESIS AND PREPARATION THERMOELECTRIC MATERIALS

### Synthesis n-CaMnO<sub>3</sub> and p-Ca<sub>3</sub>Co<sub>4</sub>O<sub>9</sub> powder thermoelectric materials

The solid-state reaction (SSR) method is most widely used for synthesis compounds because easily mixing solid powder precursors follow stoichiometric ratios. The n-CaMnO<sub>3</sub> and p-Ca<sub>3</sub>Co<sub>4</sub>O<sub>9</sub> materials were synthesized by ball-mill and hot-pressing methods. The chemical powder and equipment used in this process are shown in Table 3.1 and Table 3.2, respectively.

**Table 3.1:** List of chemicals used for solid-state reaction methods, their formula, supplier, and purity.

Chemical	Formula	Supplier	Purity	d/quantity
Calcium carbonate	CaCO <sub>3</sub>	US Research Nanomaterials, Inc.	98%	50 nm
Cobalt oxide	Co <sub>2</sub> O <sub>3</sub>	US Research Nanomaterials, Inc.	99.7%	50 nm
Manganese oxide	MnO <sub>2</sub>	US Research Nanomaterials, Inc.	98%	50 nm
Silver-sheet	Ag	Hurricane Magnets & Materials Engineering	99.99%	0.1×100×100 mm
Ethanol	CH <sub>2</sub> CH <sub>3</sub> OH	QRëC	99.99%	

**Table 3.2:** List of equipment used for synthesis of powder, preparation of bulk, characterization, and measurement of thermoelectric properties together with their model and area of application

Equipment	Model	Application
Planetary ball mill	PM 400	Mixing and milling powders
Ultrasonic cleaner	GT Sonic VGT-1730QTD	Cleaning of materials
Hot plate & stirrer	C-MAG HS 7-IKA Group Germany	Drying the reduce the moisture in the materials and drying the Ag paste for makes electrodes
Analytical balances	BGB-224, ZEPPER	To measure weight or mass of raw materials
Furnace	XDEM-1700AF	For calcination and firing the Ag paste
Hot press furnace	OTF-1200x-VHP-4	Pressing and sintering the dried powder into the pellets
Saw low speed	BUEHLER Isomet	Cutting the balk materials
X-ray diffractometer (XRD)	LabX SHIMADZU-6100	Crystal structure analysis

**Table 3.2** (continues)

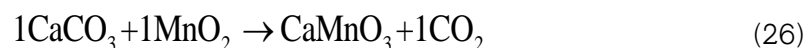
<b>Equipment</b>	<b>Model</b>	<b>Application</b>
Seebeck coefficient/electrical resistance measuring system (ZEM-3)	ULVAC-RIKO, Japan	Measured Seebeck coefficient, electrical resistance, and power factor of materials
Field emission scanning electron microscopy (FE-SEM)	JSM-7610F, JEOL, Japan	Microstructure characterization and chemical composition
Thermal diffusivity	Netzsch LFA-467, Germany	For calculated the thermal conductivity with the density of materials and specific heat capacity
Density kit	MS-DNY-54	Measure density of materials



### Preparation n-CaMnO<sub>3</sub> thermoelectric material

The n-CaMnO<sub>3</sub> was synthesized by ball-milling and hot-press method as follow by:

1. The calcium carbonate nano powder (CaCO<sub>3</sub>, US Research Nanomaterials, Inc., purity 98%, 50 nm) and manganese dioxide nano powder (MnO<sub>2</sub>, US Research Nanomaterials, Inc., purity 98%, 50nm) were used for raw materials and weight at an atomic ratio as shown in equation.26, and Table 3.3

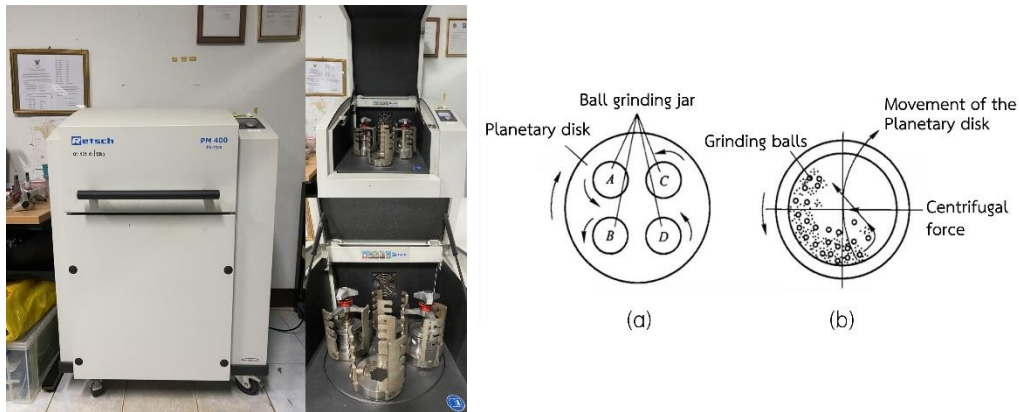


**Table 3.3** Materials balance of n-CaMnO<sub>3</sub> for 10 g.

Materials	Balance (g)	
CaMnO <sub>3</sub>	CaCO <sub>3</sub> =6.998393	MnO <sub>2</sub> =6.078871
	CO <sub>2</sub> =3.077264	

2. The raw materials were mixed with planetary ball mill (PBM) (Retsch™ PM 400 Model Planetary Ball Mill) as shown in Figure. 3.2. Planetary Ball Mills are used wherever the highest degree of fineness is required. Apart from the classical mixing and size reduction processes, the mills also meet all the technical requirements for colloidal grinding and have the energy input necessary for mechanical alloying processes. The extremely high centrifugal forces of planetary ball mills result in very high pulverization energy and therefore short grinding times. While the raw powder materials of n-CaMnO<sub>3</sub> was mixed in the agate containers with an agate ball in size of diameter 10 mm. Starting materials were used, giving balls to powder weight ratios of 10 : 5. Planetary ball mill was performed at speed 350 rpm with a rate of interval 10

minute in air. To control the particle size of  $n\text{-CaMnO}_3$  powder was set up for 8 h for decreased particle size as much as possible approximately.



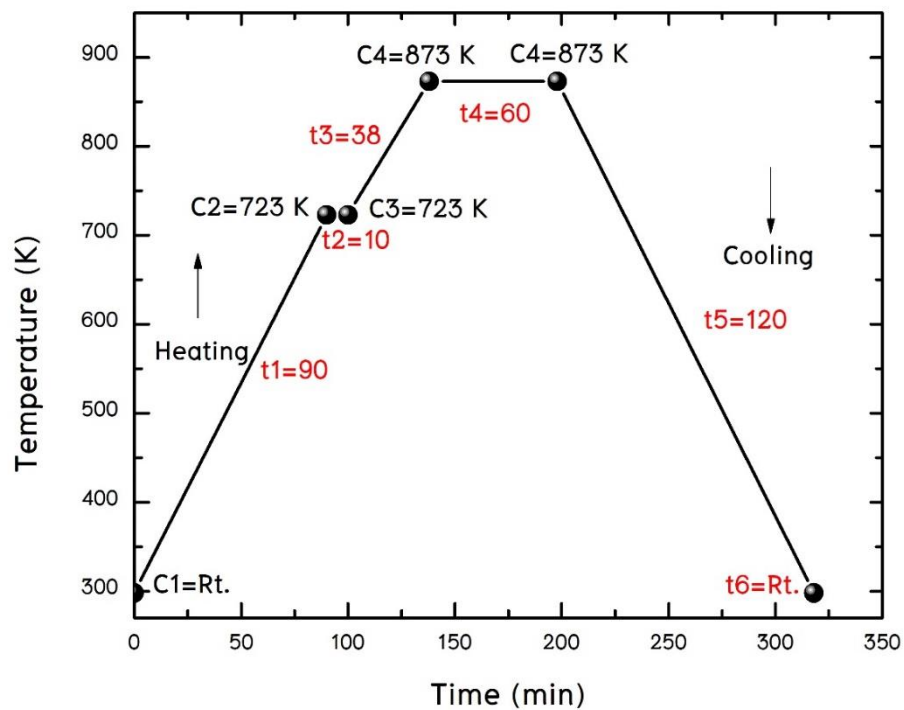
**Figure 3.2** Planetary ball milling apparatus of Retsch, PM-400 at Sakon Nakhon Rajabhat University and working principle of planetary ball mill (a) overall layout of planetary disk (b) horizontal section of grinding jar.

(<https://www.micronanotools.com/products/planetary-ball-mill-4x100ml-two-year-warranty-vacuum-and-inert-gas-grinding-compatible>)

3. For study was applied to the starting mixtures as well as to of  $n\text{-CaMnO}_3$  powder was calcined in oxygen atmosphere with temperature at 1123 K for 10 h for increasing the oxygen ratio in structure and reduced the secondary phases. After calcination of  $n\text{-CaMnO}_3$  was grinding and sieves for prepare sintering process by hot press method. These PVA solutions were made from PVA powder. Distilled water (>10 ml) was heated to approximately  $90^\circ\text{C}$ , and then PVA powder was added to the hot water and stirred with a magnetic stirring device. The mixture was heated and stirred for 30 min until the solution became clear.

4. For sintering method, the graphite die was set up in the hot press machine of  $n\text{-CaMnO}_3$  with temperature profile as shown in Figure. 3.3. The powders of  $n\text{-CaMnO}_3$  were pressed into pellets (thickness, 2 mm; diameter, 10 mm) by hot

pressing (OTF-1200x-VHP-4) under a pressure of 30 MPa at 873 K for 1 h in argon atmosphere.



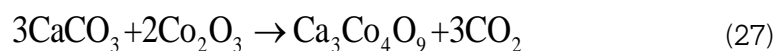
**Figure 3.3** The temperature profile for hot pressing of  $\text{CaMnO}_3$

5. The obtained circular pellets of  $n\text{-CaMnO}_3$  from hot press were cut in size of  $10 \times 10 \times 1 \text{ mm}^3$  for XRD and ZEM-3,  $3 \times 3 \times 15 \text{ mm}^3$  for thermoelectric properties measurement and  $3.5 \times 3.5 \times 5 \text{ mm}^3$  for segmented thermoelectric device fabrication.

### Preparation of p-Ca<sub>3</sub>Co<sub>4</sub>O<sub>9</sub> bulk thermoelectric materials

The p-Ca<sub>3</sub>Co<sub>4</sub>O<sub>9</sub> was synthesized by ball-milling and hot-press method as follow by:

1. The calcium carbonate nano powder (CaCO<sub>3</sub>, US Research Nanomaterials, Inc., purity 98%, 50 nm) and cobalt oxide nano powder (Co<sub>2</sub>O<sub>3</sub>, US Research Nanomaterials, Inc., purity 99.7%, 50nm) were used for raw materials and weight at an atomic ratio as shown in equation. 27 and Table 3.4.



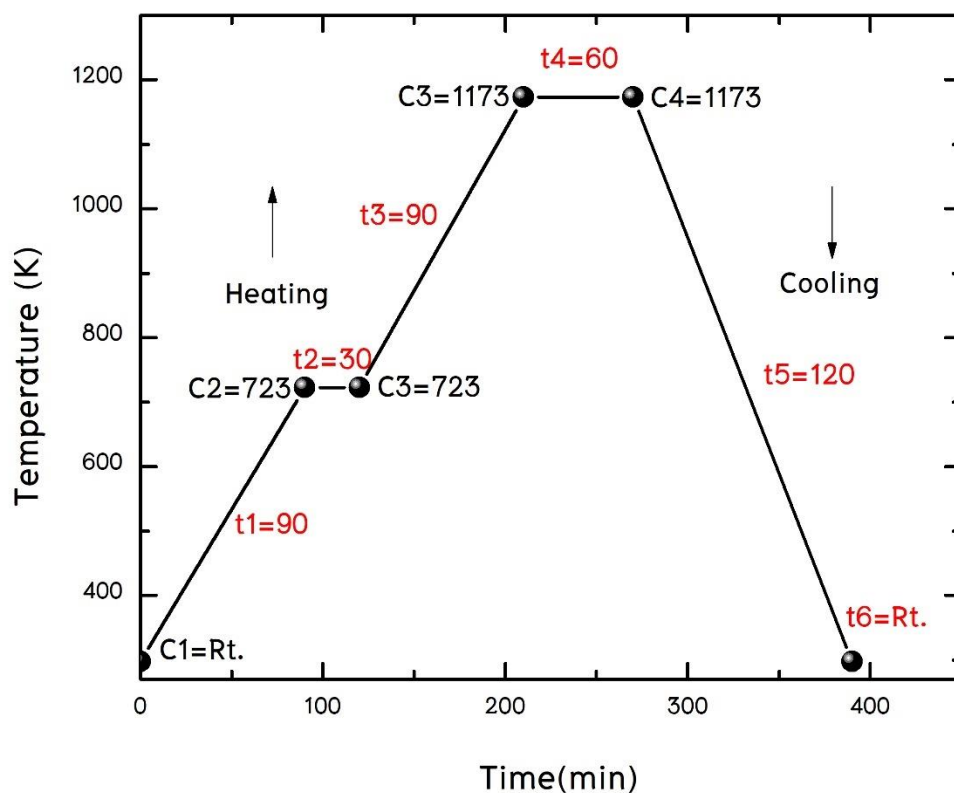
**Table 3.4:** Materials balance of p-Ca<sub>3</sub>Co<sub>4</sub>O<sub>9</sub> for 10 g.

Materials	Balance (g)	
Ca <sub>3</sub> Co <sub>4</sub> O <sub>9</sub>	CaCO <sub>3</sub> =6.005676	Co <sub>2</sub> O <sub>3</sub> =6.63508
	CO <sub>2</sub> =2.640757	

2. The raw materials were mixed with planetary ball mill (PBM) (Retsch™ PM 400 Model Planetary Ball Mill). While the raw powder materials of p-Ca<sub>3</sub>Co<sub>4</sub>O<sub>9</sub> was mixed in the agate containers with agate ball in size of diameter 10 mm. Starting materials were used, giving balls to powder weight ratios of 10 : 5. Planetary ball mill was performed at speed 350 rpm with a rate of interval 10 minute in air. To control the particle size of p-Ca<sub>3</sub>Co<sub>4</sub>O<sub>9</sub> powder was set up for 8 h for decreased particle size as much as possible approximately.

3. For study was applied to the starting mixtures as well as to of  $p\text{-Ca}_3\text{Co}_4\text{O}_9$  powder was calcined on ambient temperature at 1173 K for 10 h. After calcination of  $p\text{-Ca}_3\text{Co}_4\text{O}_9$  powder was grinding and sieves for prepare sintering process by hot press method.

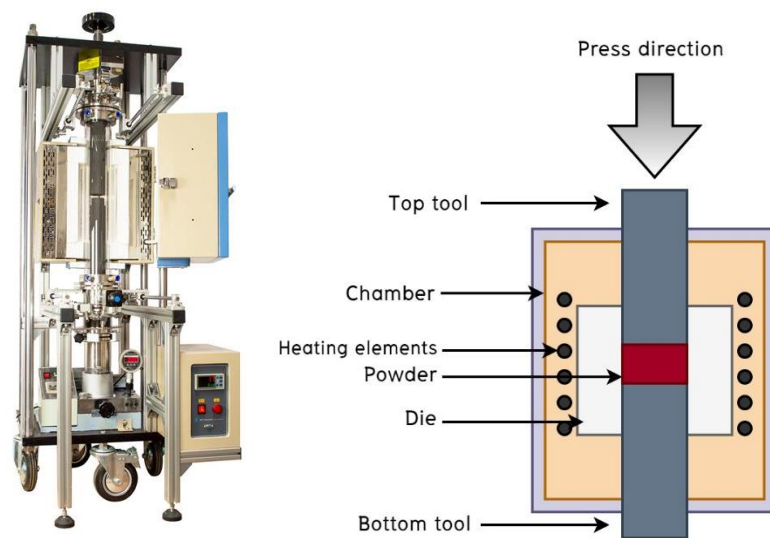
4. The graphite die was set up in the hot press machine of  $p\text{-Ca}_3\text{Co}_4\text{O}_9$  with temperature profile as shown in Figure. 3.4. The powders of  $p\text{-Ca}_3\text{Co}_4\text{O}_9$  were pressed into pellets (thickness, 2 mm; diameter, 10 mm) by hot pressing (OTF-1200x-VHP-4) under a pressure of 20 MPa at 1173 K for 1 h in argon atmosphere.



**Figure 3.4** The temperature profile for hot pressing of  $\text{Ca}_3\text{Co}_4\text{O}_9$

5. The obtained circular pellets of  $p\text{-Ca}_3\text{Co}_4\text{O}_9$  from hot press were cut in size of  $10\times 10\times 1\text{ mm}^3$  for XRD and ZEM-3,  $3\times 3\times 15\text{ mm}^3$  for thermoelectric properties measurement and  $3.5\times 3.5\times 5\text{ mm}^3$  for segmented thermoelectric device fabrication.

Hot pressing is a high-pressure, low-strain-rate powder metallurgy process for forming of a powder or powder compact at a temperature high enough to induce sintering and creep processes. This is achieved by the simultaneous application of heat and pressure. Hot pressing is mainly used to fabricate hard and brittle materials. The loose powder or the pre-compacted part is in most of the cases filled to a graphite mold that allows induction or resistance heating up to temperatures of typically  $1,000\text{ }^\circ\text{C}$  ( $1273\text{ K}$ ). The system of OTF-1200x-VHP-4 included a furnace for the heating unit outside and a chamber quartz tube for control the atmosphere. The graphite punches up from hydraulic on the bottom plate when graphite rods on top of the mold is pulled up and pressed with rods graphite top, it will cause the pressure within the mold to compound powder. The hot press furnace OTF-1200x-VHP-4 model at Sakon Nakhon Rajabhat University and schematic view of hot press machine and working chamber (Dobrzanski, *et al.*, 2017, pp. 17–52) as shown in Figure. 3.5



**Figure 3.5** The hot press furnace OTF-1200x-VHP-4 model at Sakon Nakhon Rajabhat University and schematic view of hot press machine and working chamber. (<https://www.mtixtl.com/VacuumHeatedPressingFurnace-OTF-1200X-VHP4.aspx>)

## CHARACTERIZATION TECHNIQUES

### Sample Identification

We identified a sample was made carried out using the X-ray diffraction (XRD) technique.

#### X-ray Diffraction Analysis

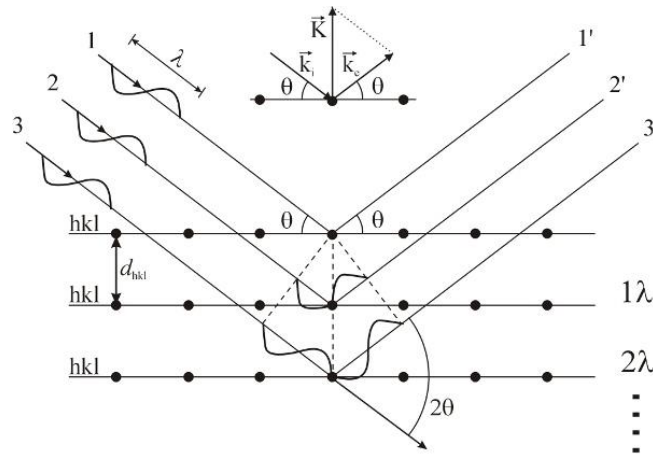
The characteristic x-ray diffraction pattern generated in a typical XRD analysis provides a unique “fingerprint” of the crystals present in the sample. When properly interpreted, by comparison with standard reference patterns and measurements, this fingerprint allows identification of the crystalline form. When a focused X-ray beam interacts with these planes of atoms, part of the beam is transmitted, part is absorbed by the sample, part is refracted and scattered, and part is diffracted. Diffraction of an X-ray beam by a crystalline solid is analogous to diffraction of light by droplets of water, producing the familiar rainbow. X-rays are diffracted by each mineral differently, depending on what atoms make up the crystal lattice and how these atoms are arranged (Pandian, 2014, pp.24). These result in diffraction in which X-rays are emitted at characteristic angles based on the spaces between the atomic planes in the crystal structure. Most crystals have many sets of planes passing through their atoms. Each set of planes has a specific interplanar distance and will give rise to a characteristic angle for diffracted X-rays. The basic principle of XRD is Bragg’s law, see Figure. 6, given by:

$$2d_{hkl} \sin \theta = n\lambda \quad (28)$$

Where  $d$ ,  $\theta$ ,  $\lambda$ , and  $n$  are lattice spacing, diffraction angle, the wavelength of the X-ray, and an integral number respectively. A set of ‘d-spaces’ obtained from a single



compound will represent the set of planes that can pass through the atoms and can be used for comparison with sets of d-spaces obtained from standard compounds (Overview, 2013).



**Figure 3.6** Diffraction (i.e. constructive interference of the scattered X-rays) will occur if the Bragg condition (eq. 28) is fulfilled and of the scattering vector  $K$  is parallel to the normal of the  $hkl$ -planes. (Meyers, 1997)

### Crystallite size

The Scherrer equation, in X-ray diffraction and crystallography, is a formula that relates the size of sub-micrometer crystallites in a solid to the broadening of a peak in a diffraction pattern. It is often referred to, incorrectly, as a formula for particle size measurement or analysis. It is named after Paul Scherrer (Scherrer, Göttinger, 1918, pp. 98; Patterson, 1939, pp. 978–982). It is used in the determination of size of crystals in the form of powder. The crystallite size of all samples was involuted from the modified Scherrer's formula as follows:

$$D = K\lambda / \beta_{hkl} \cos \theta \quad (29)$$

where  $D$  is crystalline size,  $K$  is shape factor (0.9), and  $\lambda$  is 1.5406 Å wavelength of Cu-K $\alpha$  radiation,  $\beta_{hkl}$  is full width at half maximum (FWHM) and  $\theta$  is the Bragg's angle (in radians). A broadening due to lattice strain was accorded by Wilson. (Wilson, 1949; Purushotham, 2013, pp. 973–976).

The X-ray diffraction (XRD, Shimadzu, XRD-6100) measurements was performed on Center of Excellence on Alternative Energy at Sakon Nakhon Rajabhat University, Thailand as shown in Figure 3.7. The crystal structure was analyzed by X-ray diffractometer by using Cu-K $\alpha$ 1 radiation at room temperature ( $\lambda = 1.5406$  Å) in scan range 20–80 degree of  $2\theta$  for 2 deg/min of scan speed with 0.02 of sampling pitch.



**Figure 3.7** X-ray diffractometer of Center of Excellence on Alternative Energy at Sakon Nakhon Rajabhat University.

## MICROSTRUCTURE CHARACTERIZATION

The surface microstructure measurement was revealed by the Field Emission Scanning Electron Microscopy JSM-7610FPlus, JEOL (FE-SEM).

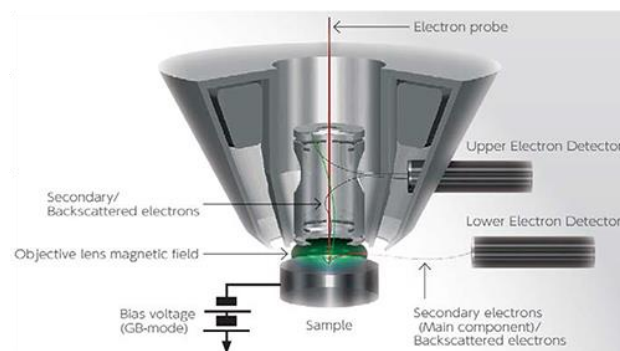
### Field Emission Scanning Electron Microscopy

Field emission scanning electron microscopy (FESEM) provides topographical and elemental information at magnifications of 10x to 300,000x, with virtually unlimited depth of field. Compared with convention scanning electron microscopy (SEM), field emission SEM (FESEM) produces clearer, less electrostatically distorted images with spatial resolution down to 1 1/2 nanometers – three to six times better. The FE-SEM observations were performed on JEOL Ultra-high Resolution Scanning Electron Microscope JSM-7610FPlus as shown in Figure 3.8. Preparation of n-CaMnO<sub>3</sub> and p-Ca<sub>3</sub>Co<sub>4</sub>O<sub>9</sub> samples were desiccated at least 2 days and heated for reduce the moisture for positive photoresists due to imaging and measurements on wet samples, as-is, is not possible. For imaging and determining the distribution of particles in powder samples, we suggest drop-casting of the sample on any conducting substrate. After that n-CaMnO<sub>3</sub> and p-Ca<sub>3</sub>Co<sub>4</sub>O<sub>9</sub> samples have been sputter-coated with a thin layer of platinum or gold prior observation.



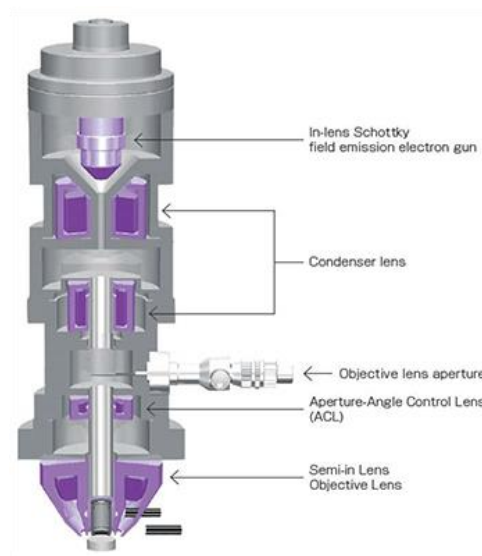
**Figure 3.8** The FE-SEM observations were performed on a JEOL Ultra-high-Resolution Scanning Electron Microscope JSM-7610FPlus at Ubon Ratchathani University and preparation the powder and bulk  $n\text{-CaMnO}_3$  and  $p\text{-Ca}_3\text{Co}_4\text{O}_9$  materials (drop casting and coating).

The Semi-in lens type objective lens and High-Power Optics of the irradiation system deliver high-spatial resolution observation and stable analysis capability. The schematic diagram semi-in Lens objective lens of the FE-SEM equipment is shown in figure 3.9.



**Figure 3.9** The schematic diagram semi-in Lens objective lens of the FE-SEM equipment.

A unique electron optical system allows a variety of analyses and observation at high magnification. The in-lens Schottky field emission electron gun, which can deliver a probe current 10 times that of the conventional Schottky field emission electron gun (FEG), along with the aperture-angle control lens (ACL) that can maintain a small probe diameter with the appropriate convergence angle even with the increased probe current, makes it possible to use probe currents of 200 nA or more. The high-power optics provides all the performance you need to conduct everything from high magnification viewing to EDS and EBSD analyses (<https://www.jeol.co.jp/en/products/detail/JSM-7610FPlus.html>). The schematic diagram high power optics of the FE-SEM equipment is shown in figure 3.10



**Figure 3.10** The schematic diagram high power optics of the FE-SEM equipment.

## Extensibility: Energy Dispersive X-ray Spectrometer (EDS)

The High-Power Optics make it possible to effectively take advantage of the features of the EDS (SDD: Silicon Drift Detector) detector that is difficult to saturate even with large probe currents. By using a low accelerating voltage and a large probe current, good quality mappings can be obtained in a very short period. The EDS analysis here was performed on a Field Emission Scanning Electron Microscopy JSM-7610FPlus, JEOL (FE-SEM).

## THERMOELECTRIC PROPERTIES MEASUREMENTS

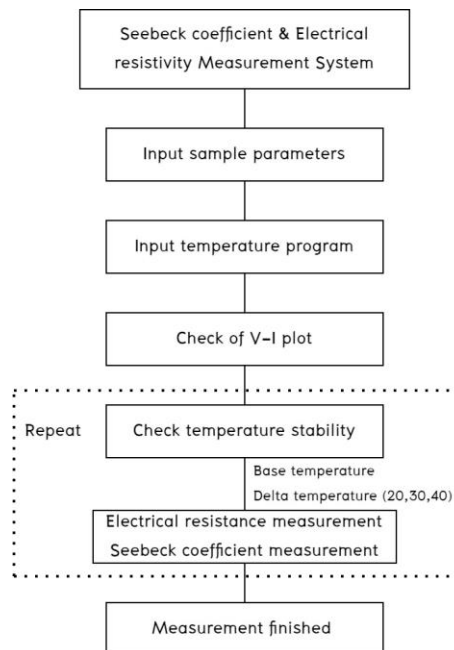
### Seebeck Coefficient / Electric Resistance Measurement System ZEM-3 series



**Figure 3.11** The Seebeck Coefficient / Electric Resistance Measurement System, ZEM-3

The ZEM-3 unit is the worldwide de facto standard for thermoelectric material measurements at temperatures from  $-130^{\circ}\text{C}$  to  $1,000^{\circ}\text{C}$ . Easy to use straightforward operation with great accuracy & repeatability is why the ZEM-3 becomes the favorite instrument in many labs across the globe. The Seebeck Coefficient / Electric Resistance Measurement System as shown in Figure. 3.11. The Seebeck coefficient and electrical

resistivity were measured by ZEM3 (Advantec, Inc) in vacuum with the step detail as shown in Figure. 3.12 (<https://www.ulvac.co.th/rd-th/zem-3/>).

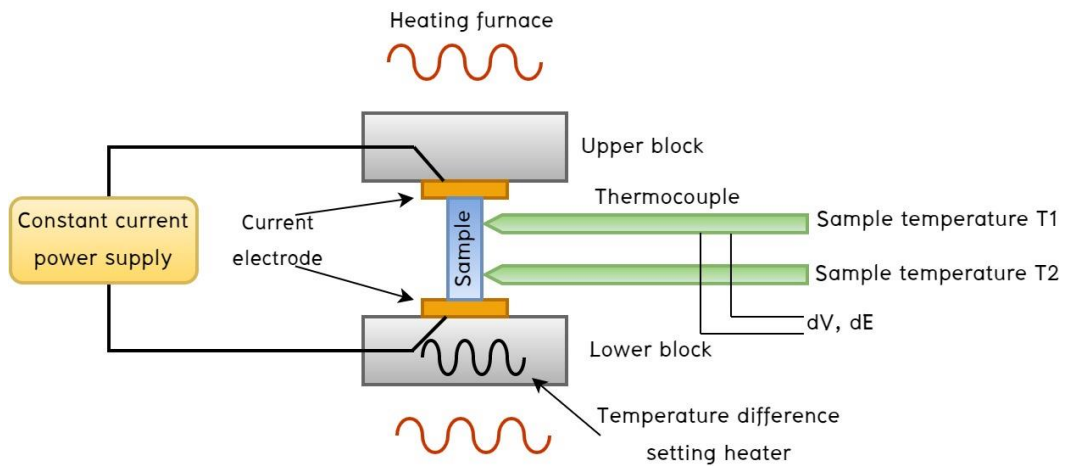


**Figure 3.12** Schematic diagram of the step detail for Seebeck coefficient and electrical resistivity measurement.

### Measurement principle

A prism or cylindrical sample is set in a vertical position between the upper and lower blocks in the heating furnace. While the sample is heated, and held, at a specified temperature, it is heated by the heater in the lower block to provide a temperature gradient. Seebeck coefficient is measured by measuring the upper and lower temperatures  $T_1$  and  $T_2$  with the thermocouples pressed against the side of the sample, followed by measurement of thermal electromotive force  $dE$  between the same wires on one side of the thermocouple. Electric resistance is measured by the dc four-terminal method, in which a constant current  $I$  is applied to both ends of the sample to measure and determine voltage drop  $dV$  between the same wires of the

thermocouple by subtracting the thermo-electromotive force between leads as shown in Figure. 3.13 (<https://www.ulvac.co.th/rd-th/zem-3/>)



**Figure 3.13** The schematic diagram of Seebeck coefficient and electrical resistivity measurement. (<https://www.ulvac.co.th/rd-th/zem-3/>)



The n-CaMnO<sub>3</sub> and p-Ca<sub>3</sub>Co<sub>4</sub>O<sub>9</sub> samples were measured by using ZEM-3 followed the conditions as shown in Table 3.5.

**Table 3.5:** ZEM-3 conditions of n-CaMnO<sub>3</sub> and p-Ca<sub>3</sub>Co<sub>4</sub>O<sub>9</sub> sample

Materials	n-CaMnO <sub>3</sub>	p-Ca <sub>3</sub> Co <sub>4</sub> O <sub>9</sub>
Shape of sample	Rectangular	Rectangular
Sample size (width × Depth mm <sup>2</sup> )	4.051 × 3.950	2.972 × 1.138
Temperature range (K)	373 – 973 K	373 – 973 K
Measurement method	Four-probe method	Four-probe method
Atmosphere	Helium	Helium
Lead interval (mm)	5.340	5.795
Delta temperature	20–30–40	20–30–40

#### Thermal Conductivity of n-CaMnO<sub>3</sub> and p-Ca<sub>3</sub>Co<sub>4</sub>O<sub>9</sub>

The thermal conductivity can be calculated from the thermal diffusivity ( $\alpha$ ), heat capacity  $C_p$ , and density of bulk  $d$  by the equation as the following:

$$\kappa = \alpha C_p d \quad (30)$$

The thermal diffusivity values ( $\alpha$ ) were measured by laser flash technique (Netzsch LFA-467, Germany) from room temperature to 973 K in argon atmosphere. In this study the specific heat capacity ( $C_p$ ) was estimated from  $3nR$ , where  $n$  is the number of atoms per formula unit and  $R$  is the gas constant.

## DENSITY DETERMINATION OF SOLIDS

The density of bulk samples was determined by density kit (Mettler Toledo, MS-DNY-54) with deionization water for auxiliary liquid. Density determinations are frequently performed by Archimedes' principle, which is also used with the density determination kit for the balances. This principle states that every solid body immersed in a fluid apparently loses weight by an amount equal to that of the fluid it displaces. The procedure for the density determination by Archimedes' principle depends on whether the density of solids or liquids must be determined.

The density of a solid is determined with the aid of a liquid whose density  $\rho_0$  is known (water or ethanol are usually used as auxiliary liquids). The solid is weighed in air (A) and then in the auxiliary liquid (B). The density  $\rho$  can be calculated from the two weighing as follows:

$$\rho = \frac{A}{A - B}(\rho_0 - \rho_L) + \rho_L \quad (31)$$

$$V = \alpha \frac{A - B}{\rho_0 - \rho_L} \quad (32)$$

Where  $\rho$  is the density of the sample, A is weight of the sample in air, B is weight of the sample in the auxiliary liquid,  $V$  is volume of the sample,  $\rho_0$  is density of the auxiliary liquid,  $\rho_L$  is density of air (0.0012 g/cm<sup>3</sup>), and  $\alpha$  is weight correction factor (0.99985), to take the atmospheric buoyancy of the adjustment weight into account. ([https://www.mt.com/id/en/home/library/operating-instructions/laboratoryweighing/NC\\_density\\_OI/jcr:content/download/file/file.res/Operating\\_Instructions\\_Density%20Kit\\_\(OP-EN\).pdf](https://www.mt.com/id/en/home/library/operating-instructions/laboratoryweighing/NC_density_OI/jcr:content/download/file/file.res/Operating_Instructions_Density%20Kit_(OP-EN).pdf))

## Dimensionless Figure of Merit

The dimensionless figure of merit ( $ZT$ ) was calculated by using the above mentioned values of the Seebeck coefficient ( $S$ ), electrical resistivity ( $\rho$ ) and thermal conductivity ( $\kappa$ ), consider by the relation (Rowe, 2005)

## Conversion Efficiency of Thermoelectric Cell and Module

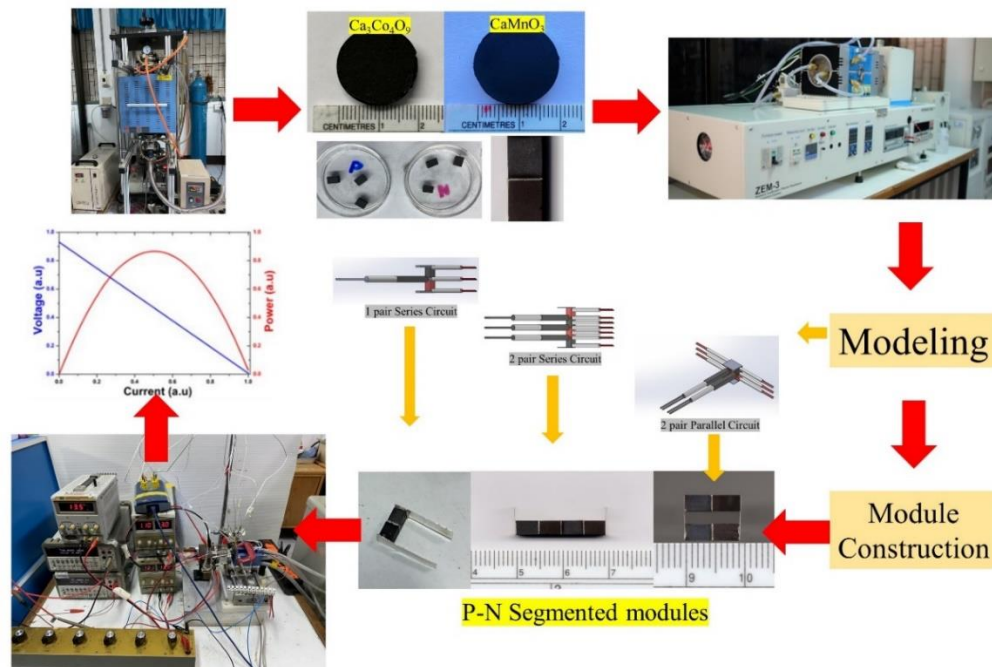
The efficiency of a thermoelectric converter depends heavily on the temperature difference  $\Delta T = T_h - T_c$  across the device. This is because the thermoelectric generator, like all heat engines, cannot have an efficiency greater than that of a Carnot cycle ( $\Delta T / T_h$ ). The efficiency of a thermoelectric generator is typically defined as (Snyder, 2008, pp. 54)

$$\eta = \frac{\Delta T}{T_h} \cdot \frac{\sqrt{1 + ZT} - 1}{\sqrt{1 + ZT} + T_c / T_h} \quad (33)$$

Where the first term is the Carnot efficiency and  $ZT$  is the figure of merit for the device.

## Thermoelectric module fabrication and measurement

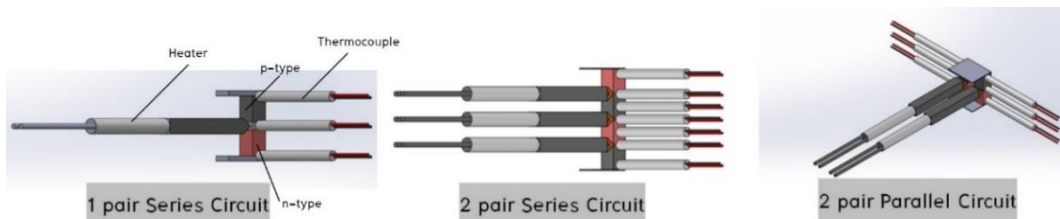
Figure 3.14 shows the whole process of segmented module fabrication used in this thesis. The materials of n-CaMnO<sub>3</sub> and p-Ca<sub>3</sub>Co<sub>4</sub>O<sub>9</sub> were first synthesized and followed by characterization step. The legs were then cut into fixed dimensions according to the literature reviews (Funahashi, 2021, pp. 3996–4005). The modeling is used to design measurements system and appropriate output performance. It is seen from Figure. 3.14 that all the step connection in series if any step is failed the process is required restart from fabricated material step.



**Figure 3.14** Schematic of the whole thermoelectric segmented module construction process from sintering and characterized materials to modelling for measurements, built-up and test modules.

### 1. Thermoelectric module design

Segmented thermoelectric devices were designed by solid works program and assembly by soldering method. The design of thermoelectric device was stated from assigning materials size of  $3.5 \times 3.5 \times 5 \text{ mm}^3$  and Ag electrode size of  $3.5 \times 3.55 \times 0.1 \text{ mm}^3$  as shown in Figure. 3.15



**Figure 3.15** Model design of segmented thermoelectric device configuration.

For the fabrication of segmented legs, the obtained pellets of CCO and CMO were cut into rectangular pieces. Before the joining step, it is crucial that the surface to be joined is prepared and cleaned. First, the joining pieces were polished to remove residues from the previous cutting process. The polishing also provides adequate surface flatness to proceed joining. Then, the polished pieces were cleaned by ultrasonication for 3 minutes in solutions of acetone. 0.1 mm thick Ag sheet with a purity of 99.99% was used to make electrodes and joining material between the CMO and the CCO. Brazing joining process was conducted in air using the silver paste at 1 mm thickness. After joining the oxide legs and Ag sheets, the joint was dried at 423 K for 10–15 min and then firing up at 1023 K for 10 min to establish good electrical contact between the metal electrodes and semiconducting oxides.

## **2. Segmented modules fabrication**

In the fabrication of a segmented TEG, besides the contact with the electrode, the creation of good contact between the TE materials is highly important. A good contact should address the following requirements:

1. Good adhesion between materials.
2. The contact resistance formed at the junction is as small as possible so that the electrical and thermal currents run in TEGs are not severely influenced (Matchanov, 2011, pp. 90–97, 2011) and consequently the overall efficiency is maintained.
3. The bond between the materials is chemically stable under conditions that are like the operating condition in real applications. Inter-diffusion between adjacent materials that might cause detrimental change in TE properties of materials should be prohibited. Oxidation of materials used for joining is also an obstacle that needs to be circumvented.

To meet the quality standard, in each joining case, a process including the selection of joining methods and joining materials should be considered.

### **Joining methods**

Materials with different chemical and physical properties require correspondingly different joining methods and procedures. Quality of joining and interfacial evolution behavior play a critical role in the performance and reliability of thermoelectric (TE) devices. In the typical cases of joining TE materials, it is critical that the processing temperature during joining is higher than the highest working temperature expected for the legs but lower than the melting / phase change temperature of the materials (D'Angelo, 2007, pp. 2–8, 2007) These are the two main joining concepts to join different materials: diffusion bonding and brazing or soldering.

#### **Diffusion bonding**

Diffusion Bonding is a solid–state joining process this is applicable to similar and dissimilar materials, primarily metals, although ceramic materials can also be joined using this process. The process works through the diffusion of atoms across the joint interface at elevated temperatures. Diffusion bonding does not require any filler materials, and for similar materials joint, it is completely autogenous. When diffusion bonding dissimilar materials, interlayers can be used. A typical commercial diffusion bonding furnace is a vacuum furnace, with hydraulic rams present to apply pressure through graphite tooling and into the parts to be joined. This process is known as uniaxial diffusion bonding. As the process relies on diffusion, applying pressure is required to bring the two surfaces into intimate contact, and thus promote increased diffusion across the interface(s). For this reason, the surface roughness and flatness of

the parts being joined are important process parameters. Higher temperatures are required for materials with a higher melting point, as the diffusion bonding temperature is typically 50–80% of the material's melting point. Certain materials are not compatible with high vacuum conditions, in which case, diffusion bonding under the partial pressure of an inert gas, such as Argon or N<sub>2</sub>, is common (<https://www.twi-global.com/what-we-do/our-processes/diffusion-bonding>).

### **– Brazing / soldering**

Brazing and soldering is also a popular joining method where bonding is made by the melting of a third material inserted between the pieces needed to be joined. The only difference between brazing and soldering is the temperature at which each process takes place. Soldering takes place at a temperature below 840°F (450°C), and brazing occurs at a temperature above 840°F (450°C). Brazing and soldering method, like diffusing bonding, usually needs to be done in a protective atmosphere due to the risk of oxidation.

### **Advantages of Brazing and Soldering**

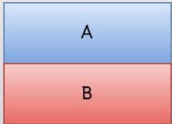
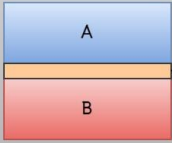

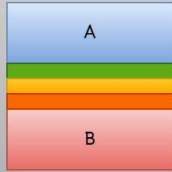
Some advantages of brazing and soldering as compared to other methods of joining include the following:

1. Low temperature
2. May be permanently or temporarily joined
3. Dissimilar materials can be joined
4. Speed of joining
5. Less chance of damaging parts
6. Slow rate of heating and cooling
7. Parts of varying thicknesses can be joined
8. Easy realignment

Brazing and soldering are processes that have many great advantages but are often overlooked when a joining process is being selected. The ability to join many different materials with a limited variety of fluxes and filler metals reduces the need for a large inventory of materials, which can result in great cost savings for a laboratory scale (<https://www.uti.edu/blog/welding/brazing-soldering-welding>).

Figure 3.16 shows a chart describing and comparing the two joining methods. A, B are subject materials to be joined and C is the filler material utilized for making the bond. Compared to diffusion bonding, brazing/soldering method has the benefit of lower processing temperatures. However, the brazing/soldering method might have a drawback of introducing more interphase between A and B due to interdiffusion reactions of the present materials.



Step 1 Surface cleaning	Clean the joining surface	
Step 2 Surface treatment	Coat a buffer layer on joining surfaces. Propose: to prevent surface oxidation prior to joining, fill in surface voids, diffusion barrier, etc.	
Step 3 Joining	<p><b>Diffusion bonding</b></p> <p><i>During joining</i></p>  <p>Pressure Temperature Atmosphere</p> <p><i>After joining</i></p>  <p>Diffusion layer A and B</p>	<p><b>Brazing/soldering</b></p> <p><i>During joining</i></p>  <p>Pressure Temperature Brazing: <math>T &gt; 723\text{ K}</math> Soldering: <math>T &lt; 723\text{ K}</math> Atmosphere</p> <p>Filler material C</p> <p><i>After joining</i></p>  <p>Interdiffusion layers A and C B and C</p>
Temperature	At least 50–80% of the lowest melting point among A and B	Melting/ solidus/ liquidus point of filler C
Pressure	Enhance physical contact between joining materials : Fill in surfacial voids	
Atmosphere	Vacuum/ inert/ reductive ambient to prohibit oxidations	
Features	<ul style="list-style-type: none"> <li>–No addition of materials, thus avoid the formation of undesired interphase</li> <li>–Provide stability at high temperature</li> </ul>	<ul style="list-style-type: none"> <li>–Application to cases required low processing temperature</li> <li>–Formation of new interphases and their influence on the overall performance should be studied</li> </ul>

**Figure 3.16** Schematic joining steps in diffusion bonding and brazing/soldering

methods and comparison between them.

### How to Select an appropriate joining method

The good requirements of contact electrodes in the fabrication of TEG the coefficient of thermal expansion of the joining should be matches those of thermoelectric materials. If the coefficient of thermal expansion mismatches between materials will increase the probability that serves the problems of delamination or debonding after we put a thermal cycle for TEG. Especially, the diffusion of the filler into the TE during operation which reduces the performance reliability needs to be

avoided and the filler should be chemically stable with no oxidation or reduction under the working conditions (Xia, 2014, pp. 1716–1723, 2014).

## Contact resistance of segmented thermoelectric modules

Thermal and electrical contact resistance

The main challenge for fabricated of segmented thermoelectric materials is how to make the minimum contact resistance between n-CaMnO<sub>3</sub> / p-Ca<sub>3</sub>Co<sub>4</sub>O<sub>9</sub> materials and the other areas of thermoelectric modules. Minimum contact resistances are essential to make a high segmented TEG performance. In general, whenever two materials are connected on each other, it will be a “contact resistance” at the interface, both electrically and thermally as shown in Figure. 3.17.

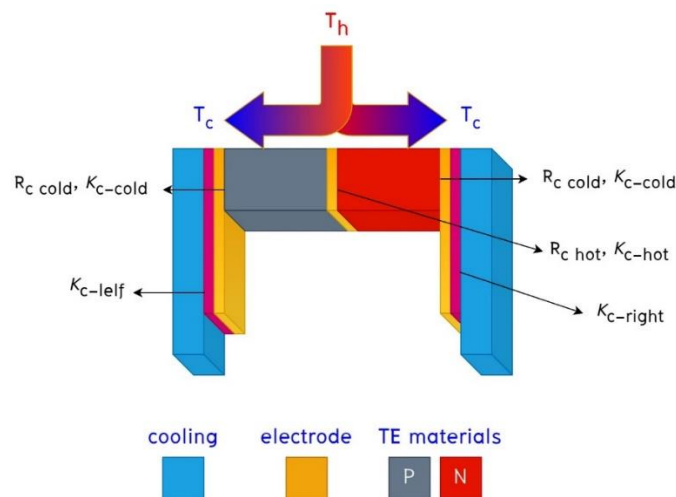
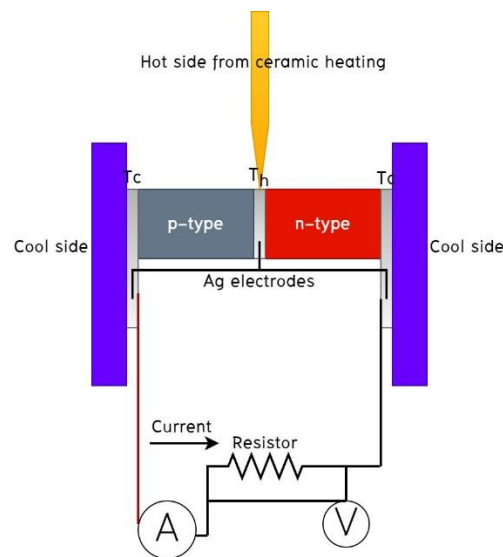


Figure 3.17 Sources of contact resistance in a TEG

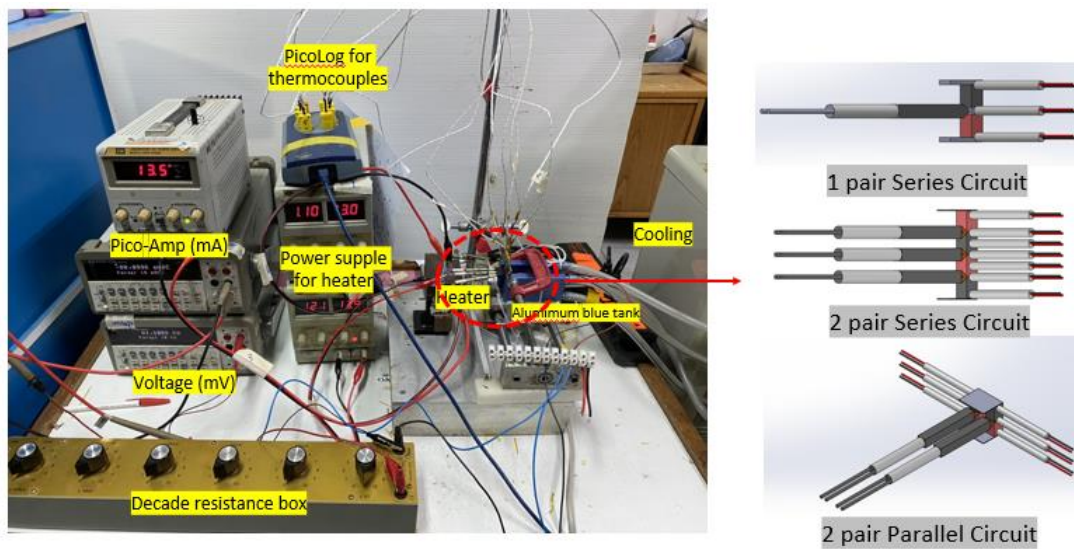
### 3. Segmented thermoelectric generator tester

The thermoelectric performance of fabricated thermoelectric generators, including output voltage, current and power, has been measured by a test system built in-laboratory. In principle, the system consists of two parts: a temperature controller to create temperature gradient and an electrical controller to measure the thermoelectric characteristics of the in-test TEG. The heat applied at the hot side is

power supply and produced by a ceramic heating core cover with copper sheets for nearby of each junction. The cold side temperature is maintained by running water with controllable temperature on aluminum tank. The TEG is settled between the aluminum tank and junction areas with heaters to keep good thermal contact between the junctions. Under a temperature gradient, the TEG generates an electrical voltage. The TEG is connected in series with an external load ( $R_{shunt}$ ) and an electronic load (E.load) which control the current run in the whole circuit. The designed measurement system can set up the measuring current range with the minimum 1 mA step size, while the electronic load is applied and scanned until reaching a value closet the defined current together with the measured voltage of TEG. To define the accurate temperature gradient, thermocouples with wire diameters of 0.4 mm were placed on the Ag electrodes at the hot side, the cold side, and some surface area of module, respectively. It is seen from Figure. 3.18.



**Figure 3.18** Schematic principle of the thermoelectric generator tester



**Figure 3.19** Photo of the TEG thermoelectric output test system

## References

- A. J. C. Wilson, X-ray optics, Methuen & Co. Ltd., London. (1949)]. [E. Purushotham, N.G. Krishna, Bull. Mater. Sci. 36[6], 973–976 (2013).
- D'Angelo, J. J., Timm, E. J., Ren, F., Hall, B. D., Case, E., Schock, H., & Hogan, T. P. (2007). Electrical Contact Fabrication and Measurements of Metals and Alloys to Thermoelectric Materials. *MRS Online Proceedings Library (OPL)*, 1044.
- Dobrzański, L. A., Dobrzańska-Danikiewicz, A. D., Achteik-Franczak, A., Dobrzański, L. B., Hajduczek, E., & Matula, G. (2017). Fabrication technologies of the sintered materials including materials for medical and dental application. *Powder Metallurgy–Fundamentals and Case Studies, InTech, Rijeka, Croatia*, 17–52.
- Funahashi, R., Matsumura, Y., Urata, T., Murakami, H., Ikenishi, H., Sasaki, S., & Sugiyama, S. (2021). Relationship Between Tensile Strength and Durability of Oxide Thermoelectric Modules. *Journal of Electronic Materials*, 50(7), 3996–4005.
- H. Xia, F. Drymiotis, C.–L. L. Chen, A. Wu, and G. J. Snyder, “Bonding and interfacial reaction between Ni foil and n-type PbTe thermoelectric materials for thermoelectric module applications,” *J. Mater. Sci.*, vol. 49, no. 4, pp. 1716–1723, 2014.
- Meyers, H. P., & Myers, H. P. (1997). *Introductory solid state physics*. CRC press.
- N. A. Matchanov, M. Farhan, E. J. Timm, T. P. Hogan, H. Schock, E. D. Case, and M. G. Kanatzidis, “Investigation of the Hot Side Contacts to Nanostructured LASTt (T) Material. Part I,” *Appl. Sol. energy*, vol. 47, no. 2, pp. 90–97, 2011
- Overview, D. D. (2013). *Advanced X-ray Diffraction System for Materials Research Applications*.

Pandian, M. S. (2014). X-ray diffraction analysis: Principle, Instrument and Application. *Pondicherry University Puducherry, INDIA*, 34.

P. Scherrer, Göttinger Nachrichten Gesell., Vol. 2, 1918, p 98.] [Patterson, A. (1939). "The Scherrer Formula for X-Ray Particle Size Determination". *Phys. Rev.* 56 (10): 978–982.

Purushotham, E., & Krishna, N. G. (2013). X-ray determination of crystallite size and effect of lattice strain on Debye–Waller factors of platinum nano powders. *Bulletin of Materials Science*, 36(6), 973–976.

Rowe, D. M. (2005). *Thermoelectrics handbook: macro to nano*: CRC press.

Snyder, G. J. (2008). Small thermoelectric generators. *The Electrochemical Society Interface*, 17(3), 54.

Wilson, A. J. C. (1949). X-ray optics, Methuen & Co. Ltd., London.

<https://www.micronanotools.com/products/planetary-ball-mill-4x100ml-two-year-warranty-vacuum-and-inert-gas-grinding-compatible>

<https://www.mtixtl.com/VacuumHeatedPressingFurnace-OTF-1200X-VHP4.aspx>

<https://www.jeol.co.jp/en/products/detail/JSM-7610FPlus.html>

<https://www.ulvac.co.th/rd-th/zem-3/>

[https://www.mt.com/id/en/home/library/operatinginstructions/laboratoryweighing/NC\\_density\\_OI/jcr:content/download/file/file.res/Operating\\_Instructions\\_Density%20Kit\\_\(OP-EN\).pdf](https://www.mt.com/id/en/home/library/operatinginstructions/laboratoryweighing/NC_density_OI/jcr:content/download/file/file.res/Operating_Instructions_Density%20Kit_(OP-EN).pdf)

<https://www.twi-global.com/what-we-do/our-processes/diffusion-bonding>

<https://www.uti.edu/blog/welding/brazing-soldering-welding>

## CHAPTER 4

### RESULTS AND DISCUSSION

The experimental results and discussion reported in this chapter can be divided into three sections. The first section explains the preparation n-CaMnO<sub>3</sub> and p-Ca<sub>3</sub>Co<sub>4</sub>O<sub>9</sub> characterization including phase identification, crystallography, morphology. The second section of each materials explained to thermoelectric properties such as electrical resistivity, Seebeck coefficient, thermal conductivity to calculate power factor and dimensionless figure of merit are presented and discussed. The third section observed that the process for fabricated of thermoelectric multilayers generator of n-CaMnO<sub>3</sub>/p-Ca<sub>3</sub>Co<sub>4</sub>O<sub>9</sub> such as joining process, thermoelectric properties of multilayers n-CaMnO<sub>3</sub>/p-Ca<sub>3</sub>Co<sub>4</sub>O<sub>9</sub> of 1 and 2 pairs and how to test thermoelectric multilayer generators.

#### Thermoelectric Materials Synthesis

##### n-CaMnO<sub>3</sub>: Crystal Structure and Chemical Composition

###### Structure and Phase Analysis.

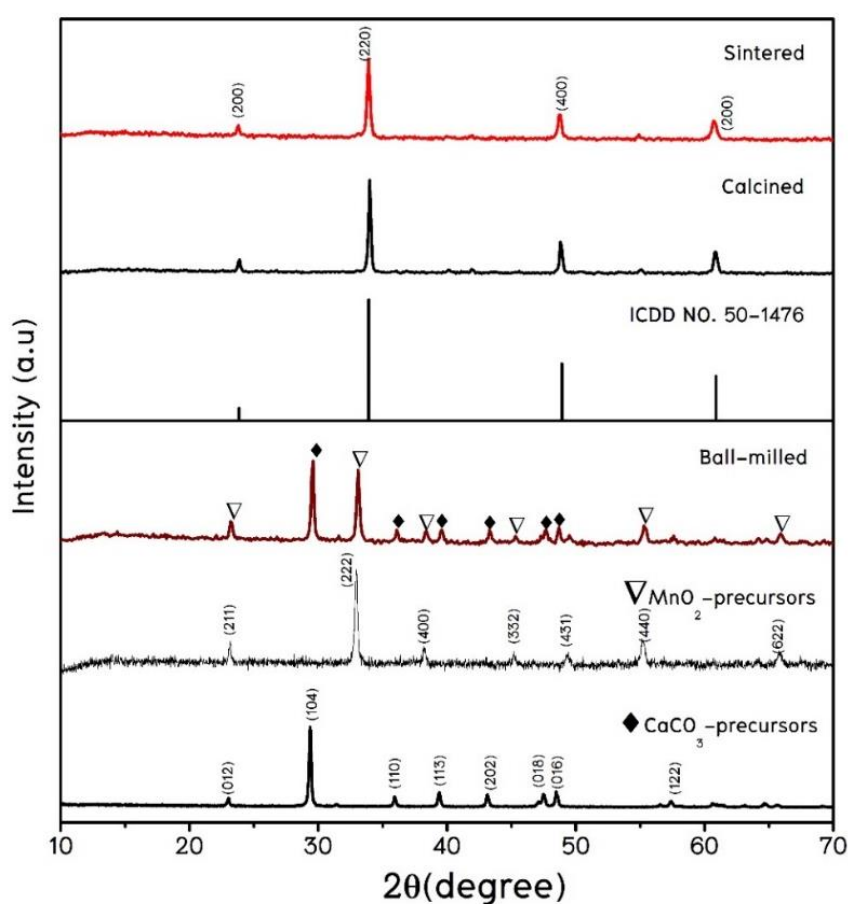
The CaMnO<sub>3</sub> powders were synthesized by two precursors: CaCO<sub>3</sub> nano powders and MnO<sub>2</sub> nano powder. After CaCO<sub>3</sub> and MnO<sub>2</sub> nanoparticles were mixed by a ball mill with increasing to 8 h where milling results in an enhanced homogeneity

rather than in increased particle comminution and calcined powder precursors at 1123 K for 10 h under oxygen atmosphere.

As reported, increased milling time decreases the particle size of powders which leads to increase the diffusion kinetics during sintering. It can be seen from the results that the samples calcined at a lower temperature under oxygen atmosphere demonstrate homogeneously dispersed nanoparticles are observed with connected network structure is due to the recovery of oxygen atoms from the atmosphere. The addition of PVA for hot-press sintering process as a capping agent improves the crystallinity and reduces the average crystallite size of these samples which is in good agreement with the report data (Mary, S. B. & Rajesh, A. L., 2019, pp. 464–468). Therefore, the HP-sintering is sufficient for complete phase formation can be achieved either at lower sintering temperature 873 K with shortest dwell time of 1 h. The XRD patterns of  $\text{CaMnO}_3$  samples are exhibited in Figure 4.1. As  $\text{CaCO}_3$  and  $\text{MnCO}_3$  both crystallize in a calcite-type structure, it can be deduced that a solid solution forms in the milling process. The crystal size of the solid solution is obtained by applying the Scherrer equation to the peaks a mean crystallite size of  $10.5 \pm 0.6$  nm results. By further milling (times > 5 h) the intensity of the peaks tends to increase: this fact is likely to be due to the crystallization of the solid solution. All  $\text{CaMnO}_3$  samples are single-phase and major crystal phase of all samples without any detectable secondary phase and can be indexed with orthorhombic *Pnma* symmetry matched with the ICDD card of  $\text{CaMnO}_3$  No.:50-1476 (Mouyane, M., *et al.*, 2014, pp. 71 — 77.). The diffraction peaks became sharper, which could be explained by the increase in grain size. It is interesting to observe that the lattice parameter, average crystallite size, density, and theoretical density as shown in table 4.1. It has been reported that the lattice parameter increases or decreases as a function of the crystallite size in the



structural and it can make a change in the properties of these materials (Dittrich, M. & Schumacher, G., 2014, pp. 27–33.) (Qi, W. H. & Wang, M. P., 2005, pp. 51 – 57.). The thermoelectric ceramics in both studies showed quite low densities of 68 – 81% (Bocher, L., *et al.*, 2008, pp. 8077 – 8085.). The highest density of  $\text{CaMnO}_3$  sample is 58.92% of theoretical density. The low-density undoped sample is more likely to lose more oxygen at elevated temperatures.

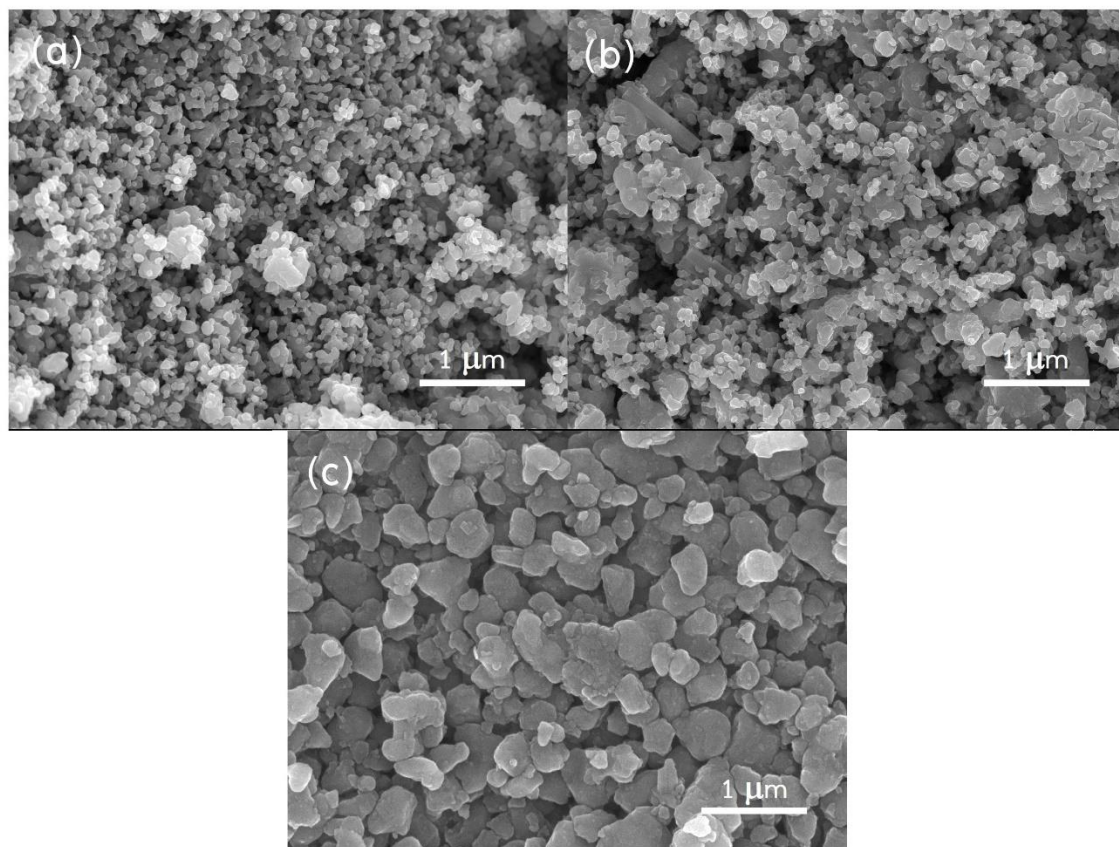


**Figure 4.1** XRD pattern of  $\text{CaMnO}_3$  samples with ball-milled, calcined and sintered.

**Table 4.1.** Crystallographic parameters with average crystallite size, density, and relative density of  $\text{CaMnO}_3$  nanoparticles (the theoretical density of  $\text{CaMnO}_3$  is  $4.705 \text{ g/cm}^3$ ) (Ferreira, N. M, *et al.*, 2019, pp. 4184 — 4188.)

Sample	Lattice parameters			Average crystallite size (nm)	Density ( $\text{g/cm}^3$ )	Relative density %
	a (Å)	b (Å)	c (Å)			
Ball-milled	–	–	–	10.56		
Calcined	5.2778	7.4609	5.2743	42.3418	–	–
Sintered	5.2714	7.4708	5.2707	32.4390	2.772	58.92%
ICDD 50-1746	5.2820	7.4550	5.2660			

## Microstructure Analysis



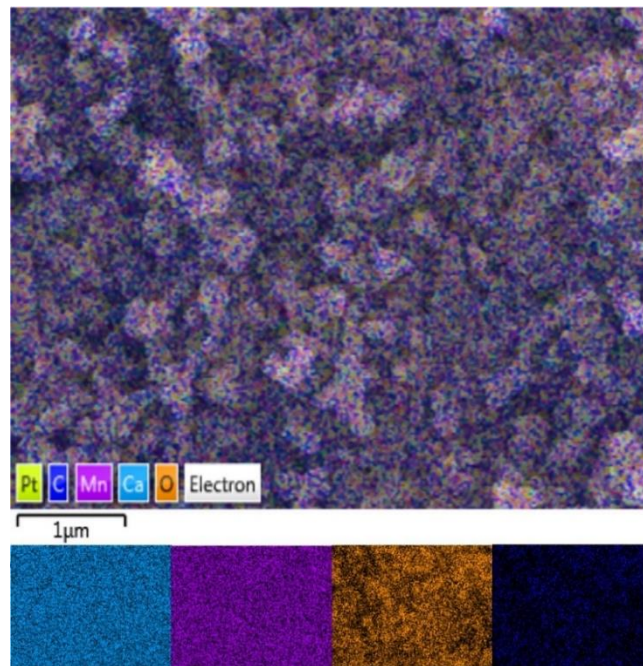
**Figure 4.2** SEM image of  $\text{CaMnO}_3$  powder after (a) ball-milling (b) calcined and (c) sintered.

The synthesis of  $\text{CaMnO}_3$  oxide has usually been performed by solid state reaction involving high temperature and long reaction time so leading to samples with large particle size. To try and solve this problem, different synthetic routes have been devised for this work describes a solid-state synthesis of  $\text{CaMnO}_3$  with precursor nanometric particle size. Figure. 4.2 SEM micrograph of  $\text{CaMnO}_3$  (a) ball-milling of the nano powder (high-energy ball milled powder with size < 50 nm). Whereas two well distinct morphological features are present in the sample of the physical mixture. The peak positions for the nano powder were identical to those of the ingot, which means

that there was no change of phase during the ball milling process. The SEM-images of (b) calcined was demonstrated that the powder has a bimodal particle size distribution, consisting of coarse and small particles of about 50 nm to 200 nm. (c) The sintered sample has spherical shape, and the size (>50 nm after HP-sintering under identical conditions at 873 K for 1 h by adding PVA for hot-press sintering can be inserted in the vacancy between the grain of materials, but we added in small quantities make low density of bulk. The relative density was decreased to the value of 58.92%. The low density of sample affected the thermoelectric properties. The elemental mapping of  $\text{CaMnO}_3$  bulk sample was obtained by Oxford Instruments detector. The elemental mapping samples shows homogenous distribution of Ca, Mn, O and C that confirmed completely by hot-pressing method. The energy dispersive X-ray spectroscopy (EDS) was analyzed, and show the results agree with the composition of initial atomic ratio, as shown in table 4.2.

**Table 4.2** The EDS of  $\text{CaMnO}_3$  bulk sample

Sample	Ca (%)	Mn (%)	C (%)	O (%)	Pt (%)
Sintered	25.99	35.99	2.46	32.68	2.88



**Figure 4.3** Elemental mapping of  $\text{CaMnO}_3$  surface bulk sample.

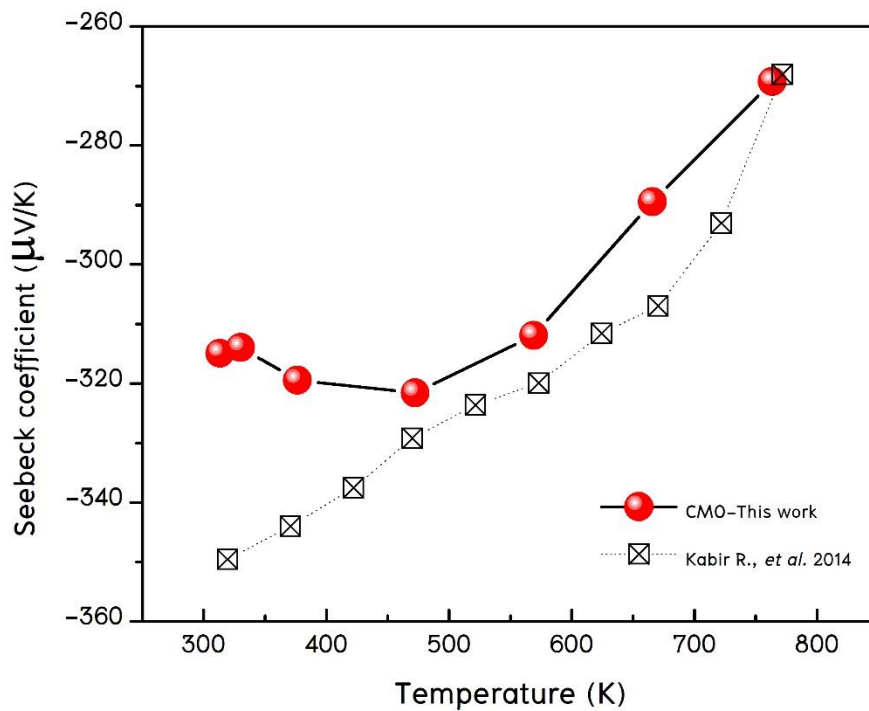
### **n- $\text{CaMnO}_3$ : Thermoelectric properties**

The values of the Seebeck coefficient depends strictly on the electronic structure of the material (Wang Y, *et al.*, 2009, pp. 4653–4660.). The negative value of  $S$  is characteristic of n-type material, in which the electrons are the major charge carriers. When the material is submitted to a gradient temperature, it presents a higher concentration of electrons on the hot side, creating an opposite electrical voltage with temperature gradient (Paengson S, *et al.*, 2017, pp. 6289–95.). The modulus of Seebeck coefficient values decreases with the increasing temperature, which may explain the behavior of the semiconductor material due to an increase in the concentration of the carriers with the temperature (Park JW, Kwak DH, Yoon SH & Choi SC., 2009, pp. 550–5.). For the temperatures above 600 K occurs the stabilization the effect, in which the Seebeck coefficient is not dependent on the temperature. The Seebeck coefficient can be given by the model proposed for degenerate

semiconductors (Cutler M, Leavy JF & Fitzpatrick RL. 1964, pp. A1143–52.), as expressed in Equation 34.

$$S = \left( \frac{8\pi^2 k_B^2}{3eh^2} m^* T \right) \left( \frac{\pi}{3n} \right)^{2/3} \quad (34)$$

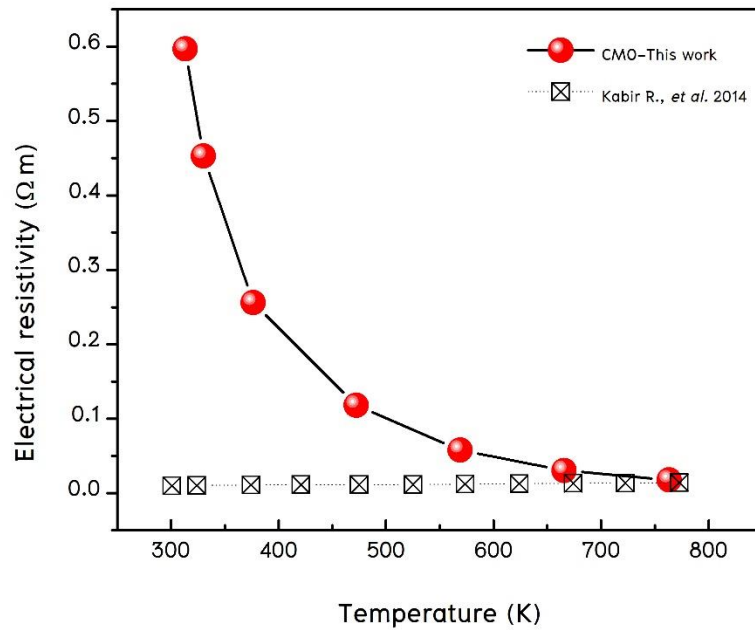
Where  $k_B$  is the Boltzmann constant and  $n$  and  $m^*$  refer to the carrier concentration and the effective mass of the carrier, respectively. The absolute values of  $S$  increase with rising temperature, indicating metallic to semiconducting transition in the range 273 – 723 K as shown in Figure 4.4. The similar phenomenon was also reported for the  $\text{CaMnO}_3$  system (Thiel P, Populoh S, Yoon S, Saucke G, Rubenis K, & Weidenkaff A., 2015, pp. 21860–7.). However, the  $S$  of these sample shows a slightly different behavior, they possess lower values from room temperature to 473 K and higher values at higher temperatures. The sintered sample has  $S$  lower values because this sample is the capacity to compact the powder into a dense bulk within short times owing to the self-heat effect makes a low densified with larger grain size increases the influence on the  $S$  values of the scattering effect will be decreased. The highest value of  $S$  is  $-269.219 \mu\text{V/K}$  at 763 K. The formation of oxygen vacancies can introduce more electrons into the undoped  $\text{CaMnO}_3$  system, thus increase the carrier concentration, leading to the lower absolute value of the Seebeck coefficient.



**Figure 4.4** Dependence of  $S$  on the temperature of the nanocrystalline  $\text{CaMnO}_3$  sample.

Figure 4.5 the dependence of the  $\rho$  on the temperature of  $\text{CaMnO}_3$  sample similarly behaviour corresponding with metal to semiconducting transition in the range 273 — 723 K which is in good agreement with the literature data. (Flahaut, D. *et al.*, 2006, pp. 084911.) [Kabir, R., *et al.*, 2014, pp. 7522 — 7528.). As expected, the  $\rho$  value decreases with increasing sintered density of the samples. However, the TE figure of merit at high temperature remains low due to its large electrical resistivity which exhibits the value of approximately  $0.3 \, \Omega \, \text{m}$  at room temperature. Additionally, the low densification of the sample without adding PVA (58.92%) contributes further to the increment in electrical resistivity. In general, research into this material is focused on the reduction in electrical resistivity without adversely affecting  $S$  it

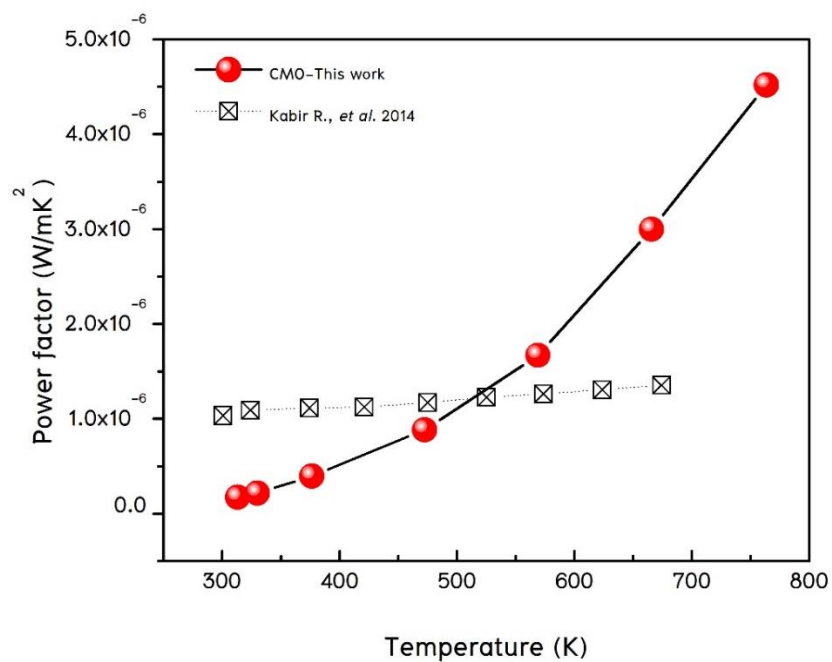
because a high resistivity results in a significant decrease in the power factor. The lowest  $\rho$  value  $\text{CaMnO}_3$  sample is  $0.597 \, \Omega \cdot \text{m}$  at 313 K to  $0.0179 \, \Omega \cdot \text{m}$  at 723 K, respectively.



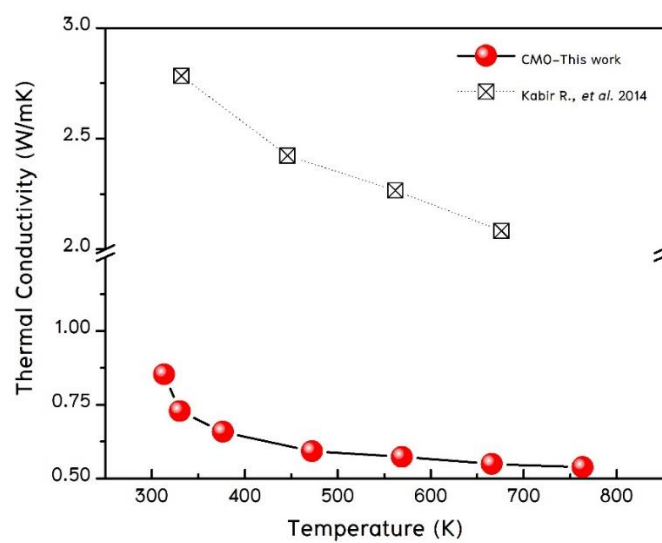
**Figure 4.5** Dependence of  $\rho$  on the temperature of the nanocrystalline  $\text{CaMnO}_3$  sample.

The temperature dependence on the power factor ( $PF = S^2 / \rho$ ) of  $\text{CaMnO}_3$  sample is shown in Figure 4.6. These samples show PF value characteristics with the values increased with increasing temperature. It is found that the highest PF value is  $1.75 \times 10^{-4} \, \text{W/mK}^2$  at 313 K, and it reached  $0.00452 \, \text{W/mK}^2$  at 723 K, which is attributed by its lowest resistivity. The highest PF value observed from these measurements greater than the corresponding value observed in the study by Thiel et al. (Thiel, P., et al., 2013, pp. 243707.) (i.e.  $2.5 \, \mu\text{W cm}^{-1} \text{K}^{-2}$  for undoped sample at 1170 K).





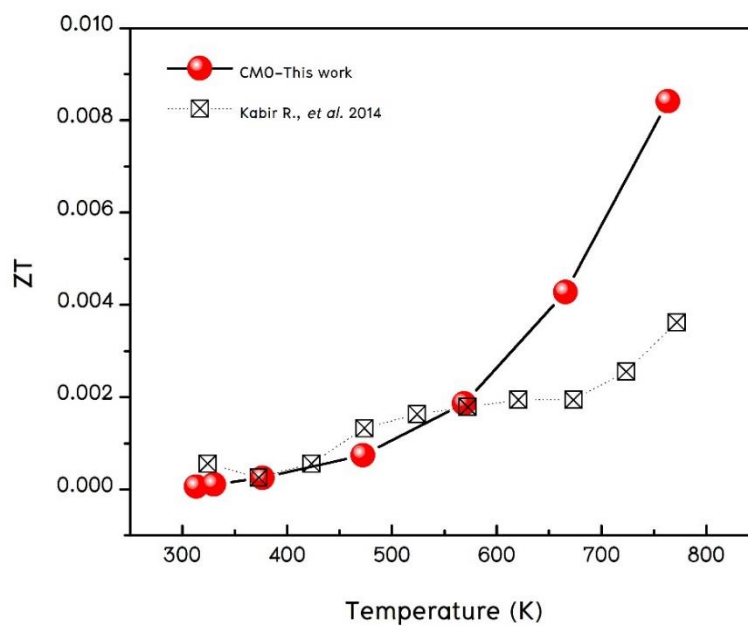
**Figure 4.6** Dependence of thermoelectric power factor  $\sigma S^2$  on the temperature of the nanocrystalline  $\text{CaMnO}_3$  sample.



**Figure. 4.7** Dependence of the  $\kappa$  on the temperature of the  $\text{CaMnO}_3$  sample was synthesized by fast sintering with hot-pressed method.

In addition to power factor, thermal conductivity is another fundamental parameter for the evaluation of performance of thermoelectric materials. In semiconductors, the thermal conductivity ( $\kappa$ ) is the sum of a phonon component ( $\kappa_{ph}$ ) and an electronic component ( $\kappa_e$ ) that can express as  $\kappa = \kappa_{ph} + \kappa_e$ . Phonon component is the dominant factor in total thermal conductivity for  $\text{CaMnO}_3$  system.  $\kappa_{ph}$  is proportional to  $1/T$  above Debye temperature, whereas  $\kappa_e$  is proportional to  $T / \rho$  ( $\rho$  : electrical resistivity). Figure. 4.7 the thermal conductivity of sample exhibited lower thermal conductivities over the whole temperature range that decreases when temperature increases from 0.85 W/mK at temperature 273 K was which became 0.53 W/mK at 773 K. It demonstrates that nanoparticles indeed reduce the thermal conductivity of  $\text{CaMnO}_3$  such reduction is associated with the enhanced phonon scattering by decreased size structured.

Dimensionless figure of merit  $ZT$  were calculated, as shown in Fig. 4.8. The maximum  $ZT$  value of  $\text{CaMnO}_3$  sample was observed at 923 K around 0.00842. The value of  $ZT$  increases with increasing the temperature, which is consistent with Kabir R., *et al.* (Kabir, R., *et al.*, 2014, pp. 7522 — 7528.).



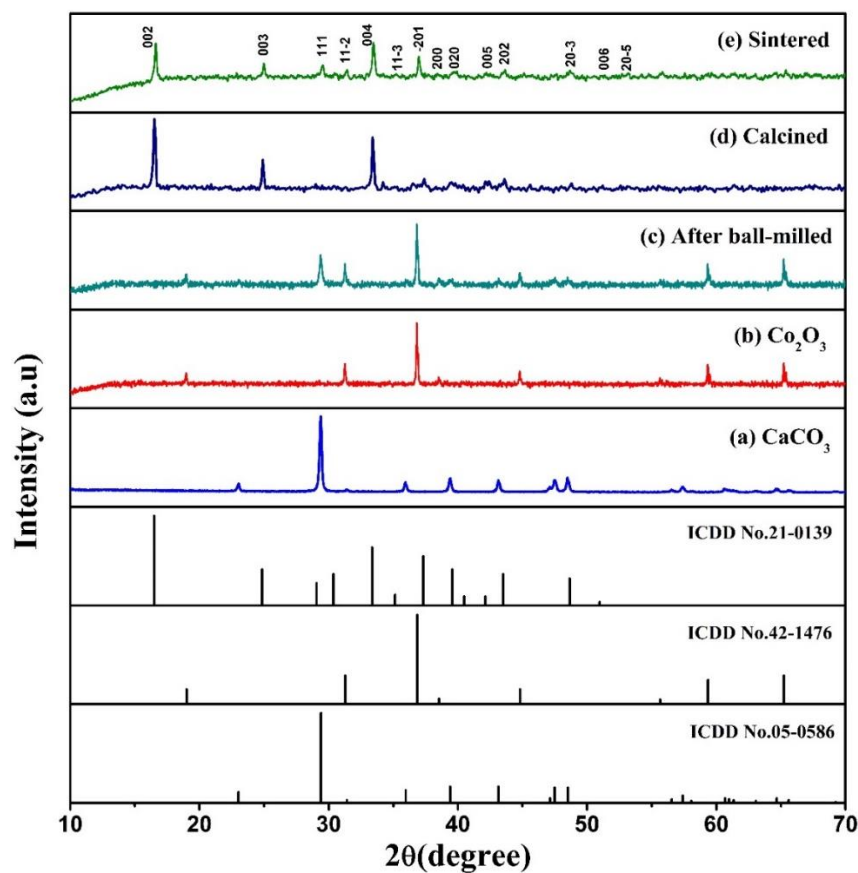
**Figure 4.8** Dimensionless figure of merit ( $ZT$ ) of the  $\text{CaMnO}_3$  sample.

## **p- $\text{Ca}_3\text{Co}_4\text{O}_9$ : Crystal Structure and Chemical Composition**

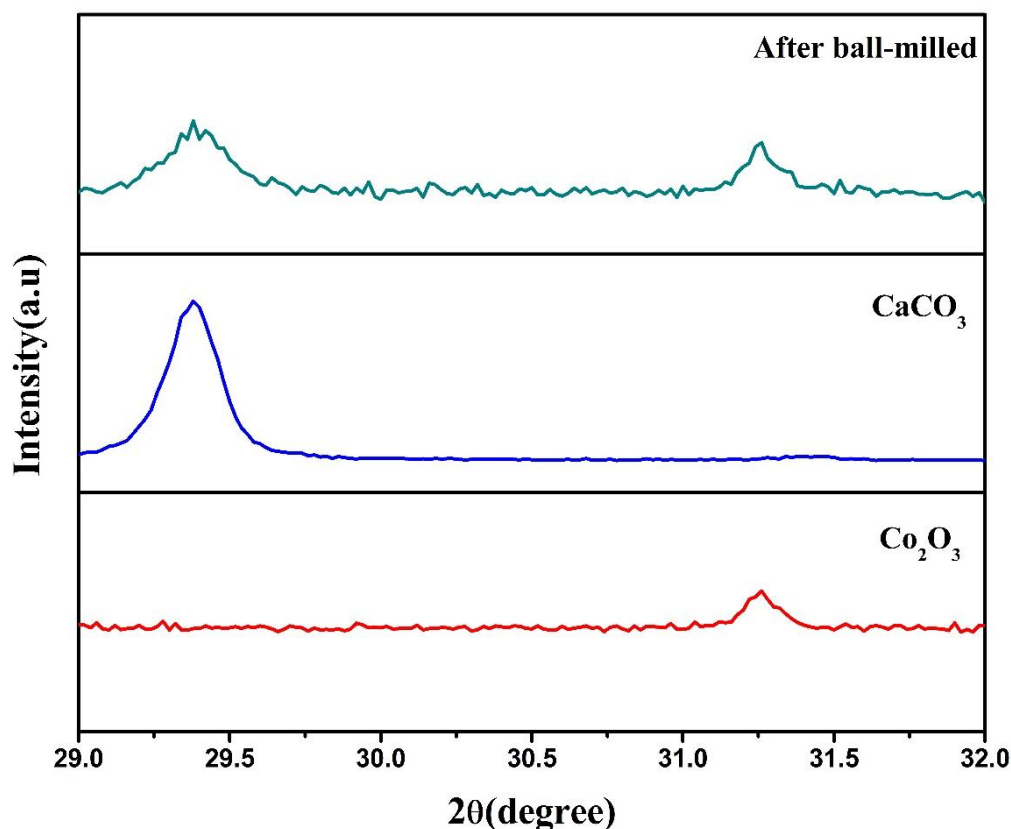
### **Synthesis $\text{Ca}_3\text{Co}_4\text{O}_9$ thermoelectric materials**

XRD patterns for the nano precursors, ball-milled powder, calcined powder, and sintered powder are shown in Figure. 4.9(a — e). The peaks in the XRD patterns indicated that (a) the  $\text{CaCO}_3$  and (b)  $\text{Co}_2\text{O}_3$  phase. The  $\text{CaCO}_3$  phases was showed broad peaks because the crystallite size is exceedingly small more than the  $\text{Co}_2\text{O}_3$  phases corresponding with Table 2. (c) the mixing treatment (8 h at 350 rpm in an agate ball mill) does not lead to the  $\text{Ca}_3\text{Co}_4\text{O}_9$  phase because they are composed of the combination inherent in both the  $\text{CaCO}_3$  and  $\text{Co}_2\text{O}_3$  peaks corresponds with N. Puri *et al.* (Puri, N., Tandon, R. P., & Mahapatro, A. K., 2018, pp. 6337–6342.). and indicates that the ball-milled process facilitates the formation of uniformly distributed mixture containing both the precursors. However, when we expanded image peaks in

range  $2\theta = 29 - 32^\circ$  shown in Figure. 4.10. the broad peaks of the mixed nano precursor powders after ball-milled 8 h and cause the crystallite size of mixed nano precursor powders become decreased with increasing ball mill time and influenced by the initial size of the precursors within the mixture correspond with N. Prasoetsopha *et al.* (Prasoetsopha, N., Pinitsoontorn, S., Kamwanna, T., Kurosaki, K., & Yamanaka, S., 2014, pp. 20635 – 20643.). Figure. 4.9d, the calcined powder was showed major crystal phase of the  $\text{Ca}_3\text{Co}_4\text{O}_9$  matched with the ICDD No.21-0139, the XRD patterns with the dominant (002) plane and expected ratio of the two highest intensity peaks for (002) and (004) planes (at  $16.5^\circ$  and  $33.6^\circ$ , respectively). While the peak at  $42.4^\circ$  found the minor diffraction peaks correspond to the presence of  $\text{Ca}_3\text{Co}_2\text{O}_6$  (ICDD No.23-0111) as intermediate phase become obvious in the sample due to the minor deviations in the stoichiometry and homogeneity were expected to facilitate the formation of secondary phases. This has been attributed to long hold durations during calcination or temperatures 1173 K, favoring the decomposition of the  $\text{Ca}_3\text{Co}_4\text{O}_9$  phase into the aforementioned phases. The diffraction signals of the calcined powders gradually narrowed and strengthened with increasing calcination temperatures, demonstrating the increase in crystallinity and crystallite size. and Figure. 4.9e From the data represented the single  $\text{Ca}_3\text{Co}_4\text{O}_9$  phase can be observed at 1173 K produce with the signature (002) plane at  $16.5^\circ$  indicated that the major diffraction peaks assigned for  $\text{Ca}_3\text{Co}_4\text{O}_9$  based phase of monoclinic structure and other planes at peak positions in accordance with ICDD No.21-0139, consisting of alternate stacking sub-systems with a two-dimensional triangular lattice of rock-salt-type  $[\text{Ca}_2\text{CoO}_3]$  layers sandwiched between two hexagonal  $[\text{CoO}_2]$  layers along c-axis corresponding with Masset, A.C., *et al.* (A.C Masset, *et al.*, 2000, pp. 166–175).



**Figure. 4.9** XRD patterns of the (a) precursors;  $\text{CaCO}_3$  nanoparticles, (b)  $\text{Co}_3\text{O}_4$  nanoparticles, (c) after ball-milled, (d)  $\text{Ca}_3\text{Co}_4\text{O}_9$  powders prepared by calcination and (e)  $\text{Ca}_3\text{Co}_4\text{O}_9$  powders prepared fast sintering by hot-press method. The vertical lines at the bottom axis represent various planes of  $\text{Co}_2\text{O}_3$ ,  $\text{CaCO}_3$ , and  $\text{Ca}_3\text{Co}_4\text{O}_9$  mentioned in ICDD No. 05-0586, 42-1476 and 21-0139, respectively.



**Figure 4.10** XRD patterns expanded image peaks in range  $2\theta = 29 - 32^\circ$ , the broad peaks of the mixed nano precursor powders after ball milled.

For ball-milled powder has agglomerate make the reduction of the size of the spheres after ball-milled, which tend to come together and form large aggregates. Calcined powder was the highest volume density because particle size was increased with increasing calcination temperatures. This could be due to the high surface energy of  $\text{Ca}_3\text{Co}_4\text{O}_9$  particles. At higher calcination temperatures, the surface energy of the particles tended to increase, resulting in increased aggregation. This consequently provided the larger particles. While sintered sample was lowest particle size due to the decreased amount of time to short sintering time (0.5 h). As evident from this figure, decreasing the sintering time reduces the particle size and volume density of sample.

The average crystallite size ( $D$ ) is calculated for the powder samples using the Scherrer's formula (Purushotham, E., & Krishna, N. G., 2013, pp. 973–976.) [Langford, J. I., & Wilson, A. J. C., 1978, pp. 102–113.). The estimated values for the average crystallite size of nano precursor powder, after ball-milled, calcined powder as shown in Table 4.3.  $\text{CaCO}_3$  and  $\text{Co}_2\text{O}_3$  have notice that the crystallite sizes obtained from XRD for ball milled sample is well below 6.90 nm, as observed clearly in the SEM images where the grain sizes are several nanometer as shown in Figure. 4.12(c). This observed decrease in crystallite size with increasing ball-milling time is attributed to the initial sizes of the precursor mixture experiencing calcination.

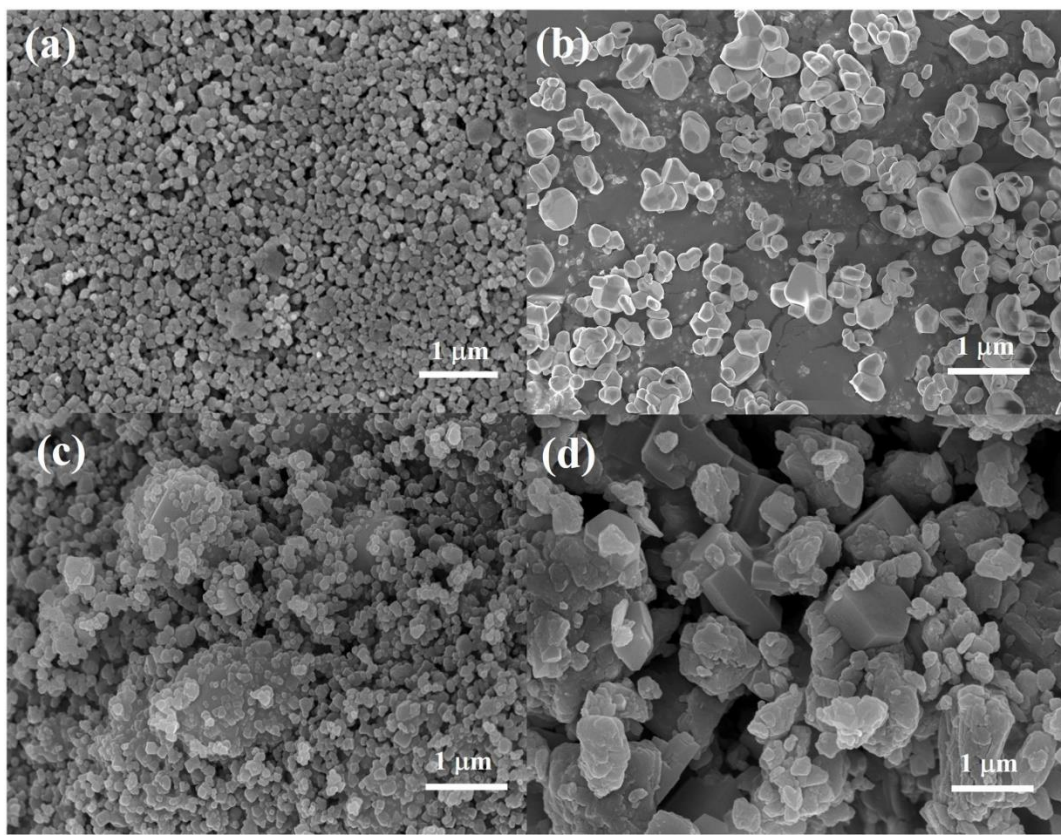
**Table 4.3** The average crystallite size ( $D$ ) determined by XRD of nano precursors powder, ball-milled, calcined samples, and grain size ( $d$ ) from SEM for sintered  $\text{Ca}_3\text{Co}_4\text{O}_9$  sample.

Samples	$2\theta$ (deg.)	FWHM (deg.)	$D$ (nm)	$d$ (nm)
$\text{CaCO}_3$	29.38	0.53	$19.45 \pm 0.1034$	—
$\text{Co}_2\text{O}_3$	36.82	0.34	$36.56 \pm 0.1342$	—
After ball-milled	36.82	1.32	$6.90 \pm 0.0024$	—
Calcined	16.5	0.55	$18.14 \pm 0.0131$	—
Sintered	16.5	0.55	$51.497 \pm 0.1819$	>100

## Microstructure Analysis

The nano precursors powder, after ball-milled, calcination, were confirmed particle sizes by SEM are shown in Figure. 4.11(a-d). shows representative micrographs of the two possible precursors:  $\text{CaCO}_3$  precursor is composed of particles size 89 nm rhombohedral crystal (Figure. 4.11a),  $\text{Co}_2\text{O}_3$  is composed of particles 393 nm octahedral crystals (Figure. 4.11b), respectively. Figure. 4.11c, shows image of the after ball-milled with irregular features average sizes of two populations  $\text{CaCO}_3$  and  $\text{Co}_2\text{O}_3$  which the reduction in feature sizes is monitored for the sample prepared with increasing ball-milled time and Figure. 4.11d observations confirm that the calcined powder contained the same plate as faceted rectangular shaped crystal grains. The size of the particle increases as calcination temperature increases. This resembles the inherent properties of lowering down the dimension using ball-milled and formation of larger features during calcination. The calcination temperatures 1173 K for 10 h, the grain size is relatively large, and the size distribution is uniform. The average grain size of calcined powder has two populations of  $\text{Ca}_3\text{Co}_4\text{O}_9$  particles seem to coexist: particles large particles, near 650 nm and exceedingly small particles, near 100 nm.

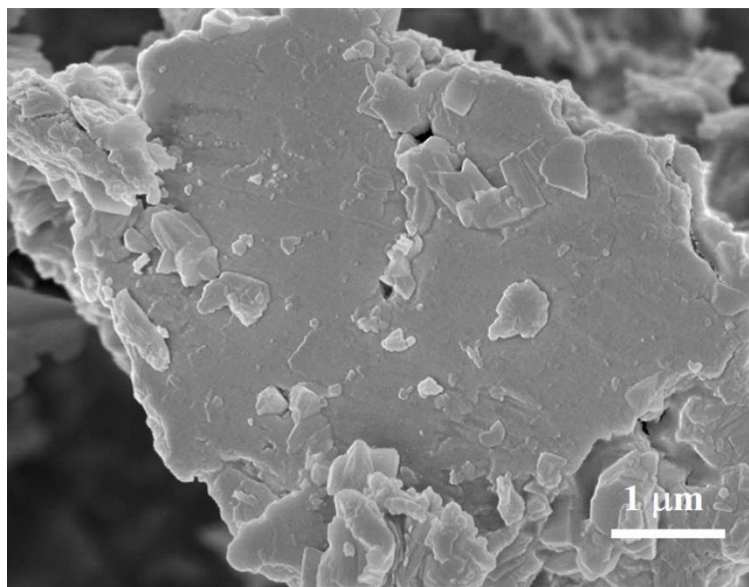




**Figure 4.11** SEM micrographs of the precursors, (a)  $\text{CaCO}_3$  nanoparticles, (b)  $\text{Co}_2\text{O}_3$  nanoparticles, and (c) ball-milled the mixed nano precursors powder after ball milling showing aggregates of nanoparticles (d) calcined powder.

The morphology of the sintered samples is shown in Figure. 4.12. After fast sintering, the grain size of  $\text{Ca}_3\text{Co}_4\text{O}_9$  is observed that grain does grow larger after sintering and exhibited a dense microstructure of lamellar grains in size and a strong texture perpendicular to the direction of the applied pressure level. The lamellar grains of  $\text{Ca}_3\text{Co}_4\text{O}_9$  have appeared to be large area, and such texture would be advantageous for thermoelectric performance since the thermoelectric properties of layered  $\text{Ca}_3\text{Co}_4\text{O}_9$  are highly anisotropic to cause of high Seebeck coefficient. The small grain around the lamellar grains was induced phonon scattering by point defects, leading to lower thermal conductivity. These authors have explained that this behavior

should be related to the reduction of grain boundaries number due to the improvement of grain alignment and the increase in bulk density corresponding to this work shows the high-density value of bulk  $\text{Ca}_3\text{Co}_4\text{O}_9$  sample.

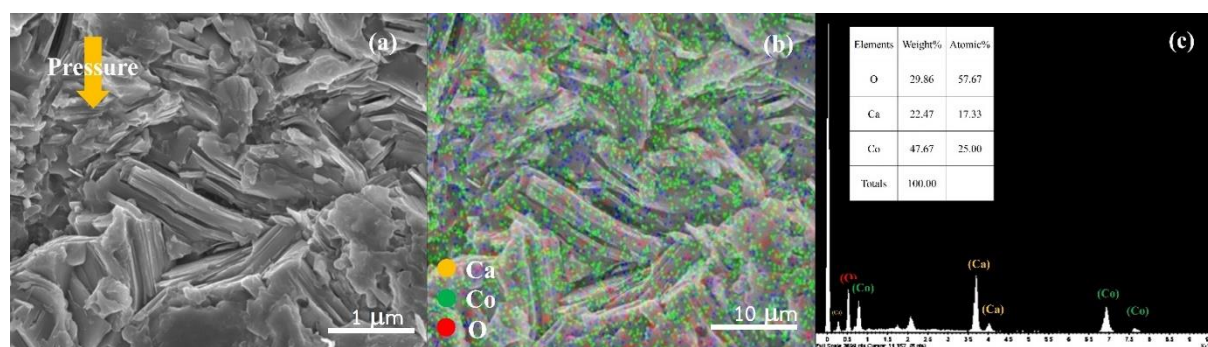


**Figure 4.12** SEM micrographs of the  $\text{Ca}_3\text{Co}_4\text{O}_9$  fast-sintering sample.

Moreover, the diffraction patterns of  $\text{Ca}_3\text{Co}_4\text{O}_9$  calcined and sintered sample were calculated the lattice parameter (a, b, c) the density, and theoretical density are given in Table 4.4. The lattice parameter is determined by XRD results. It has been reported that the lattice parameter increases or decreases as a function of the crystallite size in the structural and it can make a change in the properties of these materials (Dittrich, M., & Schumacher, G., 2014, pp. 27–33.) [Qi, W. H., & Wang, M. P., 2005, pp. 51–57.). Subsequently, the sintered sample present a high bulk density with an apparent density value larger than 94.87% of the theoretical density.

**Table 4.4** The density, theoretical density, and the lattice parameter ( $a$ ,  $b$ , and  $c$ ) of  $\text{Ca}_3\text{Co}_4\text{O}_9$  samples (Madre, M. A., *et al.*, 2013, pp. 1747–1754.)

Samples	Density ( $\text{g/cm}^3$ )	Theoretical Density %	Lattice Parameters ( $\text{\AA}$ )		
			$a$	$b$	$c$
Calcined	—	—	4.8752	4.5689	10.9032
Sintered	4.443 (4.68)	94.87	4.8680	4.5796	10.8753



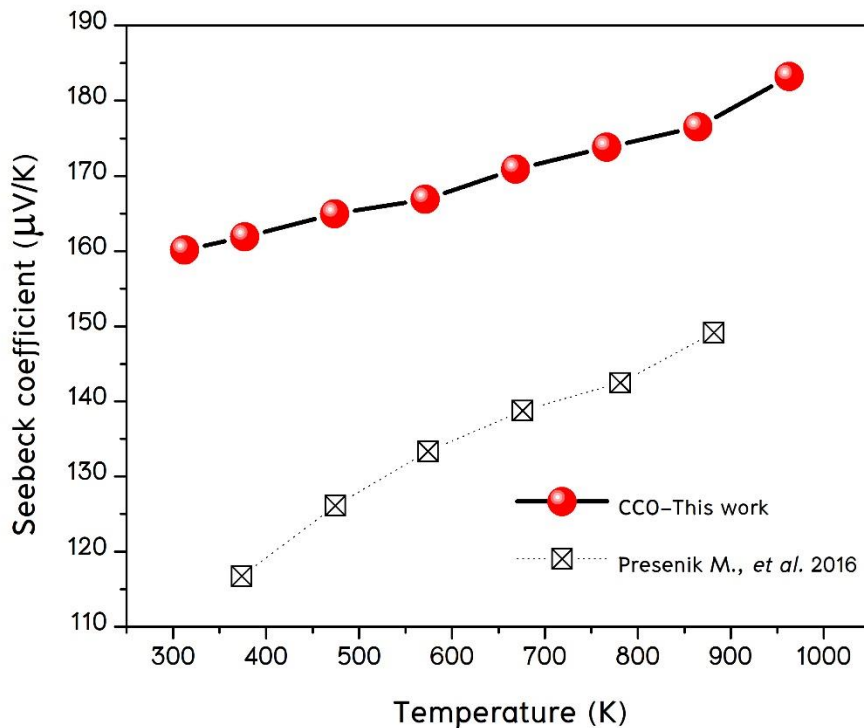
**Figure 4.13** (a) FE-SEM cross-sectional view of the fracture surface of the pellets, (b) images of the elemental compositional deviation (the colors indicate green (Co), orange (Ca), and red (O)), (c) EDX spectra of bulk  $\text{Ca}_3\text{Co}_4\text{O}_9$ .

The morphology of the  $\text{Ca}_3\text{Co}_4\text{O}_9$  powder and the EDX results are shown in Figure 4.13 (a–c). The powders (shown in Figure 6(a)) have irregular features 1  $\mu\text{m}$  in size. We clearly observe well-aligned large platelets homogeneously distributed and compactly stacked along the pressing axis. Indeed, at a hot pressure level of 20 MPa, the grains are converted to platelets, and their lateral size increases to approximately 10  $\mu\text{m}$ . Thus, much of the porosity is removed, which significantly improves the bulk density. As shown in Figure 4.13(b), the change in the elemental composition of CCO–349 after hot pressing was determined at randomly selected points on the surface. The elements in CCO–349 after hot pressing were not evenly distributed. As shown in Figure 4.13(c), the contents of Ca, Co and O were determined by EDX spectroscopy. EDX cannot quantify light elements such as oxygen. The ratio of Ca to Co was determined to be Ca:Co= 0.67:1.90.

### **p- $\text{Ca}_3\text{Co}_4\text{O}_9$ : Thermoelectric properties**

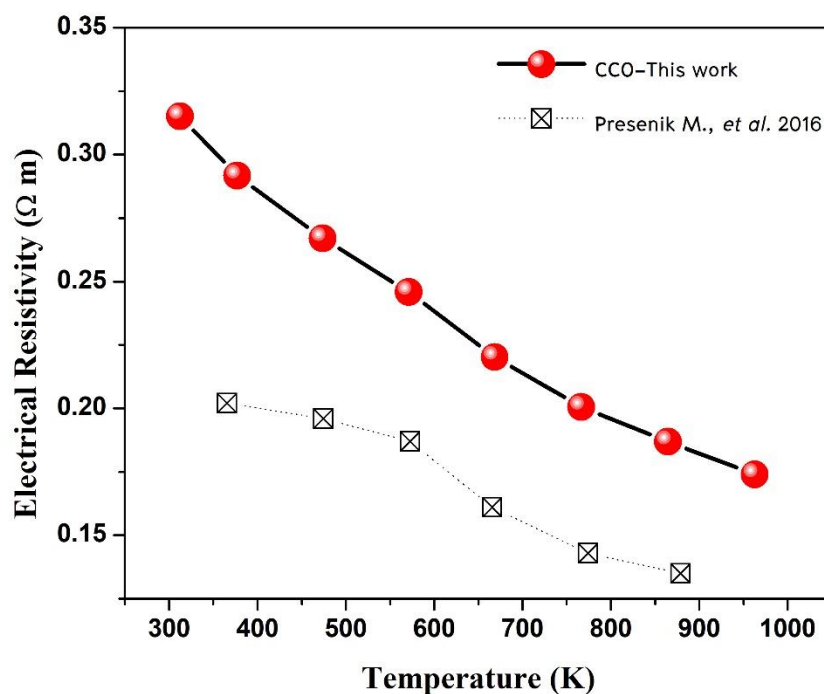
Temperature dependence of the Seebeck coefficient ( $S$ ) of  $\text{Ca}_3\text{Co}_4\text{O}_9$  sample compared with samples synthesized by hot-pressed sintering results from literature data (Presečnik, M., De Boor, J., & Bernik, S., 2016, pp. 7315–7327.) as shown in Figure. 4.14 Seebeck coefficient of all samples shows a positive value over the measured temperature range, indicating p-type conduction that the charge transport is dominated by defect electrons corresponding with the results samples HP. The  $S$  value of  $\text{Ca}_3\text{Co}_4\text{O}_9$  sample showed that it increased with increasing temperature from 160.15  $\mu\text{V/K}$  at 400 K, to 185  $\mu\text{V/K}$  at 973 K approximately. After calcination and fast sintering by hot-pressed method, the XRD pattern have shown the single phase and the grain size still micrometer which the two populations particles seem to coexist with

lamellar grains, and small grains that occur around observed from SEM images. The small grains occur around the lamellar grains have makes high mobility and low phonon transport properties make a high Seebeck coefficient. In addition,  $\text{Ca}_3\text{Co}_4\text{O}_9$  sample sintered by hot-pressing has lower  $S$  values more than another sample because this method is the capability to compact the powder into a dense bulk within long times owing to the self-heat effect makes a well densified with micrometer of grain size increasing the influence on the  $S$  values of the scattering effect will be decreased. Therefore, when the length of grains is larger, the influence of temperature on the  $S$  values become more significant. These values are extremely high and agree with the high thermal conductivity values.



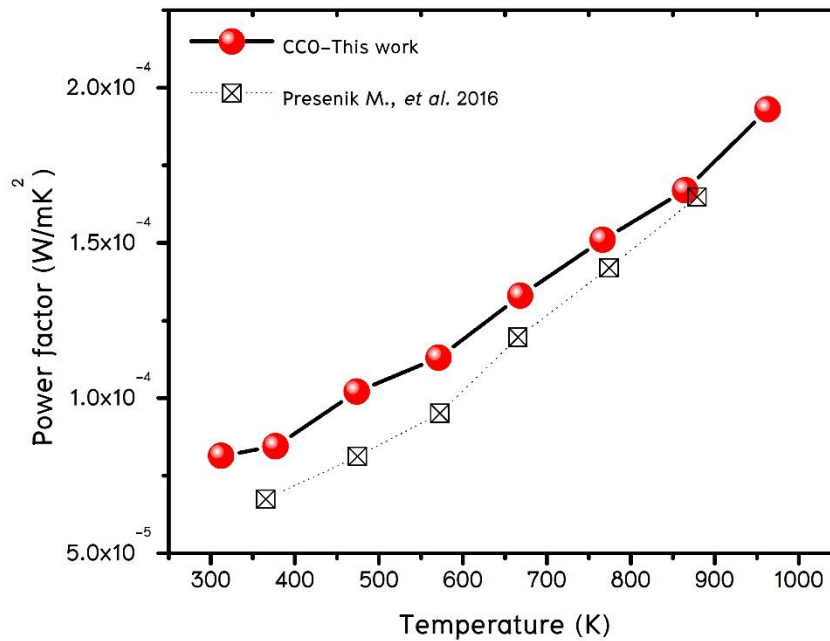
**Figure 4.14** Dependence of the  $S$  on the temperature of the  $\text{Ca}_3\text{Co}_4\text{O}_9$  sample was synthesized by fast sintering with hot-pressed method.

Figure 4.15. The  $\rho$  curves of the  $\text{Ca}_3\text{Co}_4\text{O}_9$  samples had similar behavior corresponding to metal to semiconducting transition in the range 273 — 973 K. The  $\rho$  of sample was decreased with increasing temperature, i.e.  $0.32 \, \Omega \, \text{m}$  at 300 K to  $0.17 \, \Omega \, \text{m}$  at 973 K which corresponded with literature data. The monoclinic structure of  $\text{Ca}_3\text{Co}_4\text{O}_9$  is comprised of two misfit layered subsystems: a distorted rock salt-type  $\text{Ca}_2\text{CoO}_3$  layer sandwiched between two  $\text{CdI}_2$ -type  $\text{CoO}_2$  layers along the  $c$ -axis.  $\text{CoO}_2$  nanosheets possessing a strongly correlated electron system serve as electronic transport layers (i.e., high electrical conductivity) and  $\text{Ca}_2\text{CoO}_3$  misfit layers serve as phonon scattering regions resulting in low thermal conductivity.



**Figure 4.15** Dependence of the  $\rho$  on the temperature of the  $\text{Ca}_3\text{Co}_4\text{O}_9$  sample was synthesized by fast sintering with hot-pressed method.

The temperature dependence on the power factor ( $PF = S^2 / \rho$ ) of  $\text{Ca}_3\text{Co}_4\text{O}_9$  sample is shown in Figure. 4.16. The PF value characteristics with the values increased with increasing temperature corresponding with Presečnik, M. *et al.* The calculated PF value of  $\text{Ca}_3\text{Co}_4\text{O}_9$  sample is  $0.08 \text{ mW/mK}^2$  at 300 K, and it reached  $0.19 \text{ mW/mK}^2$  at 973 K. When compared with literature from Sotelo *et al.* (Sotelo, A., *et al.*, 2015, pp. 247–254.), they have synthesized a nanometric grain size from the classical solid-state route. The result shows the similarity in values with this work.

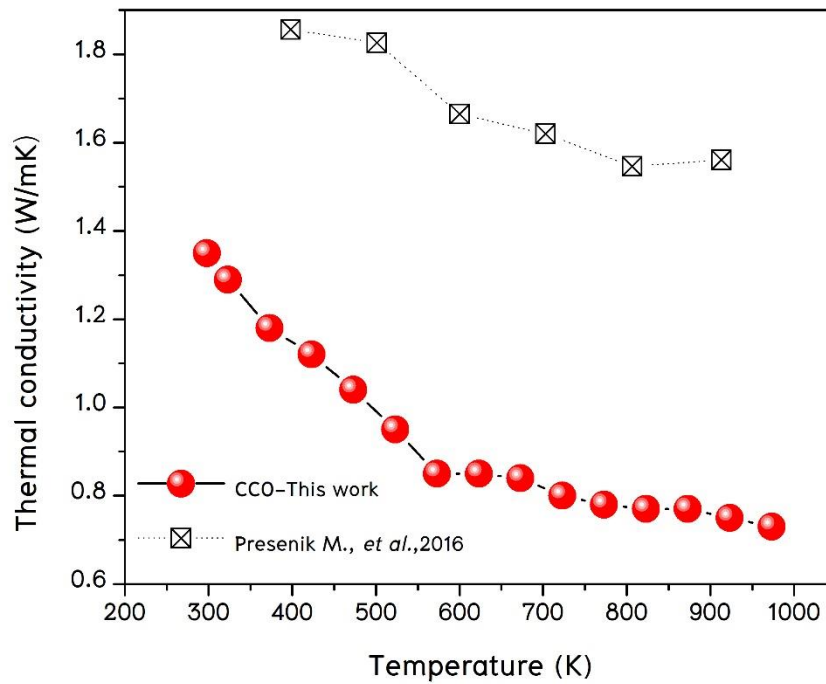


**Figure 4.16** Temperature dependence of the power factor of the  $\text{Ca}_3\text{Co}_4\text{O}_9$  sample.

Figure 4.17 the thermal conductivity sample exhibited lower thermal conductivities over the whole temperature range that decreases when temperature increases from  $1.35 \text{ W/mK}$  at temperature 273 K which became  $0.73 \text{ W/mK}$  at

973 K. The  $\kappa$  values of  $\text{Ca}_3\text{Co}_4\text{O}_9$  sample are also lower when compared with other well-known oxide ceramics (Presečnik, M., *et al.*, 2016, pp. 7315–7327.). It is evident that the lower thermal conductivity values were caused by the  $\text{Ca}_3\text{Co}_4\text{O}_9$  sample that was synthesized from nano powder precursors and the fast sintering with the hot-pressed method was highly densified, the influence of porosity on thermal transport properties can be neglected (Combe, E., Funahashi, R., Barbier, T., Azough, F., & Freer, R., 2016, pp. 1296–1305.) and nanoscale have interfaces, which could create additional phonon scattering. Therefore, it is evident that the lower  $\kappa$  values were caused by the enhancement of phonon scattering due to the fine microstructure. The thermal conductivity is dominated by phonon vibrations when the semiconductor material has a low carrier concentration. However, it is dominated by the concentration of the carriers when the carrier concentration increases. Therefore, the decrease in thermal conductivity observed for samples synthesized from nano-sized precursors, must be related to the decrease of the lattice component of the thermal conductivity  $\kappa_l$ . This decrease must be attributed to an increase in the phonon scattering. This scattering could be related to the smaller size of the  $\text{Ca}_3\text{Co}_4\text{O}_9$  particles: indeed, the average particle size of the samples synthesized from nano-sized precursors.

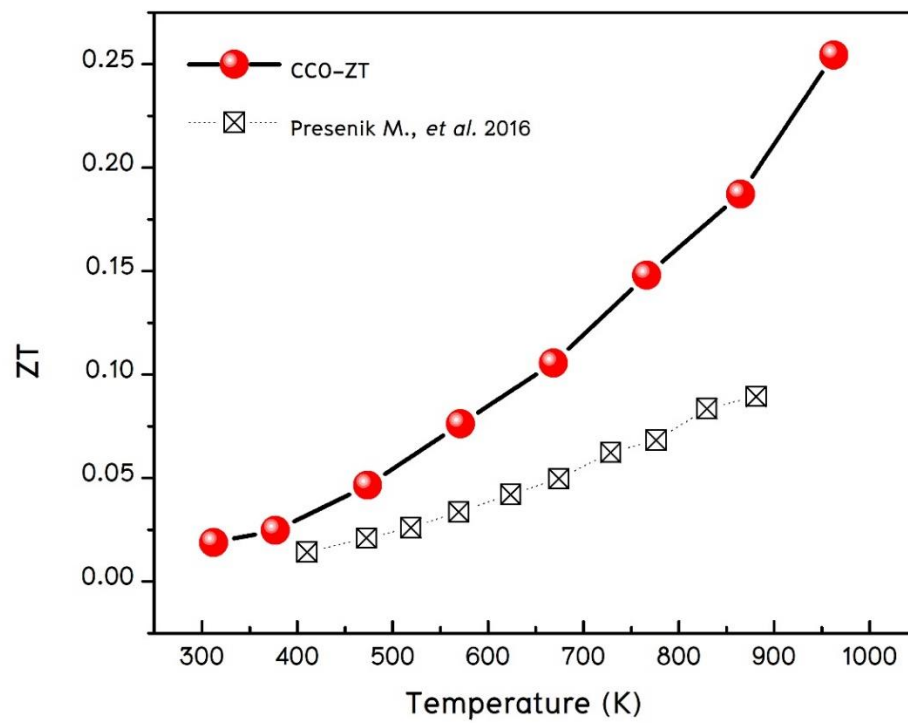




**Figure 4.17** Dependence of the  $\kappa$  on the temperature of on the temperature of the  $\text{Ca}_3\text{Co}_4\text{O}_9$  sample was synthesized by fast sintering with hot-pressed method.

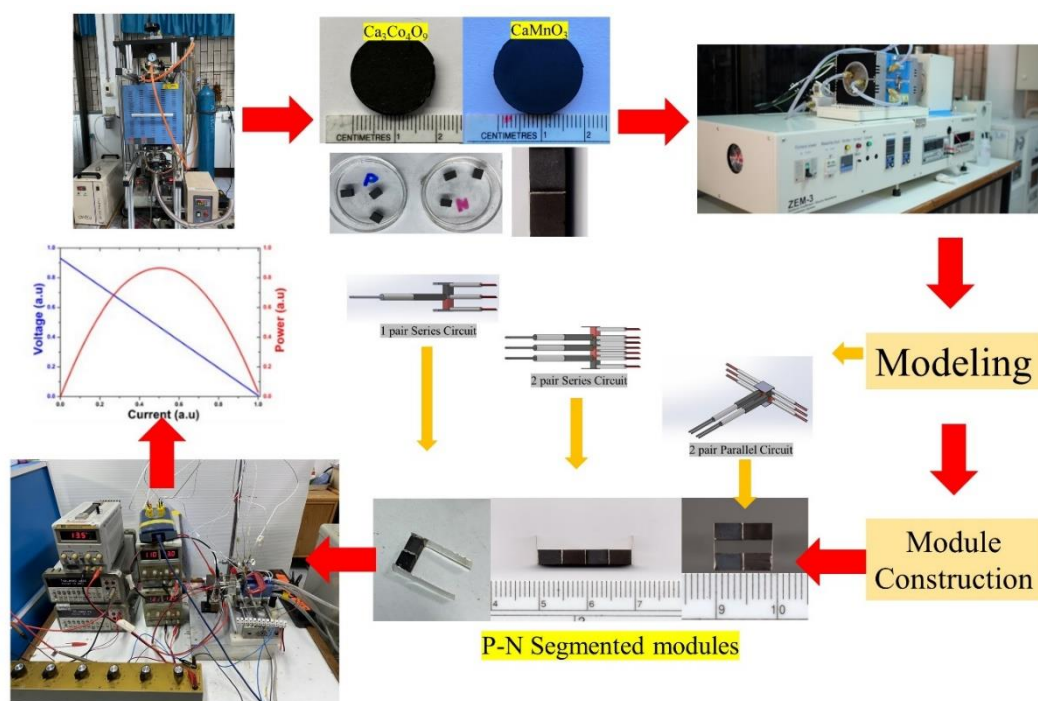
Dimensionless figure of merit  $ZT$  were calculated, as shown in Figure. 4.18. The maximum  $ZT$  value of  $\text{Ca}_3\text{Co}_4\text{O}_9$  sample was observed at 923 K around 0.25 when compared with other methods from literature data. Which is an exceptionally large value among oxide materials for undoping materials. The thermoelectric efficiency of this system is effectively improved by nano structuring due to results show, the enhanced  $ZT$  was increased with increasing temperature due to the lower electrical resistivity and significantly lower thermal conductivity in our sample due to the method for synthesizing nanoscale powders and sintering the nano powder with the short durations times for decreased the significant grain growth. Further optimization of the synthesis process such as shorter period at high temperature

should lead to even smaller  $\text{Ca}_3\text{Co}_4\text{O}_9$  particles which would in turn decrease thermal conductivity and thus lead to better  $ZT$  values.



**Figure 4.18** Dimensionless figure of merit ( $ZT$ ) of the  $\text{Ca}_3\text{Co}_4\text{O}_9$  sample.

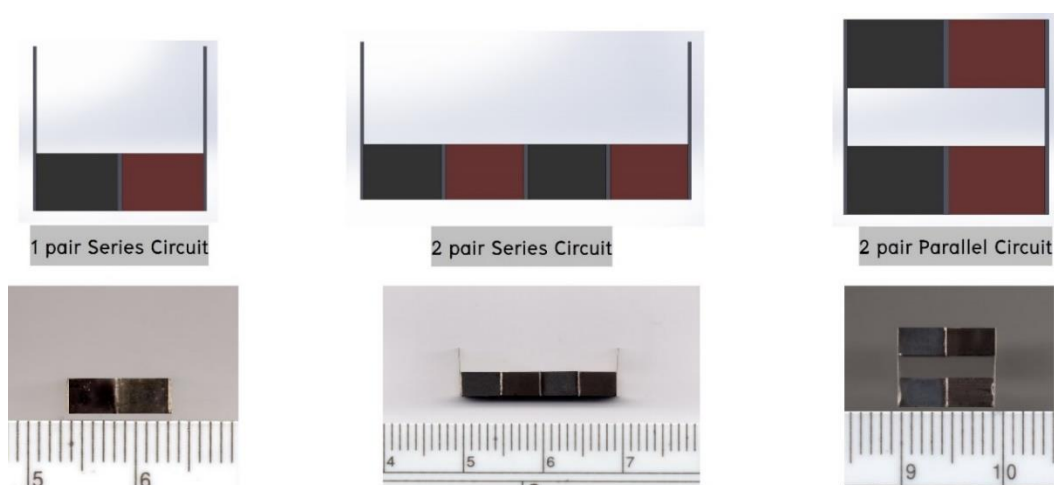
## Thermoelectric multilayers generator fabrication of n- $\text{CaMnO}_3$ and p- $\text{Ca}_3\text{Co}_4\text{O}_9$



**Figure 4.19** Schematic of the whole thermoelectric segmented module construction process from sintering and characterized materials to modelling for measurements, built-up and test modules.

For the fabrication of segmented legs, the obtained pellets of CCO and CMO were cut into rectangular pieces with desired dimensions  $3.5 \times 3.5 \times 5 \text{ mm}^3$ . Before the joining step, it is crucial that the surface to be joined is prepared and cleaned. First, the joining pieces were polished to remove residues from the previous cutting process. The polishing also provides adequate surface flatness to proceed joining. Then, the polished pieces were cleaned by ultrasonication for 3 minutes in solutions of acetone.

100  $\mu\text{m}$  thick Ag sheet with a purity of 99.99% was used to make electrodes and joining material between the CMO and the CCO. The brazing and soldering method where bonding is made by the melting of a third material inserted between the pieces needed to be joined. Brazing joining process was conducted in air using the silver paste at 1 mm thickness. After joining the oxide legs and Ag sheets, the joint was dried at 423 K for 10–15 min and then firing up at 1023 K for 10 min to establish good electrical contact between the metal electrodes and semiconducting oxides. 1 pair, 2 pairs with series circuit and 2 pairs with parallel circuit of thermoelectric multilayers devices were designed by solid works program as shown in Figure. 4.20 (a), (b), and (c), respectively.

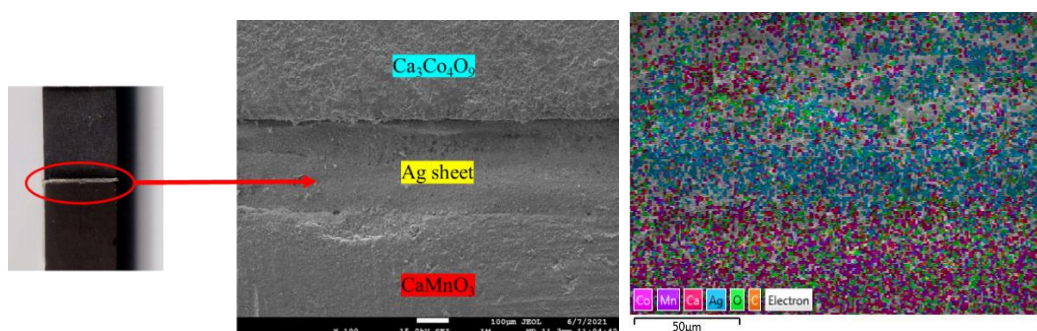


**Figure 4.20** Thermoelectric multilayers devices of (a) 1 pair designed and real fabrication, (b) 2 pairs series circuit and real fabrication, and (c) 2 pairs parallel circuit and real fabrication

## Microstructure Analysis

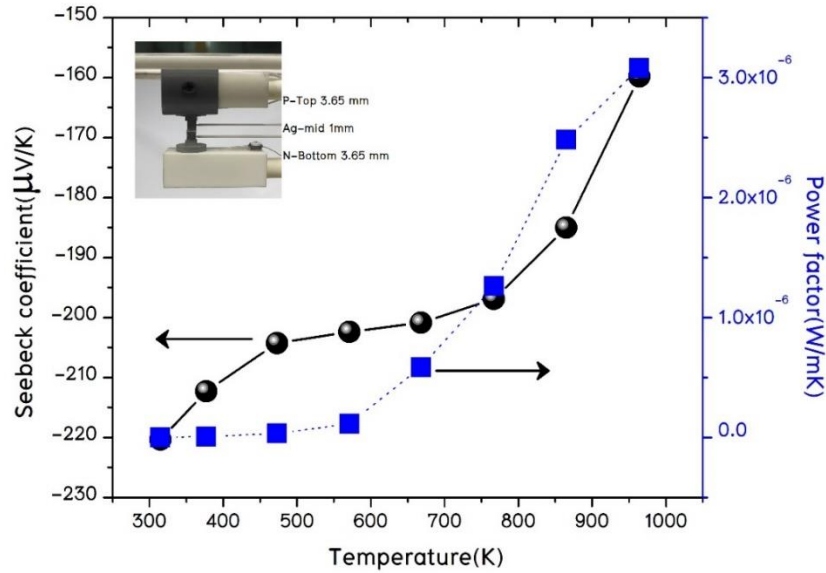
When CCO, Ag sheet, and CMO compounds were combined to form the CCO/Ag/CMO segmented ceramic as shown in Figure. 4.21(a), CCO and CMO layers were found to retain their respective phases as confirmed by the XRD patterns in Figure. 4.21(b) for CCO layer and Figure. 4.21(c) for CMO layer. This suggested that the fabrication process of CCO/CMO segmented ceramic used in this study did not affect the phase characteristics of the corresponding individual compound. Moreover, the absence of secondary phase for each side indicated an obvious separation between CCO and CMO layers. The phase formation at the interface area between CCO, Ag sheet, and CMO layers of the segmented ceramic was further investigated by field emission scanning electron microscopy. Figure. 4.21(a) shows a backscattered electron image of the CCO/CMO segmented ceramic. It could be seen that CCO and CMO layers corresponded to top and bottom areas, respectively. The interfacial area between CCO and CMO layers could be observed clearly but the boundary was sharp due to Ag sheet block the diffusion reaction between the two compounds. The compositional variation of CCO/ Ag/ CMO and interfacial boundary regions was studied using energy dispersive X-ray spectrometry (EDX). The quantitative data of composition for each side were plotted in Figure. 4.21(b). As seen in the CCO area (i.e., red color bar), the layer was mainly composed of calcium (Ca), cobalt (Co), carbon (C) and oxygen (O). Meanwhile, calcium (Ca), manganese (Mn) and oxygen (O) was observed prominently in the CMO layer (i.e., blue color bar). Interestingly, all elements could be detected at the CCO/ Ag/ CMO interface (i.e., black color bar). In addition, EDX analysis at the interfacial region revealed that there is no reaction or significant diffusion layer due to the Ag sheet was used to make electrodes. These

observations may explain for the lower measured interfacial contact resistance than that reported in (Holgate, T. C., *et al.*, 2014, pp. 827–833.) with  $\text{Fe}_{22}\text{Cr}$  electrode.



**Figure 4.21** (a) A proven picture of segmented CCO/CMO legs were successfully joined by silver brazing method and (b) elemental mapping of CCO/Ag/CMO ceramic.

## Thermoelectric properties of multilayer thermoelectric modules



**Figure 4.22** Temperature dependence of the Seebeck coefficient and power factor of n-CaMnO<sub>3</sub> and p-Ca<sub>3</sub>Co<sub>4</sub>O<sub>9</sub> 1 pair module fabrication.

### POWER GENERATION CHARACTERISTICS OF THE MODULES

The power generation of module is unexpected in a realistic working condition there are many factors which affect the output power of modules such as heat losses, contact resistances, heat transfer, etc. To demonstrate the influence of segmentation in TEG, two type of 1 couple, 2 pairs couple modules (n-CaMnO<sub>3</sub> and p-Ca<sub>3</sub>Co<sub>4</sub>O<sub>9</sub>) as was prepared with different circuit, tested, and compared. To understand the sources that influence the obtained experimental results, The relationship between the open-circuit voltage  $V_{OC}$  and the Seebeck coefficients of the TE materials forming the module can be then expressed as (Rowe, D. M. (Ed.), 2018):

$$V_{OC} = n \int_{T_c}^{T_h} \{ \alpha_p(T) - \alpha_n(T) \} dT \quad (35)$$

where  $T_h$  and  $T_c$  are the hot and the cold side temperatures,  $n$  is the number of p–n couples,  $\alpha_p$  and  $\alpha_n$  are the Seebeck coefficients of p– and n–type legs, respectively. One should note that, the thermocouples used to measure the temperature were placed on surface of Ag electrodes and their thermal contact resistance was assumed to be small. Therefore, the  $V_{OC}$  values measured are well reflecting the actual temperature span across the TE legs. As for the multilayer modules, formula can be rewritten as:

$$V_{OC} = n \int_{T_m}^{T_h} \{ \alpha_{CCO}(T) dT - \alpha_n(T) \} dT \quad (36)$$

Where  $T_m$  is the temperature at the connection junction. The  $T_m$  can be determined by the continuity of the heat flux at the junction, which yields (Apertet, Y., *et al.*, 2015, pp. 160–165.) [Apertet, Y., Ouerdane, H., Goupil, C., & Lecoœur, P., 2016, pp.1–8.):

$$\kappa_{CCO}(T_h - T_m) + \alpha_{CCO}TI = \kappa_{CMO}(T_m - T_c) + \alpha_{CMO}TI \quad (37)$$

In case of the open circuit voltage the  $T_m$  can be obtained by:

$$T_m = \frac{\kappa_{CCO}T_h + \kappa_{CMO}T_c}{\kappa_{CCO} + \kappa_{CMO}} \quad (38)$$

The magnitude of the output current,  $I$ , is proportional to the sum of the internal resistances of the module  $R_{int}$  and the external resistive load  $R_{load}$  and it is given by

$$I = \frac{V_{OC}}{R_{int} + R_{load}} \quad (39)$$

where  $R_{int} = R_{legs}R_c$  is the sum of the resistances of the p–n legs without metal electrodes  $R_{legs}$  and the total contact resistance  $R_c$ , which includes the contact



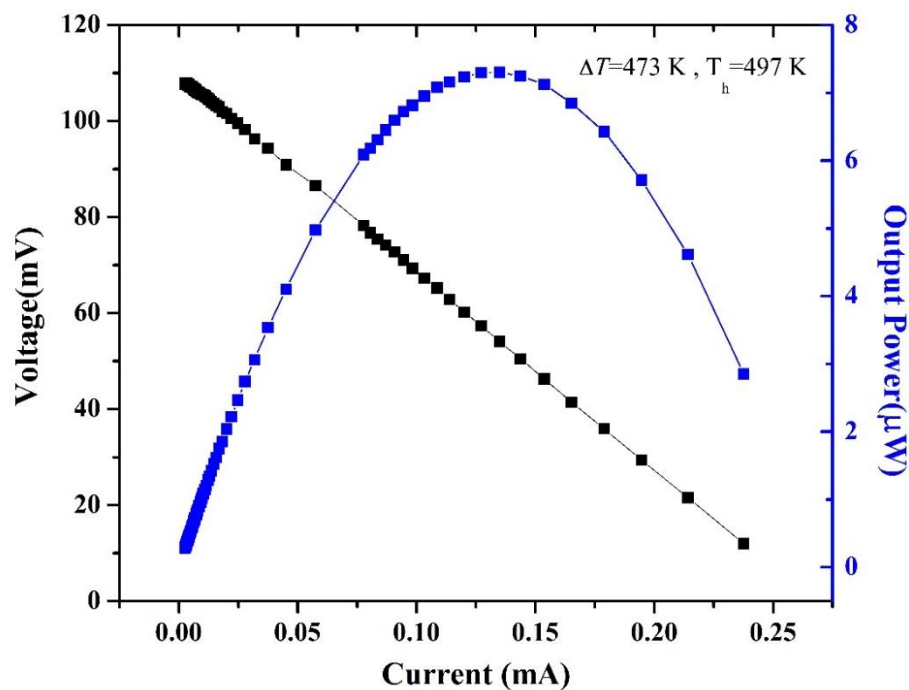
resistances at the joining part of segmented leg, the hot-side junction, and the cold-side junction. The power output of the module as a function of  $V_{OC}$  and the total resistance is given by

$$P = I^2 R_{load} = V_{OC}^2 \left[ \frac{R_{load}}{(R_{int} + R_{load})^2} \right] \quad (40)$$

It is clear from Eq. (40) that the power output of the module is dependent on the Seebeck coefficient, the internal resistance, and the external load resistance. The maximum power output ( $P_{max}$ ) occurs when the external load resistance is equal to the internal resistance. To generate a thermoelectric module at its maximum power output, the load resistance needs to be continuously adjusted to match the internal module resistance.

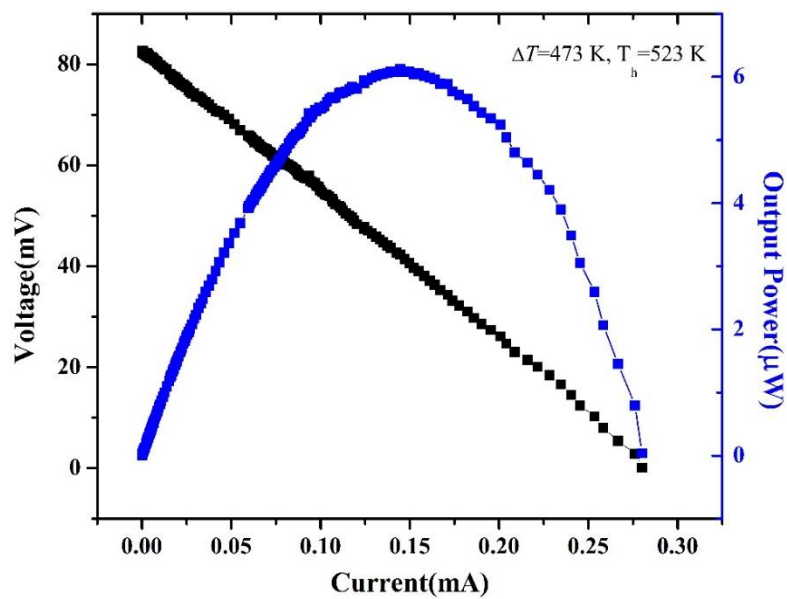
$$P_{max} = \frac{V_{oc}^2}{4R_{int}} \quad (41)$$

This resistance can vary greatly with temperature due to the temperature dependences of the resistivity of the TE materials itself as well as the temperature dependence of the total contact resistances. It is obvious that the smaller the internal resistance, the higher the maximum output power can be obtained.



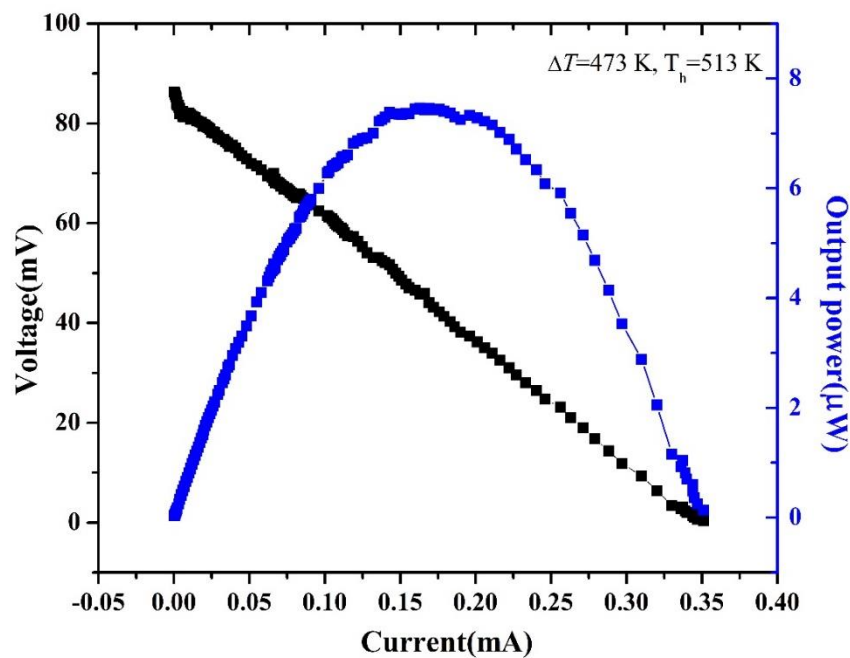
**Figure 4.23** The V–I and P–I curves of 1 pair thermoelectric multilayer module as a function of  $\Delta T = 473$  K at  $T_h = 497$  K and  $T_c = 297$  K.

Figure. 4.23 shows the power generation characteristics of modules at various applied temperature gradients. As expected, 1 pair, the voltage–current  $V(I)$  and output power current  $P(I)$  show the same tendency of increasing value as the temperature increases. At the highest applied temperature difference ( $T_h/T_c = 497$  K/ $\sim 297$  K),  $\Delta T \approx 473$  K, the measured open circuit voltage ( $V_{OC}$ ) of the 1 pair module was found to be 82.14 mV, and the voltage decreased linearly with increasing current. The measured maximum output power reached a value of 7.30  $\mu$ W at a current of 0.14 mA and matching resistances load 100 k $\Omega$ .



**Figure 4.24** The V-I and P-I curves of 2 pair thermoelectric multilayer as  $\Delta T = 473$  K at  $T_h = 523$  K and  $T_c = 323$  K.

Figure 4.24 shows 2 pair connected by a series circuit, the voltage-current  $V(I)$  and output power current  $P(I)$  show the same tendency of increasing value as the temperature increases. At the highest applied temperature difference ( $T_h / T_c = 523$  K/ $\sim 323$  K),  $\Delta T \approx 473$  K, the measured open circuit voltage ( $V_{OC}$ ) of the 2 pair module was found to be 82.27 mV, and the voltage decreased linearly with increasing current. The measured maximum output power reached a value of 6.12  $\mu$ W at a current of 0.15 mA and matching resistances load 100 k $\Omega$ .



**Figure 4.25** The V-I and P-I curves of 2 pair thermoelectric module as  $\Delta T = 473$  K at  $T_h = 513$  K and  $T_c = 313$  K.

For figure. 4.25 the results of 2 pair connected by a parallel circuit, the voltage-current  $V(I)$  and output power current  $P(I)$  show the same tendency of increasing value as the temperature increases. At the highest applied temperature difference ( $T_h/T_c = 513 \text{ K}/\sim 313 \text{ K}$ ),  $\Delta T \approx 473 \text{ K}$ , the measured open circuit voltage ( $V_{OC}$ ) of the 2 pair module was found to be 100.59 mV, and the voltage decreased linearly with increasing current. The measured maximum output power reached a value of  $7.46 \mu\text{W}$  at a current of 0.16 mA and matching resistances load  $100 \text{ k}\Omega$ .

## References

- A.C Masset, C. Michel, A. Maignan, M. Hervieu, O. Toulemonde, F. Studer, J. Hejtmanek, Phys. Rev. B. 62[1], 166–175 (2000).
- Apertet, Y., Ouerdane, H., Goupil, C., & Lecoœur, P. (2015). Equivalent parameters for series thermoelectrics. *Energy Conversion and Management*, 93, 160–165.
- Apertet, Y., Ouerdane, H., Goupil, C., & Lecoœur, P. (2016). A note on the electrochemical nature of the thermoelectric power. *The European Physical Journal Plus*, 131(4), 1–8.
- Bocher, L.; Aguirre, M. H.; Logvinovich, D.; Shkabko, A.; Robert, R.; Trottmann, M.; Weidenkaff, A.  $\text{CaMn}_{1-x}\text{Nb}_x\text{O}_3$  ( $x \leq 0.08$ ) perovskite-type phases as promising new high-temperature n-type thermoelectric materials. *Inorg. Chem.* 2008, 47(18), 8077 – 8085.
- Combe, E., Funahashi, R., Barbier, T., Azough, F., & Freer, R. (2016). Decreased thermal conductivity in  $\text{Bi}_2\text{Sr}_2\text{Co}_2\text{O}_{10}$  bulk materials prepared by partial melting. *Journal of Materials Research*, 31(9), 1296–1305.
- Cutler M, Leavy JF, Fitzpatrick RL. Electronic transport in semimetallic cerium sulfide. Phys Rev. 1964;133(4A) : A1143–52.
- Dittrich, M.; Schumacher, G. Evolution of crystallite size, lattice parameter and internal strain in Al precipitates during high energy ball milling of partly amorphous  $\text{Al}_{87}\text{Ni}_8\text{La}_5$  alloy. *Mater. Sci. Eng.: A*. 2014, 604, 27–33.

- Ferreira, N. M.; Neves, N. R.; Ferro, M. C.; Torres, M. A.; Madre, M. A.; Costa, F. M.; Kovalevsky, A. V. Growth rate effects on the thermoelectric performance of  $\text{CaMnO}_3$ -based ceramics. *J. Eur. Ceram. Soc.* 2019, **39**(14), 4184 – 4188.
- Flahaut, D.; Mihara, T.; Funahashi, R.; Nabeshima, N.; Lee, K.; Ohta, H.; Koumoto, K. Thermoelectrical properties of A-site substituted  $\text{Ca}_{1-x}\text{Re}_x\text{MnO}_3$  system. *J. Appl. Phys.* 2006, **100**(8), 084911.
- Holgate, T. C., Han, L., Wu, N., Bøjesen, E. D., Christensen, M., Iversen, B. B., ... & Pryds, N. (2014). Characterization of the interface between an Fe–Cr alloy and the p-type thermoelectric oxide  $\text{Ca}_3\text{Co}_4\text{O}_9$ . *Journal of alloys and compounds*, **582**, 827–833.
- Kabir, R.; Zhang, T.; Wang, D.; Donelson, R.; Tian, R.; Tan, T. T.; Li, S. Improvement in the thermoelectric properties of  $\text{CaMnO}_3$  perovskites by W doping. *J. Mater. Sci.* 2014, **49**(21), 7522 – 7528.
- Langford, J. I., & Wilson, A. J. C. (1978). Scherrer after sixty years: a survey and some new results in the determination of crystallite size. *Journal of applied crystallography*, **11**(2), 102–113.
- Madre, M. A., Costa, F. M., Ferreira, N. M., Sotelo, A., Torres, M. A., Constantinescu, G., ... & Diez, J. C. (2013). Preparation of high-performance  $\text{Ca}_3\text{Co}_4\text{O}_9$  thermoelectric ceramics produced by a new two-step method. *Journal of the European Ceramic Society*, **33**(10), 1747–1754.
- Mary, S. B., Rajesh, A. L. Influence of Surfactant Concentrations on N-Type Nanostructured Thermoelectric Oxide  $\text{CaMnO}_{3-\delta}$ . *INTERNATIONAL JOURNAL*

OF ENGINEERING RESEARCH & TECHNOLOGY (IJERT) Volume 08, Issue 09  
(September 2019),]

- Mouyane, M.; Itaalit, B.; Bernard, J. Houivet, D.; Noudem, J. G. Flash combustion synthesis of electron doped-CaMnO<sub>3</sub> thermoelectric oxides. *Powder Technol.* 2014, 264, 71 – 77.
- Paengson S, Pilasuta P, Singsoog K, Namhongsa W, Impho W, Seetawan T.  
Improvement in thermoelectric properties of CaMnO<sub>3</sub> by Bi doping and hot pressing. *Mater Today Proc.* 2017;4:6289–95.
- Park JW, Kwak DH, Yoon SH, Choi SC. Thermoelectric properties of Bi, Nb co-substituted CaMnO<sub>3</sub> at high temperature. *J Alloys Compd.* 2009;487(1–2):550–5.
- Presečnik, M., De Boor, J., & Bernik, S. (2016). Synthesis of single-phase Ca<sub>3</sub>Co<sub>4</sub>O<sub>9</sub> ceramics and their processing for a microstructure-enhanced thermoelectric performance. *Ceramics International*, 42(6), 7315–7327.
- Prasoetsopha, N., Pinitsoontorn, S., Kamwanna, T., Kurosaki, K., & Yamanaka, S.  
Effect of Ball-milling Time on Particle Size of Ca. *of natural sciences*, 635.
- Puri, N., Tandon, R. P., & Mahapatro, A. K. (2018). Fully dense hot pressed calcium cobalt oxide ceramics. *Ceramics International*, 44(6), 6337–6342.
- Purushotham, E., & Krishna, N. G. (2013). X-ray determination of crystallite size and effect of lattice strain on Debye–Waller factors of platinum nano powders. *Bulletin of Materials Science*, 36(6), 973–976.
- Qi, W. H.; Wang, M. P. Size, and shape dependent lattice parameters of metallic nanoparticles. *J Nanopart Res.* 2005, 7(1), 51 – 57.

- Rowe, D. M. (Ed.). (2018). *CRC handbook of thermoelectrics*. CRC press.
- Sotelo, A., Rasekh, S., Torres, M. A., Bosque, P., Madre, M. A., & Diez, J. C. (2015). Effect of synthesis methods on the  $\text{Ca}_3\text{Co}_4\text{O}_9$  thermoelectric ceramic performances. *Journal of Solid State Chemistry*, 221, 247–254.
- Thiel, P., Eilertsen, J., Populoh, S., Saucke, G., Döbeli, M., Shkabko, A., ... & Weidenkaff, A. (2013). Influence of tungsten substitution and oxygen deficiency on the thermoelectric properties of  $\text{CaMnO}_{3-\delta}$ . *Journal of Applied Physics*, 114(24), 243707.
- Thiel P, Populoh S, Yoon S, Saucke G, Rubenis K, Weidenkaff A. Charge-carrier hopping in highly conductive  $\text{CaMn}_{1-x}\text{M}_x\text{O}_{3-\delta}$  Thermoelectrics. *J Phys Chem C*. 2015;119(38):21860–7.
- Wang Y, Sui Y, Fan H, Wang X, Su Y, Su W. High temperature thermoelectric response of electron-Doped  $\text{CaMnO}_3$ . *Chem Mater*. 2009;21(19):4653–60.



## CHAPTER 5

### CONCLUSIONS and SUGGESTIONS

In this chapter is conclusion of synthesis of n-CaMnO<sub>3</sub>/p-Ca<sub>3</sub>Co<sub>4</sub>O<sub>9</sub> materials and fabricated the oxide multilayers thermoelectric module generator. Conclusions and suggestions based on the finding of this thesis are as follow:

#### Conclusions

##### Thermoelectric materials

We discussed about the effect of nano size of precursor powders by optimizing the process parameters for ball-milled, calcination and attempt to control the grain size by fast sintering times that influence on thermoelectric properties of CaMnO<sub>3</sub> and Ca<sub>3</sub>Co<sub>4</sub>O<sub>9</sub>.

As reported, increased milling time decreases the particle size of powders which leads to an increase in the diffusion kinetics during sintering. It can be seen from the results that the samples calcined at a lower temperature under an oxygen atmosphere demonstrate homogeneously dispersed nanoparticles are observed with a connected network structure is due to the recovery of oxygen atoms from the atmosphere. The polycrystalline CaMnO<sub>3</sub> material with orthorhombic *Pnma* symmetry were synthesized by solid-state reaction method and hot-pressing sintering. The XRD pattern of sample show single phase of CaMnO<sub>3</sub> and major crystal phase of all samples without any detectable secondary phase. The low-density undoped sample is

more likely to lose more oxygen at elevated temperatures. The SEM-images of calcined was demonstrated that the powder has a bimodal particle size distribution, consisting of coarse and small particles of about 50 nm to 200 nm. For the sintered sample has spherical shape, and the size (>50 after HP-sintering under identical conditions at 873 K for 1 h by adding PVA for hot-press sintering can be inserted in the vacancy between the grain of materials, but we added in small quantities make low density of bulk. The highest density of  $\text{CaMnO}_3$  sample is 58.92% of theoretical density. The elemental mapping of all samples shows homogenous distribution of Ca, Mn, and O. The EDS results show agree with the composition of initial atomic ratio. The sintered sample has  $S$  lower values because this sample is the capacity to compact the powder into a dense bulk within short times owing to the self-heat effect makes a low densified with larger grain size increases the influence on the  $S$  values of the scattering effect will be decreased. The highest value of  $S$  is  $-269.219 \mu\text{V/K}$  at 763 K. The lowest  $\rho$  value  $\text{CaMnO}_3$  sample is  $0.597 \Omega \text{ m}$  at 313 K to  $0.0179 \Omega \text{ m}$  at 723 K, respectively. The highest PF value of  $\text{CaMnO}_3$  is  $1.75 \times 10^{-4} \text{ W/mK}^2$  at 313 K, and it reached  $0.00452 \text{ W/mK}^2$  at 723 K, which is attributed by its lowest resistivity. For the thermal conductivity of sample was exhibited lower thermal conductivities over the whole temperature range that decreases when temperature increases from  $0.85 \text{ W/mK}$  at temperature 273 K was which became  $0.53 \text{ W/mK}$  at 973 K. It demonstrates that nanoparticles indeed reduce the thermal conductivity of  $\text{CaMnO}_3$  such reduction is associated with the enhanced phonon scattering by decreased size structured. Dimensionless figure of merit  $ZT$  of  $\text{CaMnO}_3$  sample was observed at 923 K around 0.00842.

Meanwhile, ball-milled powder has agglomerate make the reduction of the size of the spheres after ball-milled, which tend to come together and form large

aggregates. Calcined powder was the highest volume density because particle size was increased with increasing calcination temperatures. This could be due to the high surface energy of  $\text{Ca}_3\text{Co}_4\text{O}_9$  particles. While sintered sample was lowest particle size due to the decreased amount of time to short sintering time (0.5 h). As evident from this figure, decreasing the sintering time reduces the particle size and volume density of sample. The estimated values for the average crystallite size of nano precursor powder, after ball-milled is well below 6.90 nm, as observed clearly in the SEM images. The calcination temperatures 1173 K for 10 h, the grain size is relatively large, and the size distribution is uniform. The average grain size of calcined powder has two populations of  $\text{Ca}_3\text{Co}_4\text{O}_9$  particles seem to coexist: particles large particles, near 650 nm and exceedingly small particles, near 100 nm. The density values of nano sample are higher 94.87% due to the formation of small grain size during sintering, which could have helped the densification process. The  $S$  value of  $\text{Ca}_3\text{Co}_4\text{O}_9$  sample showed that it increased with increasing temperature from 160.15  $\mu\text{V/K}$  at 400 K, to 185  $\mu\text{V/K}$  at 973 K approximately. The  $\rho$  of sample was decreased with increasing temperature 31.51  $\Omega \text{ m}$  at 300 K to 17.39  $\Omega \text{ m}$  at 973 K. The calculated PF value of  $\text{Ca}_3\text{Co}_4\text{O}_9$  sample is 0.08  $\text{mW/mK}^2$  at 300 K, and it reached 0.19  $\text{mW/mK}^2$  at 973 K. While the thermal conductivity sample was exhibited lower thermal conductivities over the whole temperature range that decreases when temperature increases from 1.35  $\text{W/mK}$  at temperature 273 K was which became 0.73  $\text{W/mK}$  at 973 K. The best  $ZT$  value of  $\text{Ca}_3\text{Co}_4\text{O}_9$  reaches 0.25 at 973 K.

## Thermoelectric devices

For the fabrication of multilayer legs, the obtained pellets of CCO and CMO were fabricated by soldering method and exhibit resistance about 0.33  $\text{k}\Omega$ , 27.5  $\text{k}\Omega$ ,

and  $2.14 \text{ k}\Omega$ . A multilayer thermoelectric ceramics modules of 1-, and 2-pairs with series circuit and parallel circuit are constructed using misfit-layered  $\text{Ca}_3\text{Co}_4\text{O}_9$  and perovskite  $\text{CaMnO}_3$ . The output powers of the fabricated multilayer thermoelectric modules are measured, depending on the operating parameters and number of thermoelectric module pairs. A 1-, and 2-pairs with series circuit and 2- pairs parallel circuit of multilayer thermoelectric ceramics modules respectively generated open-circuit voltages ( $V_{oc}$ ) of 82.14 mV, 82.27 and 100.59 mV. The maximum output powers ( $P_{max}$ ) of all thermoelectric modules were increased with an increasing temperature difference  $\Delta T$  between the hot- and cold-side temperatures of the modules. At the temperature gradient  $\Delta T = 473 \text{ K}$ , the maximum output power of single thermoelectric module was  $7.30 \text{ }\mu\text{W}$ . However, the output powers of 2-pairs of series circuit thermoelectric module slightly decrease with in an increase in temperature difference  $6.12 \text{ }\mu\text{W}$ . While the output power of 2-pairs of parallel circuit was increased with an increasing in the same condition  $7.46 \text{ }\mu\text{W}$ , respectively. A significant increase in the output characteristics of the module shows that the multilayer is effective. The multilayer thermoelectric modules show promising output characteristics.

## Suggestion

1. The n- $\text{CaMnO}_3$  materials should be doped with elements to increase the dense of the bulk samples because this work has low density makes low thermoelectric performances.
2. For fabricated the multilayer oxide modules the n- $\text{CaMnO}_3$  has fragile between fabricated process because the low density of the bulk sample and when soldering/brazing joining with Ag electrode is not good contact with the material. When

test the modules must have problems with  $n\text{-CaMnO}_3$  and contacts make effect on the output power of each module.

3. When measurement the thermoelectric generator the heaters have an unstable temperature, we must calibrate the power source and found the oxidize on copper cover on heaters must be polished before using every time.



## APPENDICE





## APPENDICE A

### PUBLICATIONS



**First Author**

1. **Namhongsa, W.**, & Seetawan, T. (2022). Enhanced dimensionless figure-of-merit of  $\text{Ca}_3\text{Co}_4\text{O}_9$  by nano-sized precursor. Japanese Journal of Applied Physics, 61(3), 035501.
2. **Namhongsa, W.**, & Seetawan, T. (2022). High electrical power designing the horizontal shaped of bulk  $\text{Ca}_3\text{Co}_4\text{O}_9/\text{CaMnO}_3$ . Physica B: Condensed Matter, 636, 413865.

## REGULAR PAPER

Enhanced dimensionless figure-of-merit of  
 $\text{Ca}_3\text{Co}_4\text{O}_9$  by nano-sized precursor

To cite this article: Wanatchaporn Namhongsa and Tosawat Seetawan 2022 *Jpn. J. Appl. Phys.* **61** 035501

View the [article online](#) for updates and enhancements.

## You may also like

- [Preparation and Physical Properties of Segmented Thermoelectric  \$\text{YBa}\_2\text{Cu}\_3\text{O}\_{7-x}\$   \$\text{Ca}\_3\text{Co}\_4\text{O}\_9\$  Ceramics](#)  
P Wannasut, N Keawprak, P Jaiban et al.
- [Low temperature sintering and microwave dielectric properties of  \$\text{BaZn}\_2\text{Ti}\_2\text{O}\_{11}\$  ceramics with  \$\text{Li}\_2\text{O-B}\_2\text{O}\_3\text{-SiO}\_2\$  glass](#)  
S X Duan, E Z Li, Y W Chen et al.
- [Study of  \$\text{Ca}\_{1-x}\text{Bi}\_x\text{Co}\_4\text{O}\_9\$  \( \$0 < x \leq 0.5\$ \) as Novel Cathodes for H-SOFCs](#)  
Jing Zou, Jungdeok Park, Heechul Yoon et al.



## Enhanced dimensionless figure-of-merit of $\text{Ca}_3\text{Co}_4\text{O}_9$ by nano-sized precursor

Wanatchaporn Namhongsa<sup>1,2</sup> and Tosawat Seetawan<sup>1,2\*</sup>

<sup>1</sup>Program of Physics, Faculty of Science and Technology, Sakon Nakhon Rajabhat University, Sakon Nakhon, 47000, Thailand

<sup>2</sup>Thermoelectric Research Laboratory, Center of Excellence on Alternative Energy, Research and Development Institution, Sakon Nakhon Rajabhat University, Sakon Nakhon, 47000, Thailand

\*E-mail: [t\\_seetawan@snu.ac.th](mailto:t_seetawan@snu.ac.th)

Received June 14, 2021; revised December 11, 2021; accepted December 16, 2021; published online February 18, 2022

$\text{Ca}_3\text{Co}_4\text{O}_9$  sample synthesized from nanometer of  $\text{CaCO}_3$  and  $\text{Co}_2\text{O}_3$  sized precursor has been prepared by solid-state reaction and fast sintering by hot press method. The fast-sintering time can maintain the particle size of the nanometer. Their thermoelectric properties at high temperatures have been studied at 300–1000 K. The usage of a nano-sized precursor leads to decreased electrical resistivity, increased power factor, and would lead to huge dimensionless figure-of-merit ( $ZT$ ) growth, respectively. The main effect is observed on thermal conductivity that is lower than the sample synthesized with micrometer precursors powder from  $0.67 \text{ W mK}^{-1}$  which became  $0.36 \text{ W mK}^{-1}$  at 973 K. The best  $ZT$  value of  $\text{Ca}_3\text{Co}_4\text{O}_9$  reaches 0.51 at 973 K. © 2022 The Japan Society of Applied Physics

### 1. Introduction

Thermoelectric materials harvest energy by converting waste heat into electricity through different temperatures between the thermoelectric devices; this method is an attractive method to reduce greenhouse gas emissions.<sup>1–3</sup> This performance of thermoelectric materials can be predicted via considering the dimensionless figure-of-merit ( $ZT$ ) by  $ZT = S^2T/\rho\kappa$ , where  $S$  is the Seebeck coefficient (V/K),  $T$  is the absolute temperature,  $\rho$  is the electrical resistivity ( $\Omega \text{ m}$ ) and  $\kappa$  is the thermal conductivity ( $\text{W m}^{-1} \text{ K}$ ). The relationships of  $S$ ,  $\rho$  and  $\kappa$  are the most important factors leading to high or low  $ZT$  values of thermoelectric materials with a drastic dependence on carrier concentration, the electrical and thermal conductivity increase, while the Seebeck coefficient decreases with increasing carrier concentration.<sup>4,5</sup>

Several years ago, researchers have proposed a process to enhance the  $ZT$  value and reduce the bulk thermal conductivity by decreasing the grain sizes when the grain diameter is less than 500 nm to the dimensionality of materials to 1D nanostructures, which would lead to a large  $ZT$  increase.<sup>6</sup> Many efforts have been made to improve the  $ZT$  value of  $\text{Ca}_3\text{Co}_4\text{O}_9$  by improving the grain alignment in the materials or by chemical substitutions.

The electrical resistivity of  $\text{Ca}_3\text{Co}_4\text{O}_9$  was reduced by improving grain alignment, increasing grain size, and enhancing bulk density, and the improved power factor reached  $0.8 \text{ mW m K}^{-2}$  at 1073 K. However, the thermal conductivity was increased caused by the increase of the grain size and the enhancement of the degree of grain alignment is much smaller than the improvement of the power factor.<sup>7</sup> Furthermore, the researcher demonstrated the enhancement of the thermoelectric performance of  $\text{Ca}_3\text{Co}_4\text{O}_9$  via decreasing the grain size to nanoscale texturing and engineered interfaces. This strategy modified the crystal structure of  $\text{Ca}_3\text{Co}_4\text{O}_9$  and induced phonon scattering by point defects, leading to lower thermal conductivity. Nanoscale texturing along the  $c$ -axis provided the advantage of higher electrical conductivity and reduce thermal conductivity in hot-pressing or spark plasma sintering samples, enhancing the thermoelectric properties response (enhanced  $ZT$ ).<sup>8</sup>

Herein, we focus on oxide-based, which is a potential candidate for thermoelectric application due to its good

stability at high temperatures, less toxic, less expensive, and environmentally friendly.<sup>9</sup> The  $\text{Ca}_3\text{Co}_4\text{O}_9$  thermoelectric materials are cobaltite ceramics including the misfit-layered structure as  $[\text{Ca}_2\text{CoO}_3]_{b_1/b_2}[\text{CoO}_2]_{b_1/b_2}$ , where  $b_1$  and  $b_2$  refer to  $b$ -axis length of rock-salt type  $[\text{Ca}_2\text{CoO}_3]$  sublattice and  $\text{CdI}_2$ -type  $[\text{CoO}_2]$  sublattice, respectively. Which, these sublattices are stacked alternatively along the  $c$ -axis and the interaction of these two subsystems via displacive  $\text{Ca-O}$  bonds leads to anisotropic transport in the  $\text{Ca}_3\text{Co}_4\text{O}_9$  system.<sup>10</sup> Although  $\text{Ca}_3\text{Co}_4\text{O}_9$  exhibits a large  $ZT$  value at elevated temperatures, at lower temperatures the  $ZT$  value is much smaller because the thermal conductivity is dependent on the microstructure of bulk material and grain size effect on the thermoelectric properties of  $\text{Ca}_3\text{Co}_4\text{O}_9$  bulk samples. The  $\text{Ca}_3\text{Co}_4\text{O}_9$  bulk was synthesized by the hot-pressed method at 1173 K for 1 h and annealed by a furnace at 1173 K for 12 h. The electrical resistivity of the sample is  $24.2 \text{ m}\Omega \text{ cm}$  at 373 K, Seebeck coefficient  $205 \mu\text{V K}^{-1}$ , and power factor  $0.17 \text{ mW m}^{-1} \text{ K}^{-2}$  at 873 K, respectively.<sup>11</sup> F. Delorme et al. have shown the effect of micrometer, nanometer and mixing sizes of precursors powder, which were prepared by a solid-state reaction and spark plasma sintering. The  $\text{Ca}_3\text{Co}_4\text{O}_9$  sample was synthesized from nanosized  $\text{CaO}$ –micro-sized  $\text{Co}_3\text{O}_4$  precursors lead to slightly higher electrical conductivity and higher power factor, meanwhile the thermal conductivity values are lower around  $1.65 \text{ W m}^{-1} \text{ K}^{-1}$  at 1000 K more than micro-sized  $\text{CaO}$ –micro-sized  $\text{Co}_3\text{O}_4$  sized precursors sample. The best  $ZT$  value was reached 0.18 at 973 K for the sample synthesized from nanosized  $\text{CaO}$  and micrometer-sized  $\text{Co}_3\text{O}_4$ .<sup>12</sup> The  $\text{Ca}_3\text{Co}_4\text{O}_9$  was prepared by powder synthesis with the solid-state reaction and conventional sintering. The  $\text{Ca}_3\text{Co}_4\text{O}_9$  microstructure has a strong texture of the  $\text{Ca}_3\text{Co}_4\text{O}_9$  platelets within lamination. The electrical conductivity of conventional sintering is  $56 \text{ S cm}^{-1}$  at 373 K. The thermal conductivity of the  $\text{Ca}_3\text{Co}_4\text{O}_9$  sample is  $1.3 \text{ W/(mK)}$  at 373 K.  $ZT$  of the  $\text{Ca}_3\text{Co}_4\text{O}_9$  sample increases with temperature and reaches about 0.11 at 873 K.<sup>13</sup> Gunes et al. analyzed the effect of grain size and porosity on thermal conductivity of  $\text{Ca}_3\text{Co}_4\text{O}_9$  ceramics with various grain sizes; for nano-sized samples exhibit higher  $ZT$  values, they report a thermal conductivity  $0.32 \text{ W/(mK)}$  at 300 K, decreasing with particle sizes. The  $ZT$  value reached 0.29 at 1273 K. The increase in

$ZT$  at high temperatures is due to several factors. First, the thermal conductivity is already low and remains constant. Second, the Seebeck coefficient increases with temperature; however, the electrical transport behavior changes, and resistivity decreases near 420 K, which substantially contributes to the enhancement of  $ZT$  at high temperature. The synthesized nano-sized samples exhibited higher electrical resistivity due to the quantity of pores, which increased the carrier scattering at boundaries, and the lower thermal conductivity due to phonon boundary scattering at the increased number of interfaces.  $ZT$  was enhanced due to the substantial decrease in the thermal conductivity despite the great increase in resistivity. The total thermal conductivity reduction was experimentally observed to be larger for smaller grain sizes and higher porosities. Because the size and morphology of materials strongly affect  $ZT$  values.<sup>14)</sup>

However, no detailed reports are available on the  $\text{Ca}_3\text{Co}_4\text{O}_9$  oxide concerning the combined nanostructure and enhanced the  $ZT$  values. In this work, the effect of nano-sized precursors on the enhancement of the  $ZT$  value of  $\text{Ca}_3\text{Co}_4\text{O}_9$  sample is reported by decreasing the total thermal conductivity without significantly degrading the Seebeck coefficient.

## 2. Materials and methods

The  $\text{Ca}_3\text{Co}_4\text{O}_9$  sample was synthesized from mixing nano precursor powders  $\text{CaCO}_3$  (US Research Nanomaterials, Inc., purity 98%) and  $\text{Co}_2\text{O}_3$  (US Research Nanomaterials, Inc., purity 99.7%) with a planetary ball mill (PBM) (Retsch<sup>TM</sup> PM 400 Model Planetary Ball Mill). The ratio of the ball with powder was 10:5, with a diameter of 10 mm, and performed at 350 rpm. To control the grain size, the ball-milling time was set to 8 h. Mixed nanopowder precursors were calcined at 1173 K for 10 h and then fast sintered by hot-pressed in a graphite die using hot-press systems (HP, TMAX-PressFumace1 Model) using a pressure of 20 MPa under Ar atmosphere at 1173 K for 0.5 h by control heating rate up  $5^\circ\text{C min}^{-1}$ .

The resulting bulk samples were precisely analyzed and the crystal structure of the samples were characterized using powder X-ray diffraction (XRD) in the  $2\theta$  range  $10^\circ$ – $70^\circ$  and a continuous scan mode of  $2^\circ/\text{min}$  receiving slit = 0.15000 mm would calculate it as 3251 steps, using  $\text{CuK}\alpha$  radiation ( $\lambda = 1.5406 \text{ \AA}$ ) with a voltage of 40 kV and current of 30 mA, (LabX XRD-6100, SHIMADZU, Japan) at room temperature.

The crystallite size of all samples was involuted from the modified Scherrer's formula as follows:

$$D = K\lambda / \beta_{hkl} \cos \theta \quad (1)$$

where  $D$  is the crystalline size in nanometers,  $K$  is a constant whose value depends on particle shape and usually varies from 0.62 to 2.08.<sup>15,16)</sup> The constant of proportionality,  $K$ , is 0.94 and depends on how the width is determined, the shape of the crystal, and the size distribution (assumes for an FWHM of spherical crystals with cubic symmetry), and  $\lambda$  is 1.5406 Å wavelength of Cu-K $\alpha$  radiation,  $\beta_{hkl}$  is the FWHM and  $\theta$  is the Bragg's angle (in radians).

The microstructure of the sample was examined using field emission scanning electron microscopy (FESEM JSM-7610F, JEOL, Japan) to obtain SEM images. Insulating

samples have been sputter-coated with a thin layer of about 10 nanometers (nm) of a conductive material such as platinum or gold prior to observation by Auto Fine Coater (JEOL JEC-3000FC).

Thermoelectric properties of the sintered samples were cut along the radial direction into bars with a dimension of  $3 \times 3 \times 15 \text{ mm}^3$  measured by a standard four-probe method using the Seebeck coefficient/electrical resistance measuring system (ZEM-3, ULVAC-RIKO, Japan) at a temperature range 300–973 K in a He atmosphere.

The thermal conductivity can be calculated using the relationship of thermal diffusivity ( $\alpha$ ), heat capacity  $C_p$ , and density of bulk ( $d$ ) as the following:

$$\kappa = \alpha(T)C_p(T)d(T) \quad (2)$$

The thermal diffusivity values ( $\alpha$ ) were measured by flash diffusivity apparatus (Netzsch LFA-467, Germany) from room temperature to 973 K in an argon atmosphere. The heat capacity  $C_p$  can be calculated using the following equation:

$$C_p = \frac{1}{m} \frac{dQ}{dT} = \frac{Q}{m\Delta T} \quad (3)$$

where  $C_p$  is the specific heat capacity at a constant pressure ( $\text{J}\cdot\text{Kg}^{-1}\cdot\text{K}^{-1}$ ),  $m$  is the mass (kg),  $Q$  is the heat energy (J) and  $T$  is the temperature (K). From this, the specific heat of  $\text{Ca}_3\text{Co}_4\text{O}_9$  material was calculated as  $399.12(8) \text{ J kg}^{-1} \text{ K}^{-1}$ . The experimental relative density ( $d$ ) of the ceramic was calculated based on the sample size and weight measured by density kit (MS-DNY-54, METTLER TOLEDO, Switzerland) with the Archimedes method as follows:

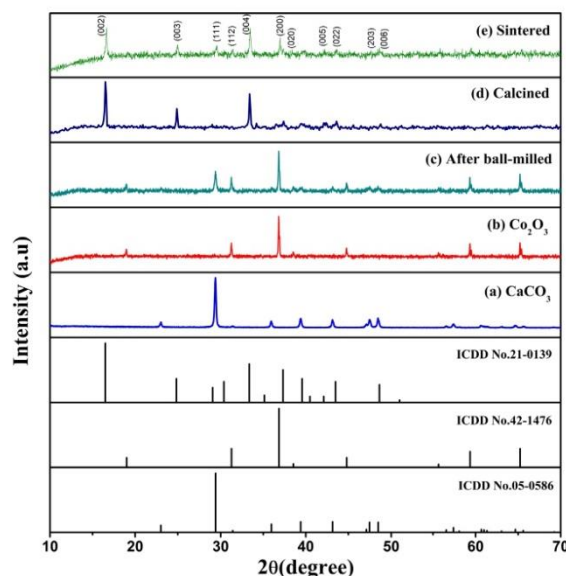
$$d = \frac{A}{A - B}(d_0 - d_L) + d_L \quad (4)$$

where  $d$  is the density determination of solids,  $A$  is the weight of the sample in air,  $B$  is the weight of sample in an auxiliary liquid,  $d_0$  is the density of auxiliary liquid followed by differential room temperature and  $d_L$  is the density of air ( $0.0012 \text{ g cm}^{-3}$ ). To ensure the accuracy of the results, all characterization tests were performed using the same sample. By using experimentally measured thermal diffusivity, specific heat, and density the thermal conductivity of the samples was determined.

## 3. Results and discussion

XRD patterns for the nano precursors, ball-milled powder, calcined powder, and sintered powder are shown in Figs. 1(a)–1(e). The peaks in the XRD patterns indicated that (a) the  $\text{CaCO}_3$  and (b)  $\text{Co}_2\text{O}_3$  phase. The  $\text{CaCO}_3$  phases were shown as broad peaks because the crystallite size is exceedingly small more than the  $\text{Co}_2\text{O}_3$  phases corresponding with Table I. (c) The mixing treatment (8 h at 350 rpm in an agate ball mill) does not lead to the  $\text{Ca}_3\text{Co}_4\text{O}_9$  phase because they are composed of the combination inherent in both the  $\text{CaCO}_3$  and  $\text{Co}_2\text{O}_3$  peaks corresponding with N. Puri et al.<sup>17)</sup> and indicates that the ball-milled process facilitates the formation of a uniformly distributed mixture containing both the precursors. However, when we expanded image peaks in the range  $2\theta = 29$ – $32^\circ$ , shown in Fig. 2, the broad peaks of the mixed nano precursor powders after being ball-milled for 8 h causing the crystallite size of mixed nano precursor





**Fig. 1.** (Color online) XRD patterns of the (a) precursors:  $\text{CaCO}_3$  nanoparticles, (b)  $\text{Co}_2\text{O}_3$  nanoparticles, (c) after ball-milled, (d)  $\text{Ca}_3\text{Co}_4\text{O}_9$  powders prepared by calcination and (e)  $\text{Ca}_3\text{Co}_4\text{O}_9$  powders prepared fast sintering by the hot-press method, respectively. The vertical lines at the bottom axis represent various planes of  $\text{Co}_2\text{O}_3$ ,  $\text{CaCO}_3$ , and  $\text{Ca}_3\text{Co}_4\text{O}_9$  mentioned in ICDD No. 05-0586, 42-1476 and 21-0139, respectively.

**Table I.** The average crystallite size ( $D$ ) determined by XRD of nano precursors powder, ball-milled, calcined samples, and grain size ( $d$ ) from SEM for the sintered  $\text{Ca}_3\text{Co}_4\text{O}_9$  sample.

Samples	$2\theta$ (deg.)	FWHM (deg.)	$D$ (nm)	$d$ (nm)
$\text{CaCO}_3$	29.38	0.53	19.45(6)	—
$\text{Co}_2\text{O}_3$	36.82	0.34	36.56(1)	—
After ball-milled	36.82	1.32	6.90(2)	—
Calcined	16.5	0.55	18.14(1)	—
Sintered	16.5	0.55	51.50(1)	>100

powders to become decreased with increasing ball mill time and influenced by the initial size of the precursors within the mixture corresponding to N. Prasertsopha et al.<sup>18)</sup> Figure 1(d) shows the phase-composition analysis of the calcined samples showed a strong influence of the particle size of the  $\text{CaCO}_3$  and the  $\text{Co}_2\text{O}_3$  in the starting-powder mixtures on the formation of the  $\text{Ca}_3\text{Co}_4\text{O}_9$  phase. The calcined powder showed a major crystal phase of the  $\text{Ca}_3\text{Co}_4\text{O}_9$  matched with the ICDD No. 21-0139, the XRD patterns with the dominant (002) plane, and the expected ratio of the two highest-intensity peaks for (002) and (004) planes (at  $16.5^\circ$  and  $33.6^\circ$ , respectively). While for the peak at  $42.4^\circ$  we found the minor diffraction peaks correspond to the presence of  $\text{Ca}_3\text{Co}_2\text{O}_6$  (ICDD No. 23-0111) as an intermediate phase. Minor deviations in the stoichiometry and homogeneity of the sample were expected to facilitate the formation of secondary phases. This has been attributed to long hold durations during calcination or temperatures  $1173\text{ K}$ , favoring the decomposition of the  $\text{Ca}_3\text{Co}_4\text{O}_9$  phase

into the aforementioned phases. The diffraction signals of the calcined powders gradually narrowed and strengthened with increasing calcination temperatures, demonstrating the increase in crystallinity and crystallite size and Fig. 1(e) from the data represented the single  $\text{Ca}_3\text{Co}_4\text{O}_9$  phase can be observed at  $1173\text{ K}$  produced with the signature (002) plane at  $16.5^\circ$  indicated that the major diffraction peaks assigned for  $\text{Ca}_3\text{Co}_4\text{O}_9$  based phase of the monoclinic structure and other planes at peak positions in accordance with ICDD No. 21-0139, consistent with the alternate stacking sub-systems with a two-dimensional triangular lattice of rock-salt-type  $[\text{Ca}_2\text{CoO}_3]$  layers sandwiched between two hexagonal  $[\text{CoO}_2]$  layers along the  $c$ -axis corresponding to Masset, A. C., et al.<sup>19)</sup> The quality of the starting powders has a significant impact on the synthesis of the  $\text{Ca}_3\text{Co}_4\text{O}_9$  phase, and the smoothness observed in the  $\text{Ca}_3\text{Co}_4\text{O}_9$  phase formation reactions was most probably due to the fine-grained starting powders.

For particle size analysis, the particle size will change with changing molarity. The particle size of the ball-milled, calcined, and sintered are about  $8.68(1)\text{ }\mu\text{m}$ ,  $7.64(2)\text{ }\mu\text{m}$ , and  $5.92(1)\text{ }\mu\text{m}$ , respectively, seen as a tail in the size distribution diagram given in Fig. 3. The molarity was decreased with decreasing particle size. The ball-milled powder has an agglomerate making the reduction of the size of the spheres after ball-milling, which tends to come together and form large aggregates. Calcined powder was the highest volume density because particle size was increased with increasing calcination temperatures. This could be due

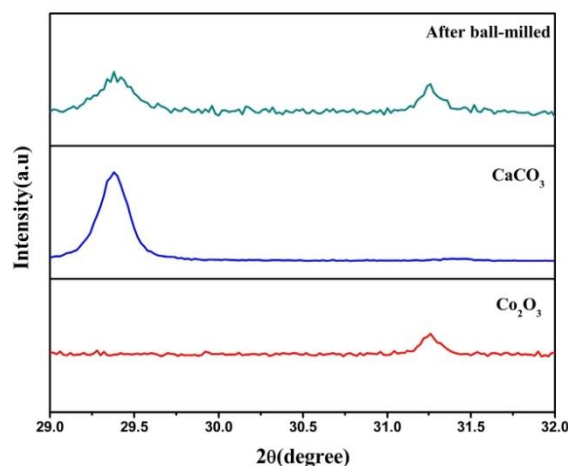


Fig. 2. (Color online) XRD patterns expanded image peaks in range  $2\theta = 29\text{--}32^\circ$ , the broad peaks of the mixed nano precursor powders after ball milling.

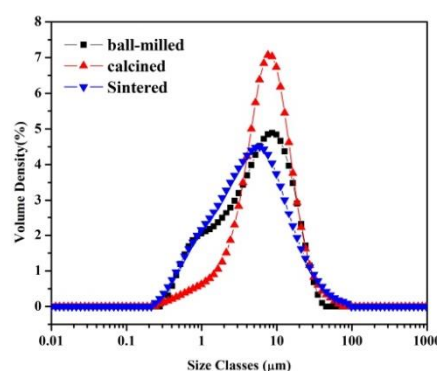


Fig. 3. (Color online) Particle size distribution of  $\text{Ca}_3\text{Co}_4\text{O}_9$ .

to the high surface energy of  $\text{Ca}_3\text{Co}_4\text{O}_9$  particles. At higher calcination temperatures, the surface energy of the particles tended to increase, resulting in increased aggregation. This consequently produced the larger particles, while the sintered sample was the lowest particle size due to the decreased amount of time to short sintering time (0.5 h). As evident from this figure, decreasing the sintering time reduces the particle size and volume density of the sample.

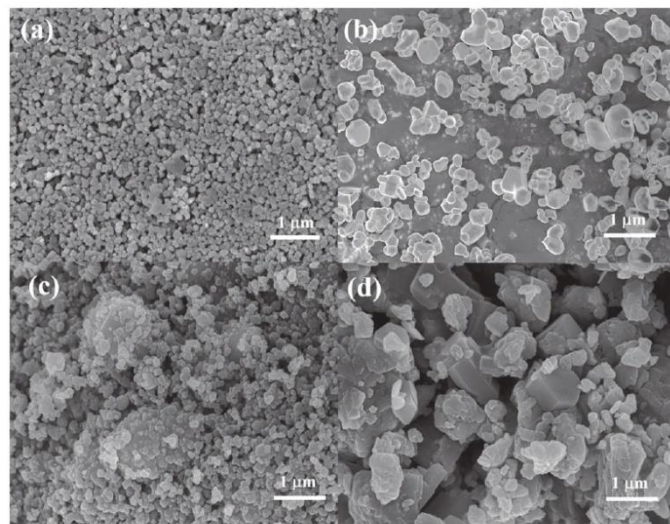
The average crystallite size ( $L$ ) is calculated for the powder samples using the Scherrer's formula.<sup>15,16)</sup> The estimated values for the average crystallite size of nano precursor powder, after ball-milling, calcined powder as shown in Table I. For  $\text{CaCO}_3$  and  $\text{Co}_2\text{O}_3$  the crystallite sizes obtained from XRD for the ball-milled sample are well below 6.90 nm, as observed clearly in the SEM images where the grain sizes are several nanometers as shown in Fig. 4(c). This observed

decrease in crystallite size with increasing ball-milling time is attributed to the initial sizes of the precursor mixture experiencing calcination.

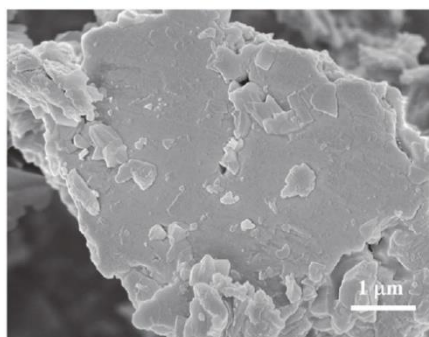
The nano precursors powder, after ball-milling and calcination, had its particle sizes confirmed by SEM, as shown in Fig. 4, which shows representative micrographs of the two possible precursors: the  $\text{CaCO}_3$  precursor is composed of particles size 89 nm rhombohedral crystal [Fig. 4(a)],  $\text{Co}_2\text{O}_3$  is composed of particles 393 nm octahedral crystals [Fig. 4(b)]. Figure 4(c), shows an image of after ball-milling with irregular features average sizes of two populations  $\text{CaCO}_3$  and  $\text{Co}_2\text{O}_3$  which the reduction in feature sizes is monitored for the sample prepared with increasing ball-milled time and Fig. 4(d) observations confirm that the calcined powder contained the same plate as faceted rectangular shaped crystal grains. The size of the particle increases as calcination temperature increases. This resembles the inherent properties of lowering down the dimension using ball-milled and the formation of larger features during calcination. For calcination temperatures of 1173 K for 10 h, the grain size is relatively large, and the size distribution is uniform. The average grain size of calcined powder has two populations of  $\text{Ca}_3\text{Co}_4\text{O}_9$  particles which seem to coexist: large particles, near 650 nm, and exceedingly small particles, near 100 nm.

The morphology of the sintered samples is shown in Fig. 5. After fast sintering, the grain size of  $\text{Ca}_3\text{Co}_4\text{O}_9$  is observed to grow larger after sintering and exhibited a dense microstructure of lamellar grains in size and a strong texture perpendicular to the direction of the applied pressure level. The lamellar grains of  $\text{Ca}_3\text{Co}_4\text{O}_9$  have appeared to be a large area, and such texture would be advantageous for thermoelectric performance since the thermoelectric properties of layered  $\text{Ca}_3\text{Co}_4\text{O}_9$  are highly anisotropic to cause a high Seebeck coefficient. The small grain around the lamellar grains was induced by phonon scattering by point defects,





**Fig. 4.** SEM micrographs of the precursors, (a)  $\text{CaCO}_3$  nanoparticles, (b)  $\text{Co}_2\text{O}_3$  nanoparticles, and (c) ball-milled the mixed nano precursors powder after ball milling showing aggregates of nanoparticles (d) calcined powder.



**Fig. 5.** SEM micrographs of the  $\text{Ca}_3\text{Co}_4\text{O}_9$  fast-sintering sample.

leading to lower thermal conductivity. These authors have explained that this behavior should be related to the reduction in the number of grain boundaries due to the improvement of grain alignment and the increase in bulk density corresponding to this work shows the high-density value of the bulk  $\text{Ca}_3\text{Co}_4\text{O}_9$  sample.

Moreover, the diffraction patterns of the  $\text{Ca}_3\text{Co}_4\text{O}_9$  calcined and sintered sample helped to calculate the lattice parameter ( $a$ ,  $b$ ,  $c$ ) the density, and relative density, which are given in Table II. The lattice parameter is determined by XRD results. It has been reported that the lattice parameter increases or decreases as a function of the crystallite size in the structure and it can make a change in the properties of these materials.<sup>20,21</sup> Subsequently, the sintered sample

**Table II.** The density, relative density, and the lattice parameter ( $a$ ,  $b$ , and  $c$ ) of  $\text{Ca}_3\text{Co}_4\text{O}_9$  samples.

Samples	Density (g $\text{cm}^{-3}$ )	Relative Density %	Lattice Parameters ( $\text{\AA}$ )		
			$a$	$b$	$c$
Calcined	—	—	4.88(5)	4.57(7)	10.90(1)
Sintered	4.443 4.68 <sup>22)</sup>	94.87	4.87(1)	4.58(4)	10.87(8)

presents a high bulk density with an apparent density value larger than 94.87% of the relative density.

Temperature dependence of the Seebeck coefficient ( $S$ ) of  $\text{Ca}_3\text{Co}_4\text{O}_9$  sample compared with the literature data<sup>12,23,24</sup> is shown in Fig. 6. The Seebeck coefficient of all samples shows a positive value over the measured temperature range, indicating p-type conduction and that the charge transport is dominated by defect electrons corresponding with the results of samples HP<sup>12</sup>, SSR.<sup>23,24</sup> The  $S$  value of the  $\text{Ca}_3\text{Co}_4\text{O}_9$  sample showed that it increased with increasing temperature from  $160.15 \mu\text{V K}^{-1}$  at 400 K, to  $185 \mu\text{V K}^{-1}$  at 973 K approximately. However, the  $S$  shows a slight decrease of  $\sim 156.87 \mu\text{V K}^{-1}$  at 380 K. After calcination and fast sintering by the hot-pressed method, the XRD pattern shows the single phase and the grain size is still nanometers, and the two populations particles seem to coexist with lamellar grains and small grains that occur around observed from SEM images. The small grains that occur around the lamellar grains have high mobility and low phonon transport properties giving a high Seebeck coefficient. While for the  $\text{Ca}_3\text{Co}_4\text{O}_9$  sample sintered by the solid-state reaction method<sup>24</sup> the values have shown a slightly different behavior, they possess lower  $S$  values from room temperature to

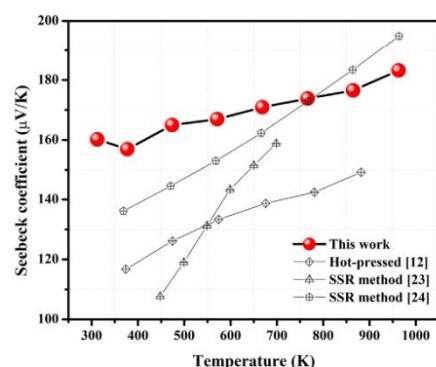


Fig. 6. (Color online) Dependence of the  $S$  value on the temperature of the  $\text{Ca}_3\text{Co}_4\text{O}_9$  sample synthesized by fast sintering with a hot-pressed method.

~673 K and higher values at higher temperatures. In addition, the  $\text{Ca}_3\text{Co}_4\text{O}_9$  sample sintered by the hot-pressing<sup>12)</sup> and solid-state reaction method<sup>23)</sup> had lower  $S$  values in comparison to the other samples because this method has the capability to compact the powder into a dense bulk within long times owing to the self-heating effect being well densified with micrometers of grain size, increasing the influence on the  $S$  values of the scattering effect which will be decreased. Therefore, when the length of grains is larger, the influence of temperature on the  $S$  values becomes more significant. These values are extremely high and agree with the high thermal conductivity values.

In Fig. 7 the  $\rho$  curves of the  $\text{Ca}_3\text{Co}_4\text{O}_9$  samples had similar behavior corresponding to the metal to semiconducting transition in the range 273–973 K. The  $\rho$  of the samples was decreased with increasing temperature 31.51 mΩ cm at 300 K to 17.39 mΩ cm at 973 K when corresponding with

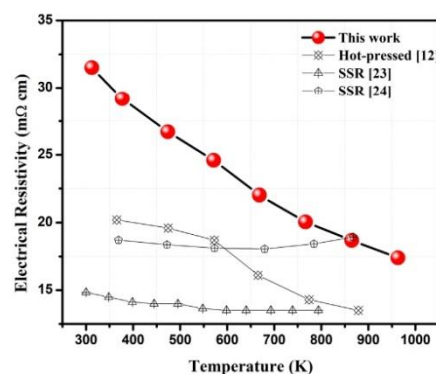


Fig. 7. (Color online) Dependence of the  $\rho$  on the temperature of the  $\text{Ca}_3\text{Co}_4\text{O}_9$  sample synthesized by fast sintering with a hot-pressed method.

literature data. The monoclinic structure of  $\text{Ca}_3\text{Co}_4\text{O}_9$  is comprised of two misfit layered subsystems: a distorted rock salt-type  $\text{Ca}_2\text{CoO}_3$  layer sandwiched between two  $\text{CdI}_2$ -type  $\text{CoO}_2$  layers along the  $c$ -axis.  $\text{CoO}_2$  nanosheets possessing a strongly correlated electron system serve as electronic transport layers (i.e., high electrical conductivity) and  $\text{Ca}_2\text{CoO}_3$  misfit layers serve as phonon scattering regions resulting in low thermal conductivity.

The temperature dependence on the power factor ( $PF = S^2/\rho$ ) of the  $\text{Ca}_3\text{Co}_4\text{O}_9$  sample is shown in Fig. 8. The  $PF$  value characteristics with the values increased with increasing temperature corresponding with the literature.<sup>12,23,24)</sup> The calculated  $PF$  value of the  $\text{Ca}_3\text{Co}_4\text{O}_9$  sample is 0.08 mW mK<sup>-2</sup> at 300 K, and it reached 0.19 mW mK<sup>-2</sup> at 973 K. When compared with the literature from Sotelo et al.,<sup>24)</sup> they have synthesized a nanometric grain size from the classical solid-state route. The result shows similarity with the values in this work.

Since thermal conductivity is a function of thermal diffusivity, specific heat capacity at constant pressure and density, the relationship between thermal conductivity and temperature can be obtained by measuring thermal diffusivity, specific heat capacity at constant pressure, and density. Figure 9 shows that the thermal conductivity decreases with the increase of temperature. The thermal conductivity sample exhibited lower thermal conductivities over the whole temperature range from 0.67 W m K<sup>-1</sup> at temperature 298 K was which became 0.36 W m K<sup>-1</sup> at 973 K. The  $\kappa$  values of  $\text{Ca}_3\text{Co}_4\text{O}_9$  samples were also lower when compared with other well-known oxide ceramics.<sup>11,23)</sup> It is evident that the lower thermal conductivity values were caused by the  $\text{Ca}_3\text{Co}_4\text{O}_9$  sample that was synthesized from nano powder precursors and the fast sintering with the hot-pressed was highly densified, the influence of porosity on thermal transport properties can be neglected<sup>25)</sup> and nanoscale have interfaces, which could create additional phonon scattering. Therefore, it is evident that the lower  $\kappa$  values were caused by the enhancement of phonon scattering due to the fine microstructure. The thermal conductivity is dominated by phonon vibrations when the semiconductor material has a low carrier concentration. However, it is dominated by the

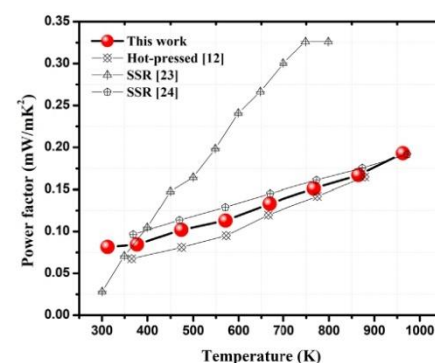


Fig. 8. (Color online) Temperature dependence of the power factor of the  $\text{Ca}_3\text{Co}_4\text{O}_9$  sample.

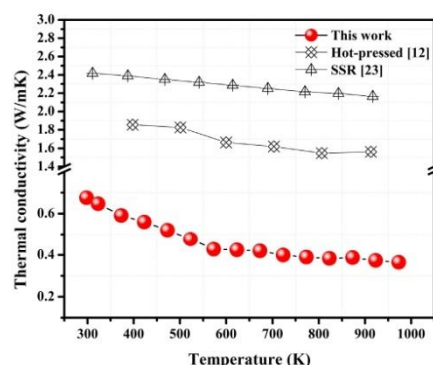


Fig. 9. (Color online) Dependence of the  $\kappa$  on the temperature of the  $\text{Ca}_3\text{Co}_4\text{O}_9$  sample was synthesized by fast sintering with a hot-pressed method.

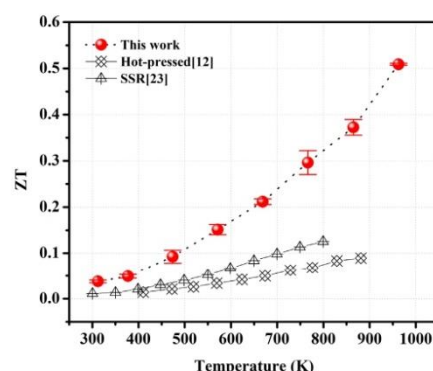


Fig. 10. (Color online) Dimensionless figure of merit ( $ZT$ ) of the  $\text{Ca}_3\text{Co}_4\text{O}_9$  sample.

concentration of the carriers when the carrier concentration increases. Therefore, the decrease in thermal conductivity observed for samples synthesized from nano-sized precursors must be related to the decrease of the lattice component of the thermal conductivity  $k_l$ . This decrease must be attributed to an increase in the phonon scattering. This scattering could be related to the smaller size of the  $\text{Ca}_3\text{Co}_4\text{O}_9$  particles and the average particle size of the samples synthesized from nano-sized precursors.

The dimensionless figure of merit  $ZT$  was calculated, as shown in Fig. 10. The maximum  $ZT$  value of  $\text{Ca}_3\text{Co}_4\text{O}_9$  sample was observed at 923 K around 0.51 when compared with other methods from the literature data, which is an exceptionally large value among oxide materials for undoping materials. The thermoelectric efficiency of this system is effectively improved by nano structuring, as results show the enhanced  $ZT$  was increased with increasing temperature due to the lower electrical resistivity and significantly lower thermal conductivity in our sample due to the method for

synthesizing nanoscale powders and sintering the nano powder, with the short durations times for significantly decreased grain growth. Further optimization of the synthesis process such as a shorter period at high temperature should lead to even smaller  $\text{Ca}_3\text{Co}_4\text{O}_9$  particles which would, in turn, decrease thermal conductivity and thus lead to better  $ZT$  values.

#### 4. Conclusions

We discussed the effect of nano-size precursor powders by optimizing the process parameters for ball-milled, calcination and attempted to control the grain size by fast sintering times that influence the thermoelectric properties of  $\text{Ca}_3\text{Co}_4\text{O}_9$ . The  $\text{Ca}_3\text{Co}_4\text{O}_9$  sample has an improved characteristic of the material due to the small grain size, revealed as disk-like microstructures and grains randomly throughout the material. The density values of nano samples are higher due to the formation of small grain size during sintering, which could have helped the densification process. In addition, the lowest thermal conductivity of  $\text{Ca}_3\text{Co}_4\text{O}_9$  due to the nano precursor powder has a strategy that modified the crystal structure and induced phonon scattering leading to lower thermal conductivity when compared with synthesis by micro precursor powder. The best  $ZT$  value of  $\text{Ca}_3\text{Co}_4\text{O}_9$  reaches 0.51 at 973 K.

#### Acknowledgments

The authors would like to express their gratitude to the research facility support from the Center of Excellence on Alternative Energy, Sakon Nakhon Rajabhat University, and the thermal diffusivity measurements were supported by Dr. Sora-at Tanusilp and Prof. Ken Kurosaki at Kyoto University, Japan.

#### Funding

This work is financially supported by The Royal Golden Jubilee PhD Programme (RGJ-PhD.) (Grant No. PhD/0065/2560), Thailand Research Fund (TRF) Research Career Development Grant, (RSA6180070).

#### ORCID iDs

Tosawat Seetawan  <https://orcid.org/0000-0003-4297-3452>

- 1) J. W. Fergus, *Eur. Ceram. Soc.* **32**, 525 (2012).
- 2) S. M. Choi, K. H. Lee, C. H. Lim, and W. S. Seo, *Energy Convers. Manag.* **52**, 335 (2011).
- 3) R. Funahashi, I. Matsubara, H. Ikuta, T. Takeuchi, U. Mizutani, and S. Sodeoka, *Jpn. J. Appl. Phys.* **39**, L1127 (2000).
- 4) M. Kumagai, K. Kurosaki, Y. Ohishi, H. Muta, and S. Yamanaka, *Mater. Trans.*, 1215–1228 (2014).
- 5) A. Minnich, M. S. Dresselhaus, Z. F. Ren, and G. Chen, *Energy Environ. Sci.* **2**, 466 (2009).
- 6) X. J. Zheng, L. Zhu, Y. H. Zhou, and Q. Zhang, *Appl. Phys. Lett.* **87**, 242101 (2005).
- 7) M. Mikami, E. Guilmeau, R. Funahashi, K. Chong, and D. Chateigner, *J. Mater. Res.* **20**, 2491 (2005).
- 8) M. E. Song, H. Lee, M. G. Kang, W. Li, D. Maurya, B. Poudel, and S. Priya, *ACS omega* **3**, 10798 (2018).
- 9) F. Delorme, D. O. Ovono, P. Marudhachalam, c. f. Martin, and O. Fraboulet, *Mater. Res. Bull.* **47**, 1169 (2012).
- 10) Y. Wang, Y. Sui, J. Cheng, X. Wang, and W. Su, *J. Alloys Compd.* **477**, 817 (2009).
- 11) A. Angnanon, *J. Mater. Sci.* **9**, 469 (2020).
- 12) M. Presečnik, J. De Boor, and S. Bernik, *Ceram. Int.* **42**, 7315 (2016).

- 13) T. Schulz, T. Reimann, A. Bochmann, A. Vogel, B. Capraro, B. Mieller, and J. Töpfer, *J. Eur. Ceram.* **38**, 1600 (2018).
- 14) M. Gunes and M. Ozenbas, *J. Alloys Compd.* **626**, 360 (2015).
- 15) E. Purushotham and N. G. Krishna, *Bull. Mater. Sci.* **36**, 973 (2013).
- 16) J. I. Langford and A. J. C. Wilson, *J. Appl. Crystallogr.* **11**, 102 (1978).
- 17) N. Puri, R. P. Tandon, and A. K. Mahapatro, *Ceram. Int.* **44**, 6337 (2018).
- 18) N. Prasertsotha, S. Pinitsoontorn, T. Kamwanna, K. Kurosaki, and S. Yamanaka, *CMUJ NS Special Issue on Physics*, **13**, 635 (2014).
- 19) A. C. Masset, C. Michel, A. Maignan, M. Hervieu, O. Toulemonde, F. Studer, and J. Hejmanek, *Phys. Rev. B* **62**, 166 (2000).
- 20) M. Dittrich and G. Schumacher, *Mater. Sci. Eng. C* **604**, 27 (2014).
- 21) W. H. Qi and M. P. Wang, *J. Nanoparticle Res.* **7**, 51 (2005).
- 22) M. A. Madre, F. M. Costa, N. M. Ferreira, A. Sotelo, M. A. Torres, G. Constantinescu, and J. C. Diez, *J. Eur. Ceram. Soc.* **33**, 1747 (2013).
- 23) S. Saini, H. S. Yaddanapudi, K. Tian, Y. Yin, D. Maggini, and A. Tiwari, *Sci. Rep.* **7**, 44621 (2017).
- 24) A. Sotelo, S. Rasekh, M. A. Torres, P. Bosque, M. A. Madre, and J. C. Diez, *J. Solid State Chem.* **221**, 247 (2015).
- 25) E. Combe, R. Funahashi, T. Barbier, F. Azough, and R. Freer, *Mater. Res.* **31**, 1296 (2016).





Contents lists available at ScienceDirect

Physica B: Physics of Condensed Matter

journal homepage: [www.elsevier.com/locate/physb](http://www.elsevier.com/locate/physb)

# High electrical power designing the horizontal shaped of bulk $\text{Ca}_3\text{Co}_4\text{O}_9/\text{CaMnO}_3$

W. Namhongsa<sup>a,b</sup>, T. Seetawan<sup>a,b,\*</sup>

<sup>a</sup> Program of Physics, Faculty of Science and Technology, Sakon Nakhon Rajabhat University, Sakon Nakhon, 47000, Thailand

<sup>b</sup> Thermoelectric Research Laboratory, Center of Excellence on Alternative Energy, Research and Development Institution, Sakon Nakhon Rajabhat University, Sakon Nakhon, 47000, Thailand

## ARTICLE INFO

### Keywords:

Horizontal shape  
 $\text{Ca}_3\text{Co}_4\text{O}_9$   
 $\text{CaMnO}_3$   
 Thermoelectric properties  
 Thermoelectric device  
 Output powers

## ABSTRACT

A horizontal-shaped cell of a bulk oxide thermoelectric material was constructed using misfit layered  $\text{Ca}_3\text{Co}_4\text{O}_9$  (CCO) and perovskite  $\text{CaMnO}_3$  (CMO). The electrical power was measured based on the operating parameters. The horizontal shape can improve the efficiency of the thermoelectric cell because it reduces the heat loss through the sidewalls to the junction of the thermoelectric legs, resulting in an improved thermoelectric efficiency. The pair was connected to a series circuit to generate an open-circuit voltage ( $V_{oc}$ ) of 107.98 mV. The maximum output power ( $P_{max}$ ) of the thermoelectric cell was 7.1  $\mu\text{W}$  at  $\Delta T = 473$  K. A significant increase in the output characteristics of the cell indicates that the bulk was effective. The horizontal-shaped cell of the bulk thermoelectric oxide exhibited promising output characteristics.

## 1. Introduction

Thermoelectric device systems are solid-state energy devices that can convert heat energy directly into electrical energy without moving parts or the production of environmentally harmful waste, regardless of the size of the source, yielding cleaner forms of energy [1].

In the mid 1990s, new guiding principles garnered increasing attention for novel materials, including oxides. Oxide materials have excellent thermoelectric properties, such as being non-toxic to researchers, cheap, and chemically stable at high temperatures. The experimental results previously revealed significant potential for applications in high-temperature oxide thermoelectric power generators; however, the performance of the oxide modules is still relatively low, particularly in comparison to metal-semiconductor materials [2–4]. Among thermoelectric oxide materials, *p*-type layered cobaltite  $\text{Ca}_3\text{Co}_4\text{O}_9$  (CCO) and *n*-type perovskite  $\text{CaMnO}_3$  (CMO) are promising barrier candidates for thermoelectric applications because of their chemical stability at high temperatures. For *p*-CCO with *ZT* values reaching up to 0.40 at 975 K [5], the *n*-CMO materials still need to be further studied because they do not have *ZT* values as good as *p*-type materials. Research on CMOs presented in this study obtained *ZT* values in the range of 0.018–0.075 [6].

The fabrication and power generation of oxide thermoelectric

modules have a low conversion efficiency; however, they are composed of non-toxic, easily accessible elements with excellent chemical stability in air, even at high temperatures in the range of 800–1000 K. For instance, *p*- $\text{Ca}_3\text{Co}_4\text{O}_9$ , *n*- $\text{Ca}_{0.97}\text{Bi}_{0.03}\text{MnO}_3$  was reported by Paengson et al. [7]. It was observed that the  $\pi$ -shape exhibited the highest maximum voltage of 76.8 mV, approximately 70 mA electrical current, and electrical power of 4 mW at a temperature difference of 200 K. The 12 pairs of *p*-CCO/*n*-CMO legs with dimensions of 0.5 mm  $\times$  5 mm  $\times$  3 mm were fabricated using the Cu electrodes with low differential temperature ( $\Delta T = 200$  K,  $T_c = 473$  K) with  $R_{load}$  in the range of 0.1–0.75 k $\Omega$ . Seetawan et al. reported that the output voltage generated ( $V_{out}$ ) was 0.8 V, output current ( $I_{out}$ ) was 2.46 mA, maximum output power ( $P_{out}$ ) was 1.98 mW, and maximum conversion efficiency ( $\eta$ ) was 0.15% [8]. According to Phaga et al. [9], the thermoelectric module was composed of *n*-CMO and *p*-CCO 31 couples/in<sup>2</sup> and the electrodes were made of thin copper sheet and silver paste. The mean voltage was determined as 121.70 mV, electric current 0.012 mA, and output power 1.47 W.

As mentioned previously, the traditional thermoelectric module was constructed from a *p*–*n* type of thermoelement assembly of more than ten couples with the  $\pi$ -shape. A traditional thermoelectric module is connected electrically in series and thermally in parallel on a ceramic substrate. The spaces between the *p*–*n* thermoelements increase the heat loss and thus reduce the electrical generation performance.

\* Corresponding author. Program of Physics, Faculty of Science and Technology, Sakon Nakhon Rajabhat University, Sakon Nakhon, 47000, Thailand.  
 E-mail address: [t\\_seetawan@snru.ac.th](mailto:t_seetawan@snru.ac.th) (T. Seetawan).

<https://doi.org/10.1016/j.physb.2022.413865>

Received 11 January 2022; Received in revised form 18 March 2022; Accepted 21 March 2022

Available online 23 March 2022

0921-4526/© 2022 Elsevier B.V. All rights reserved.

However, no pair of thermoelectric oxide materials can maintain high thermoelectric performance over the entire service temperature range. Therefore, the proposed oxide thermoelectric modules for heat energy recovery are designed with different internal geometries, shapes of thermoelements, or emplacements such as segmentation and design, resulting in a more stable flow. Segmentation has been suggested as an approach for thermoelectric modules. Each *p*- and *n*-leg in a segmented leg is composed of at least two different *p*- and *n*-materials, respectively [10]. These interfaces between the joints can cause significant heat and electrical losses, resulting in reduced module efficiency. In comparison to a traditional module of cobaltite  $\text{Ca}_3\text{Co}_4\text{O}_{9.6}$  *p*-leg, the power density of a segmented module with a bulk half-Heusler, cobaltite  $\text{Ca}_3\text{Co}_4\text{O}_{9.6}$  *p*-leg, and ZnO *n*-leg increased more than threefold [11]. Wannasut et al. synthesized  $\text{YBa}_2\text{Cu}_3\text{O}_{7-x}/\text{Ca}_3\text{Co}_4\text{O}_9$  bulk ceramic with a high relative density of approximately 96% via hot pressing at high temperatures. They were successful even though there may be a reaction and/or ionic diffusion at the interface. Therefore, hot pressing seems to be a suitable method for producing high-quality bulk oxide thermoelectric ceramics [12].

To overcome the limitations of traditional thermoelectric modules, new strategies and concepts for module design and fabrication are required. Combining two types of thermoelements without the gap/space between segments is expected to achieve higher efficiency because it reduces heat loss in the systems. A newly designed TEG was fabricated using a single *p*-*n*-type thermoelectric material in the horizontal direction [11]. Zhang presented a new design concept for a thermoelectric generator that eliminates heat loss and improves module performance by reducing the space between the thermoelements. In comparison to the traditional module design, the power generation of the proposed module design increased by 8%, and its efficiency increased by 20%, according to the modeling results [13].

Kanas et al. demonstrated a new concept for a thermoelectric module based on a hybrid *p*-*n* junction of *p*-CCO and *n*-CMO. The modification of the thermoelectric module design resulted in an increase in the output power from 12.4 (3.1) to 28.9 mW/cm<sup>2</sup> (7.2 mW) at  $\Delta T = 923$  K after two days of maintaining the temperature for the hot side at 1173 K [14].

Thus far, no detailed reports have been published on horizontal bulk oxide thermoelectric cells. We proposed a new innovative high-temperature thermoelectric cell comprising layered cobaltite  $\text{Ca}_3\text{Co}_4\text{O}_9$  and perovskite  $\text{CaMnO}_3$ . The gaps between the two types of oxide thermoelectric materials were removed by combining thermoelement couples. In terms of the *I*-*V* testing circuit, measurements are not less than three times because the magnitudes of the voltage (V) and the matching resistance load with current (A) can be measured by standard digital multimeters. The generated voltage and current were scanned at different points, less than 100 ms apart, to obtain the *I*-*V* curves or to operate the TEG under a dynamic load. The bulk thermoelectric cell improved the maximum output power at  $\Delta T = 473$  K.

## 2. Experimental procedures

### 2.1. Materials preparation and characterization

*p*-CCO was synthesized through a solid-state reaction method and pressed into pellets through hot-press (HP) sintering. Commercial nanopowder precursors of  $\text{CaCO}_3$  and  $\text{Co}_2\text{O}_3$  were mixed in stoichiometric amounts and calcined at 1023 K for 10 h in air. The calcined powder was pelletized for densification via HP sintering by heating to 1023 K using uniaxial pressure of 20 MPa for 1 h under argon atmosphere (heating/cooling rate of 5 °C/min).

*n*-CMO materials were prepared using commercial nanopowder precursors of  $\text{CaCO}_3$  and  $\text{MnO}_2$  as starting powders in appropriate ratios and mixed through planetary ball milling; thereafter, ethanol was added for 8 h. The mixtures were dried and heated at 1123 K for 10 h in oxygen atmosphere. The *n*-CMO powder was pelletized for densification through hot pressing under a mechanical pressure of 10 MPa, whereas

conventional sintering was performed at 1173 K for 24 h (heating/cooling rate of 5 °C/min).

Measurements of electrical resistivity ( $\rho$ ) and Seebeck coefficient ( $\alpha$ ) were performed on a ULVAC-RIKO ZEM-3 from room temperature to 873 K on a 0.1 bar of helium. The thermal conductivity ( $\kappa$ ) was determined from the measured thermal diffusivity ( $\alpha$ ), heat capacity ( $C_p$ ), and density ( $d$ ) using the following formula:  $\kappa = d(T) \times \alpha(T) \times C_p(T)$ . The mass densities of the samples were measured through the Archimedes' method using a density kit (MS-DNY-54, METTER TOLEDO). Thermal diffusivity was measured using an LFA-457 laser flash system. The thermal conductivity of the samples was determined using experimentally measured thermal diffusivity, specific heat, and density. The microstructures of the contacts and joining parts were observed through field-emission scanning electron microscopy (FESEM, JSM-7610F, JEOL, Japan).

### 2.2. *p*-*n* horizontal bulk thermoelectric cell design and fabrication

A horizontal thermoelectric cell was designed using a solid work program and assembled using the soldering method. The design of the thermoelectric cell was determined by assigning a material with 3.5 mm × 3.5 mm × 5 mm dimensions and an Ag electrode with 3.5 mm × 3.5 mm × 0.1 mm dimensions as shown in Fig. 1. Modeling was used to design the measurement system and determine the appropriate output performance. As shown in Fig. 1, for the fabrication of the horizontal legs, the obtained thermoelement pellets were cut into rectangular pieces with desired dimensions of 3.5 mm × 3.5 mm × 5 mm. First, pieces of thermoelements were polished and cleaned through ultrasonication for 3 min in acetone to remove contaminants. An Ag sheet with purity of 99.99% and thickness of 0.1 mm was used to make the electrodes and join the thermoelements. The brazing joining method was performed with a 1 mm thick Ag paste. After joining the oxide legs and Ag sheets, the joint was dried at 423 K for 10–15 min and thereafter fired at 1023 K for 10 min to establish excellent electrical contact between the metal electrodes and thermoelectric oxides. Excellent contact between thermoelectric materials when fabricating a horizontal shape is important. There should be no interdiffusion between adjacent materials because it could result in a negative change in the thermoelectric properties of the materials. Therefore, the contact resistance at the junction should be as low as possible to avoid affecting the electrical and thermal currents in thermoelectric devices [10].

### 2.3. Measurement the efficiency of thermoelectric cell phones

The efficiency of the thermoelectric cell, including the output electrical voltage, electrical current, and thermal power, were measured after fabrication. These parameters were measured using a laboratory

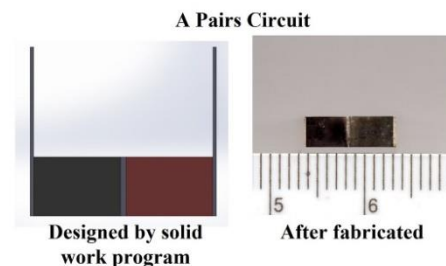


Fig. 1. Model design of *p*-*n* bulk thermoelectric cell configuration and after fabricated of the horizontal design.

test system. Fig. 2 illustrates a schematic of the measurement system concept. A temperature controller was used to create a temperature gradient (hot side from the heater and cold side from the water tank), and an electrical controller was used to measure the efficiency of the in-test cell. A ceramic heating core cover with copper sheets was heated by a power source provided that the heat touched it nearly at each junction. The ends of the heaters had a temperature range of 573–623 K, as measured by the thermocouples. The cold-side temperature was maintained by running water from a vending water machine with a controllable temperature of less than 283 K on an aluminum tank before starting the testers. A thermoelectric cell was placed between the aluminum tank and the junction areas with heaters to maintain excellent thermal contact between the junctions. The thermoelectric cell was connected in series with an external load ( $R_{load}$ ) and an internal load ( $R_{int}$ ) that controlled the current in the entire circuit, generating an electrical voltage under a temperature gradient. For the designed measurement, the electronic load was used for matching if it reached a value close to the current, along with the voltage of the thermoelectric cell. To detect the temperature gradient, we used a thermocouple wire with a 0.4 mm diameter, which had contact with the hot side, cold side, and interface areas.

The geometries of the power generators are conceptually identical. In this case, the left and right sides were adjoined with a cooling source and the joint was connected to a heat source.

An electric circuit was constructed by joining horizontal thermoelectric cells of  $p$ -CCO and  $n$ -CMO materials. The joint was composed of Ag layers to create an excellent electrical conductor. The current is produced by voltage and it passes from one thermoelement to another via the connecting joint. When current flows within the module, heat radiates from the joint to cooled areas. The horizontal thermoelectric device configuration has lower heat losses from the electrical connections (joints) between the different types of thermoelements in comparison to the traditional design. The maximum benefit when creating the horizontal design is the reduction in electrical resistance and heat loss in the thermoelements and interfaces.

### 3. Results and discussion

Fig. 3(a) shows an image of the  $p$ -CCO/Ag/ $n$ -CMO bulk ceramic were combined to form. It is observed that the  $p$ -CCO (top) and  $n$ -CMO (bottom) layers connect with the Ag layer in the middle of the thermoelectric cell. A horizontal-shaped thermoelectric cell was fabricated in addition to the electrode contacts by the Ag brazing and soldering methods. This suggests that the fabrication process in this study has no effect on the phase or thermoelectric properties of each thermoelement. However, Fig. 3(b) shows a gap in the joint of the Ag electrode layer between the two thermoelements that is caused by incomplete brazing and soldering methods, resulting in a small gap between the layers. The average thickness of the Ag electrode was 279  $\mu\text{m}$ , which had a favorable effect on the interfacial contact resistance. Owing to the occurrence of gaps, the interfacial contact (electrical and thermal) resistance was slightly high, which affected the generated electrical power of the horizontal thermoelectric cell. From the measured results, the exhibit resistance was 0.33 k $\Omega$ . In addition, when we fabricated the connection to the joint without gaps between the two elements, the thin layers of the Ag electrode could send heat directly to the thermoelectric cell without heat loss. Moreover, we confirmed that a single phase on each side indicated a clear separation between the  $p$ -CCO and  $n$ -CMO layers. Phase formation at the interface of the  $p$ -CCO, Ag layer, and  $n$ -CMO was further investigated through FESEM. The FESEM results demonstrated that the interface area between the  $p$ -CCO and  $n$ -CMO layers separated by the Ag layer could be clearly observed. The Ag layer blocked the diffusion reaction between the two types of thermoelements. Chemical characterization of the  $p$ -CCO/Ag layers/ $n$ -CMO and the area of the interface boundary were studied through energy dispersive X-ray (EDX) spectrometry. The quantitative data for the composition on each side are shown in Fig. 3(c). In the  $p$ -CCO area (blue bar), the layer is mainly composed of calcium (Ca), cobalt (Co), carbon (C), and oxygen (O). The bottom area is prominently composed of calcium (Ca), manganese (Mn), and oxygen (O) in the  $n$ -CMO layer (red bar). Notably, all the elements were detected at the  $p$ -CCO/Ag/ $n$ -CMO interface (yellow bar). These observations may explain the lower measured interfacial contact resistance than that reported in Ref. [15] for the  $\text{Fe}_{22}\text{Cr}$  electrode.

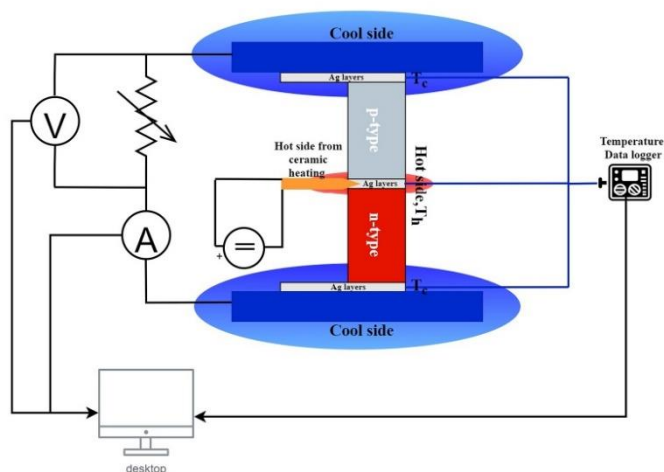


Fig. 2. Schematic diagram of the measurement systems concept.



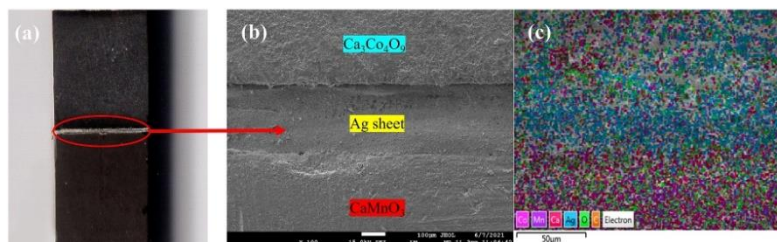


Fig. 3. (a) Image of the fabricated horizontal shape thermoelectric cell, (b) interfacial area between p-CCO, Ag layer, and n-CMO layers, and (c) EDX elemental map of interfacial area.

#### TE performance of the single materials

Before fabrication, the horizontal shape of the thermoelectric cell of each thermoelement was measured to determine the temperature dependence of its thermoelectric properties, as shown in Fig. 4. The  $\alpha$  value of the n-CMO sample was  $-269.219 \mu\text{V/K}$  at 763 K. Our previous study on the  $\alpha$  value of the p-CCO sample revealed that it increased with an increasing temperature of  $185 \mu\text{V/K}$  at approximately 973 K [16]. p-CCO and n-CMO samples were synthesized from nanometer-sized  $\text{CaCO}_3$ ,  $\text{Co}_2\text{O}_3$ , and  $\text{MnO}_2$  precursors. A significant effect can be observed in the reduced thermal conductivity of the samples synthesized with nanometer-sized precursors.

The electric power of a thermoelectric cell is unexpected under realistic working conditions because several factors affect the output power of the cell, for instance, heat losses in joint areas, temperature, contact resistances, and cold areas should have the same temperature and heat transfer. Thereafter, the performance of a thermoelectric cell can be described as follows from the open-circuit voltage [17–19]:

$$V_{OC} = 2\alpha\Delta T \quad (1)$$

Ohm's law was used to demonstrate the electrical properties. The output current ( $I$ ) is proportional to the open-circuit voltage with the sum of the internal resistances of the device ( $R_{int}$ ) and the external resistive load ( $R_{load}$ ), electrical resistance ratio,  $m = R_L/R_i$  by [18].

$$I = \frac{V_{OC}}{R_{int} + R_{load}} = \frac{\alpha\Delta T}{\rho l(1 + m)} \quad (2)$$

The small thermocouples wires used to detect the temperature were placed on the surface of Ag electrodes as a result their insignificant

thermal contact resistance. Therefore, the  $V_{OC}$  values measured are well reflecting the actual temperature span across the TE legs [17,20].

The power output of the thermoelectric cell is expressed as follows [18]:

$$P = I^2 R_{load} = V_{OC}^2 \left[ \frac{R_{load}}{(R_{int} + R_{load})^2} \right] \quad (3)$$

$$P_{max} = \frac{V_{OC}^2}{4R_{load}} \quad (4)$$

Because the resistivity of each thermoelement is temperature-dependent, it varies dramatically with temperature. The power output reaches a maximum value when the external load resistance is identical to the internal resistance.

Fig. 5 shows the power generation characteristics of the thermoelectric cell under various applied temperature gradients. As expected, the voltage-current  $V(I)$  and output power current  $P(I)$  exhibit a similar tendency of increasing as the temperature increases. At the highest applied temperature variance ( $T_h/T_c = 497 \text{ K}/\sim 297 \text{ K}$ ),  $\Delta T \approx 473 \text{ K}$ , the measured  $V_{OC}$  of the thermoelectric device is 82.14 mV, and the voltage decreased linearly with increasing current. The measured maximum output power reached a value of  $7.30 \mu\text{W}$  at a current of 0.0026 mA and a voltage of 107.98 mV. However, several TE modules exhibited low performance and, in all cases, performance that is significantly lower than that predicated in theory. This is believed to be mainly due to the contact resistance at the junctions (metal/metal, metal/oxide, and oxide/oxide), thus limiting the magnitude of the output power. From literature reviews, the thermoelectric module was composed of small n-CMO and p-CCO of 31 couples/in<sup>2</sup> and the use of a

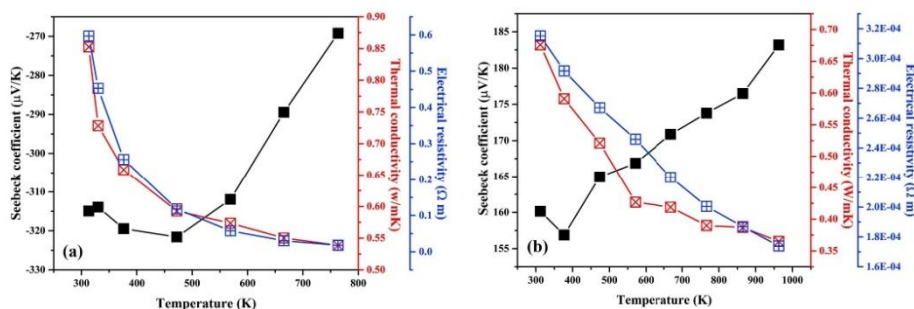


Fig. 4. Temperature dependence of the thermoelectric properties of (a) p-CCO and (b) n-CMO.



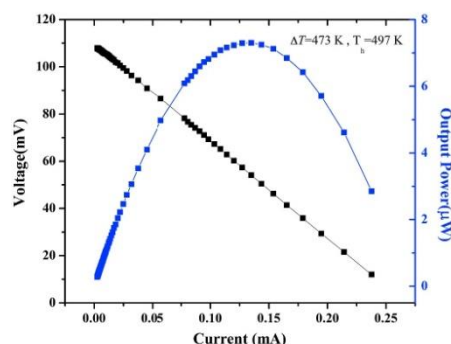


Fig. 5.  $V$ - $I$  and  $P$ - $I$  curves of horizontal shape of bulk thermoelectric cell as a function of temperature variance at  $T_h = 497$  K.

thin copper plate and Ag paste as electrodes, as reported by Phaga et al. [9]. It was observed that the mean voltage was  $\sim 121.70$  mV, current was  $\sim 0.012$  mA, and power was  $\sim 1.47$   $\mu$ W. From the above, when compared the results from this work with literature reviews, the reason for this high electrical power caused by the modification of contact electrode (Ag brazing soldering process), the optimized material properties (hot-pressed process and nanoparticle effect), and we can reduce heat losses because of good packing of thermal insulation with the design of the horizontal shape.

#### 4. Conclusions

We demonstrated an efficient way to improve the electrical power of oxide-based thermoelectric cells to design horizontal legs. The selection of materials in the horizontal direction was based on their thermoelectric properties and ZT. Using this approach, we successfully demonstrated the horizontal shape of a bulk thermoelectric device using p- $\text{Ca}_3\text{Co}_4\text{O}_9$  and n- $\text{CaMnO}_3$  legs with improved output power. The improved efficiency of the oxide horizontal thermoelectric cell also benefits from the reduced resistance of the cell because of the low contact resistance of the oxide materials and Ag electrodes. The horizontal shape of bulk thermoelectric oxide with series circuit exhibited total internal resistance of approximately 0.33 k $\Omega$  and  $V_{OC}$  of 107.98 mV.  $P_{max}$  of all thermoelectric modules increased with increasing temperature variance  $\Delta T$  between the hot- and cold-side temperatures of the modules. At the temperature gradient  $\Delta T \approx 473$  K, the maximum output power of a single thermoelectric device was 7.30  $\mu$ W. A significant increase in the output characteristics of the module indicates that the horizontal shape was effective. The horizontal-shaped bulk oxide thermoelectric cell exhibited promising output characteristics.

#### Funding

This work was financially supported by The Royal Golden Jubilee Ph. D. Programme (RGJ-PhD) (Grant No. PHD/0065/2560), and the Thailand Research Fund (TRF) Research Career Development Grant (RSA6180070).

#### Credit author statement

Tosawat Seetawan: Conceptualization, Supervision, Validation,

Wanatchaporn Namhonsa Methodology, Data curation, Writing – original draft preparation. Visualization, Investigation. Writing-Reviewing and Editing.

#### Declaration of competing interest

The authors declare that they have no known competing financial interests or personal relationships that could have appeared to influence the work reported in this paper.

#### Acknowledgments

The authors would like to express the gratitude to the research facility support from Center of Excellence on Alternative Energy, Sakon Nakhon Rajabhat University and the thermal diffusivity measurements were supported by Dr. Sora-at Tanusilp and Prof. Ken Kurosaki at Kyoto University, Japan. Finally, we are grateful to Dr. Ryoji Funahashi at the National Institute of Advanced Industrial Science and Technology for the useful discussions.

#### References

- [1] L.E. Bell, Cooling, heating, generating power, and recovering waste heat with thermoelectric systems, *Science* 321 (2008) 1457–1461.
- [2] M. Ohtaki, Recent aspects of oxide thermoelectric materials for power generation from mid-to-high temperature heat source, *J. Ceram. Soc. Jpn.* 119 (2011) 770–775.
- [3] N. Pryds, B. Rasmus, Oxide thermoelectrics: from materials to module, *Adv. Ceram. Energy Conv. Syst.* (2020) 131–156.
- [4] R. Funahashi (Ed.), *Thermoelectric Energy Conversion: Theories and Mechanisms, Materials, Devices, and Applications*, Woodhead Publishing, 2021.
- [5] T. Yin, D. Liu, Y. Ou, F. Ma, S. Xie, J.F. Li, J. Li, Nanocrystalline thermoelectric  $\text{Ca}_3\text{Co}_4\text{O}_9$  ceramics by sol–gel based electrosintering and spark plasma sintering, *J. Phys. Chem. C* 114 (2010) 10061–10065.
- [6] S.D.O. Torres, D. Thomazini, G. P. Balhazar, M.V. Gelfuso, Microstructural influence on thermoelectric properties of  $\text{CaMnO}_3$  ceramics, *Mater. Res.* 23 (2020).
- [7] S. Paengpon, Uni-leg and  $\pi$ -shape thermoelectric cells, *SNRU. J. Sci. Technol.* 8 (2016) 199–203.
- [8] T. Seetawan, K. Singsoog, S. Srichai, C. Thanachayanont, V. Amornkitbamrung, P. Chindaprasit, Thermoelectric energy conversion of p- $\text{Ca}_3\text{Co}_4\text{O}_9$ /n- $\text{CaMnO}_3$  module, *Energy Proc.* 61 (2014) 1067–1070.
- [9] P. Phaga, A. Vora-Ud, T. Seetawan, Invention of low-cost thermoelectric generators, *Procedia Eng.* 32 (2012) 1050–1053.
- [10] H.N. Pham, Design and Optimization of Effective Segmented Thermoelectric Generator for Waste Heat Recovery, Department of Energy Conversion and Storage, Technical University of Denmark, 2015.
- [11] L.T. Hung, N. Van Nong, L. Han, R. Bjerk, P.H. Ngan, T.C. Holgate, N. Pryds, Segmented thermoelectric oxide-based module for high-temperature waste heat harvesting, *Energy Technol.* 3 (2015) 1143–1151.
- [12] P. Wannan, N. Keavprak, P. Jaibon, A. Watcharaporn, Preparation and physical properties of segmented thermoelectric  $\text{YBa}_2\text{Cu}_3\text{O}_{7-x}$ - $\text{Ca}_3\text{Co}_4\text{O}_9$  ceramics, in: *IOP Conference Series: Materials Science and Engineering*, vol. 33, 2018, 012010.
- [13] T. Zhang, A new design concept for a thermoelectric generator with multiscale, multiphase, multifunctional composites, *Clean Energy* 2 (2018) 154–166.
- [14] N. Kanas, R. Bjerk, K.H. Wells, R. Schuler, M.A. Einarsrud, N. Pryds, K. Wilk, Time-enhanced performance of oxide thermoelectric modules based on a hybrid p-n junction, *ACS Omega* 6 (2020) 197–205.
- [15] T.C. Holgate, L. Han, N. Wu, E.D. Bojesen, M. Christensen, B.B. Iversen, N. Pryds, Characterization of the interface between an Fe–Cr alloy and the p-type thermoelectric oxide  $\text{Ca}_3\text{Co}_4\text{O}_9$ , *J. Alloys Compd.* 582 (2014) 827–833.
- [16] W. Namhonsa, T. Seetawan, Enhanced ZT of  $\text{Ca}_3\text{Co}_4\text{O}_9$  by nano-sized precursor, *Jpn. J. Appl. Phys.* (2021).
- [17] Y. Apertet, H. Ouerdane, C. Goupil, P. Lecoeur, Equivalent parameters for series thermoelectrics, *Energy Convers. Manag.* 93 (2015) 160–165.
- [18] D. M. Rowe, *CRC Handbook of Thermoelectrics*, CRC press, 2018.
- [19] H.S. Han, Y.H. Kim, S.Y. Kim, S. Um, J.M. Hyun, Performance measurement and analysis of a thermoelectric power generator, in: 2010 12th IEEE Intersociety Conference on Thermal and Thermomechanical Phenomena in Electronic Systems, IEEE, 2010, pp. 1–7.
- [20] Y. Apertet, H. Ouerdane, C. Goupil, P. Lecoeur, Influence of thermal environment on optimal working conditions of thermoelectric generators, *J. Appl. Phys.* 116 (2014) 144901.



## APPENDICE B

### INTERNATIONAL CONFERENCES



1. **Namhongsa, W.,** & Seetawan, T. (2022). “Enhancing Power Factor of CCO–349 by Reduced Crystallite Size and Rapid Sintering Method” The 38<sup>th</sup> International Conference on Thermoelectrics and the 4th Asian Conference on Thermoelectrics at Gyeongju Hwabaek International Conventions Center, Gyeongju, South Korea, 30 June to 4 July 2019
2. **Namhongsa, W.,** & Seetawan, T. “Effect of The PVA on the Characterization and Thermoelectric Properties of  $\text{CaMnO}_3$ ” The 5<sup>th</sup> International Conference on Smart Materials and Nanotechnology (SmartMat@2020X December 1 – 4, 2020, Pattaya, Thailand



## APPENDICE C

### THE ACTIVITIES





1. Joining the 34<sup>th</sup> Computational Materials Design (CMD) workshop at Osaka University, Osaka, Japan 18 – 22 February 2019



2. Assistant Lecturer “Thermoelectric Materials Simulation and Device Fabrication Workshop2019” at University of Yangon, Myanmar, 7–8 March 2019



3. Assistant Lecturer Asean Alternative Energy Workshop AAEW2019, Sakon Nakhon Rajabhat University, 14 June 2019





## APPENDICE D

### A BRIEF HISTORY OF RESEARCHER



## A BRIEF HISTORY OF RESEARCHER

### PERSONAL DATA:

Name	Wanatchaporn Namhongsa
Academic Position	Ph.D. student
Date of Birth	March 25, 1993
Place of Birth	Amnat Charoen, Thailand
Nationality	Thai
Marital Status	Single
Address	
1. Home:	234 Phanason Villa 10, King Rama 9 Road, King Rama 9 Soi 48 Dok Mai, Prawet, Bangkok 10250, Thailand Tel. +669-0339-4650
2. Office:	Center of Excellence on Alternative Energy, 680/31 Nittayo Road, Sakon Nakhon Rajabhat University, Sakon Nakhon 47000, Thailand Tel. +66-42-744319 Fax. +66-42-744319 namhongsa@snru.ac.th

### EDUCATION:

Primary School: Suppakornwittaya School, Bangkok, 2001–2006

Secondary School: 1–6, Sirirattanathorn School, Bangkok, 2006–2011

## College:

B.S. Major: Physics

Sakon Nakhon Rajabhat University, Thailand, 2011–2014

Research Title: EFFECTS OF MAGNETIC FIELD ON SYNTHESIS AND  
THERMOELECTRIC PROPERTIES OF  $\text{NaCoO}_2$

## Graduate Schools:

M.S. Physics

Sakon Nakhon Rajabhat University, Thailand, 2015–2018

Thesis Title: GENERATE ELECTRICITY OF THERMOELECTRIC FROM  
HEAT IN RICE MILL INDUSTRY

Ph.D Physics

Sakon Nakhon Rajabhat University, Thailand, 2018–present

Thesis Title: Thermoelectric Multilayer Generator of Nano Oxide  
Thermoelectric Materials

**SCHOLARSHIPS:**

- 2012–2013     National Metal and Materials Technology, Cooperation Research  
Scholarship
- 2013–2014     Sakon Rajabhat Nakhon University Scholarship for Thesis
- 2015–2018     Research and Researchers for Industries (RRI) Scholarship for Master degree
- 2018–present   Ph.D student of The Royal Golden Jubilee Ph.D. Programme

**NATIONAL AND INTERNATIONAL PUBLICATIONS:**

1. W.Namhongsa , T.Seetawan, U.Seetawan , A.Ratchasin , S.Srichai ,  
K.Singsoog, C.Ruttanapun, S.Siridejachai “Analysis of Thermoelectric Generator  
by Finite Element Method” Physics Procedia 32 (2012) 1006 –1011  
International Science, Social–Science, Engineering and Energy Conference  
2012: Engineering Science and Management.
2. Wanatchaporn Namhongsa, Urai Seetawan, Tosawat Seetawan\* “Synthesis  
CaMnO<sub>3</sub> Thermoelectric Materials Substituted Ca and Mn by Na” The 5<sup>th</sup>  
SNRU International Conference on Cooperation for Development on the East–  
West Economic Corridor : Cooperation Networks for Sustainable Development  
towards ASEAN 20 July 2012, Sakon Nakhon Rajabhat University , Sakon  
Nakhon, Thailand
3. Wanatchaporn Namhongsa, Urai Seetawan, Tosawat Seetawan\*  
“Thermoelectric Properties of Ca<sub>0.8</sub>Na<sub>0.2</sub>MnO<sub>3</sub>” The 2<sup>nd</sup> Southeast Asia  
Conference on Thermoelectrics 30 October 2012, Sakon Nakhon Rajabhat  
University, Sakon Nakhon, Thailand
4. Wanatchaporn Namhongsa, Tosawat Seetawan, Pennapa Muthitamongkol  
and Chanchana Thanachayanont “Microstructure and Thermoelectric

Properties of  $\text{Na}_{0.5}\text{CoO}_2$ ” International Conference on Engineering, Applied Science, and Technology (ICEAST 2013). Advanced Materials Research Vol. 802 (2013) pp 218–222 (SJR 0.13)

5. W. Namhongsa, K. Singsoog, S. Paengson, P. Pilasuta, T. Seetawan, P. Muthitamongkol and C. Thanachayanont “Effect of magnetic field on synthesis of  $\text{NaCoO}_2$ ”. 3<sup>rd</sup> Southeast Asia Conference on Thermoelectrics 2014. 22–24 December 2014, Champasak Grand Hotel, Pakse, Laos PDR. Journal Integrated Ferroelectrics Vol 165:1 (2015) pp 81–85 (SJR 0.375)

6. Wanatchaporn Namhongsa, Kunchit Singsoog, Supasit Paengson, Panida Pilasuta, Meena Rittirum, Arthorn Vora-ud, and Tosawat Seetawan “Thermal conductivity of GeTe simulated by molecular dynamics” Sakon Nakhon Rajabhat University International Conference 24 July, 2015, Sakon Nakhon, Thailand

7. Wanatchaporn Namhongsa, Tatsuro Omoto, Yosuke Fujii, Tosawat Seetawan, and Atsuko Kosuga. “Effect of the crystal structure on the electronic structure and electrical properties of thermoelectric  $\text{GeSb}_6\text{Te}_{10}$  prepared by hot pressing” Scripta Materialia Vol. 133 (2017) pp. 96–100 (IP=3.375)